Electron-Muon Correlations in Proton+Proton and Deuteron+Gold Collisions at PHENIX

Tatia Engelmore

Submitted in partial fulfillment of the
requirements for the degree of
Doctor of Philosophy
in the Graduate School of Arts and Sciences

Columbia University

2011

Abstract

Electron-Muon Correlations in Proton+Proton and Deuteron+Gold Collisions at PHENIX

Tatia Engelmore

This dissertation presents the first measurement of electron-muon azimuthal correlations at the PHENIX experiment at RHIC in 200 GeV proton-proton and deuteron-gold collisions. Electron-muon pairs result from the semileptonic decay of D mesons, which come from correlated charm pairs. The pairs are measured at forward rapidity, with $|\eta| < 0.5$ for the electron and $1.4 < |\eta| < 2.1$ for the muon. Electron-muon pairs exhibit a characteristic peak at $\Delta\phi = \pi$ in the azimuthal distribution due to momentum conservation in the $c\bar{c}$ decay, and this enables clear identification. The shape of the azimuthal pair distribution in p+p collisions helps us determine which hard scattering processes contribute to charm production, and it allows us to test NLO QCD predictions. The p+p result also serves as a baseline measurement for understanding heavy ion collisions. Pairs were also measured in d+Au collisions at forward rapidity in the deuteron-going direction, which is a kinematic region at which we expect suppression effects to be evident. The pair yield in d+Au was found to be suppressed relative to that in p+p. Also the

peak in $\Delta\phi$ almost disappears in d+Au, indicating either a change in charm production mechanisms or interactions with the nuclear matter.

Contents

List of Figures

List of Tables

Acknowledgments

Getting a Ph.D is a long and difficult, though rewarding, process. It wouldn't have been possible without my parents and my friends because of the support (and commiseration) they provided through the whole journey. I'd like to thank my advisor, Brian Cole, for suggesting the measurement, and giving me guidance along the way. I also want to thank Nathan Grau, who spent a lot of time working through the details of this analysis with me. All of my knowledge of programming can be credited to Dave Winter, who was of great help, especially when I first joined the group. Also to all of the other members of the Columbia group, who made it enjoyable to come into work each day. Finally I want to thank my husband, Simon West, for encouraging me to stick with it during the most difficult parts of my Ph.D. It was certainly worth it in the end!

Chapter 1

Introduction

The early 21st century is a unique time in the history of physics. Much of what we know about the world has been distilled into well-tested physical laws, leaving mysteries regarding only the most extreme physical conditions. Of the four fundamental forces, we understand how to use electromagnetism and the weak force to predict observable phenomena. Gravity is described by general relativity to good agreement with experiment, though the theory likely needs to be refined or expanded upon in order to unify it with the other four forces. The final force is the strong force (described by quantum chromodynamics), for which we know the fundamental Lagrangian, though it has proven to be a difficult theory to make predictions from due to its complexity. In our quest to understand gravity we are searching for gravity waves caused by exotic astronomical objects; in order to explore the limits of quantum chromoynamics (QCD) we have built high energy heavy ion colliders such as the Relativistic Heavy Ion Collider (RHIC). Heavy ion collisions allow us to test

experimentally the extremely complicated theory of QCD and thereby help complete a coherent physical picture of the world.

1.1 Content and Structure of this Thesis

The topic of this thesis is the measurement of electron-muon correlations in proton-proton and deuteron-gold collisions at $\sqrt{s} = 200$ GeV. These lepton pairs are the result of the semi-leptonic decay of D meson pairs. Because the D mesons are formed from $c\bar{c}$ pairs (or from the decay of two B mesons from a $b\bar{b}$ pair), this signal is a probe of heavy quark production, where "heavy" means charm and bottom. This measurement was made at the PHENIX experiment at the Relativistic Heavy Ion Collider (RHIC), located at Brookhaven National Laboratory in Upton, New York (see Sec. 3.1.1). The purpose of the measurement in p+p collisions is to provide a better understanding of heavy quark production at intermediate rapidity ranges in order to test perturbative QCD (pQCD) predictions. Angular correlations give insight into production mechanisms that previous heavy flavor measurements (namely single electrons and muons) were not able to do. Similar measurements in d+Au, using p+p as a baseline, help provide an understanding of how heavy quark production is modified due to effects from being created in nuclear matter. This measurement will help us to understand the distribution of partons in the nucleus, as well as the role of initial and final state interactions in particle production.

The structure of the remainder of this thesis is as follows: first, the introduction outlines the basic concepts involved in a heavy ion analysis, with an emphasis on the physics of d+Au collisions. This includes asymptotic freedom, nuclear structure functions, and saturation effects. The next chapter describes charm production in nuclear collisions, and how it may be modified by cold nuclear matter effects. Then comes a detailed description of the PHENIX detector, focusing on the individual detectors used in this analysis. After that is are two chapters on the details of the measurement of electron-muon correlations in p+p and d+Au collisions. Finally, a discussion of the results obtained from comparing these datasets.

1.2 RHIC Physics

RHIC was designed to probe a new state of matter, the quark-gluon plasma (QGP). The QGP is a deconfined state of quarks and gluons that only exists at extremely high temperature and density. This phase of matter is only found in extreme conditions, for example in the high baryon density state of the core of a hypothetical quark star, or the high energy density in the early universe. The universe existed in the QGP state at approximately 10 microseconds after the Big Bang [1], after which it cooled to the point where hadrons could form. The goal of the RHIC experiments was to recreate the QGP via gold-gold collisions, and to study its properties in order to better understand the complicated and

non-perturbative interactions in quantum chromodynamics.

1.2.1 Quantum Chromodynamics

Quantum chromodynamics (QCD) is the fundamental theory of the strong interaction. It describes the interactions between fundamental fermions called quarks through the exchange of massless bosons called gluons. QCD is a non-abelian (Yang-Mills) theory that exhibits SU(3) symmetry. The quarks have three possible charges (colors), red, green, and blue, and these make up the fundamental representation of SU(3). The QCD Lagrangian is given by

$$\mathcal{L}_{QCD} = -\frac{1}{4}F^{\alpha}_{\mu\nu}F^{\alpha\mu\nu} + \sum_{q}\bar{q}_i(i\gamma^{\mu}D_{\mu} - m_q)_{ij}q_j \tag{1.1}$$

and the field strength tensor $F^{a}_{\mu\nu}$ is given by

$$F^{\alpha}_{\mu\nu} = \partial_{\mu}A^{\alpha}_{\nu} - \partial_{\nu}A^{\alpha}_{\mu} - g_s f^{abc}A^{b}_{\mu}A^{c}_{nu} \tag{1.2}$$

where the A_{μ} are the gluon fields, g_s is the gauge coupling, q are the fermion fields, and f^{abc} are the structure constants [2]. The covariant derivative D_{μ} is

$$(D_{\mu})_{ij} = \delta_{ij}\partial_{\mu} + ig_s T^{a}_{ij}A^{a}_{\mu} \tag{1.3}$$

where the T^{a}_{ij} are the Lie group generators. Because gluons carry a color charge themselves (unlike photons in QED) they can interact with each other, leading

to Feynman diagrams that contain both quark-gluon and gluon-gluon vertices.

One of the most important aspects of QCD is the fact that the coupling becomes stronger at large distances, or equivalently it becomes larger at a lower momentum scale. Conversely, at higher energies or short distances, quarks behave as if they are free particles. This behavior is known as asymptotic freedom. It arises in QCD because color-charged objects are anti-screened, meaning virtual gluons created in the vacuum around a color charge tend to augment its color. This is the opposite effect to that which occurs in QED, where virtual electron-positron pairs tend to screen electric charges so that you see less charge the further away you get. The strong coupling constant is given by [3]:

$$\alpha_s(Q^2) \equiv \frac{g_s(Q^2)}{4\pi} = \frac{1}{\beta_0 \ln\left(Q^2/\Lambda^2_{QCD}\right)} \tag{1.4}$$

Λ_{QCD} sets the momentum scale at which the strong force becomes non-perturbative, approximately less than 200 MeV. Processes occurring at energies above that are much simpler to calculate using perturbative methods: these are known as "hard" processes, and occur infrequently in heavy ion collisions. "Soft" processes are the non-perturbative processes that dominate collisions, and typically have a momentum scale of less than 2 GeV/c.

No free quark or gluon has ever been seen on its own: this is due to the principle of color confinement. Although hard to prove analytically, it means that quarks are only found in the form of hadrons. These include mesons, which contain a

quark and an antiquark, and baryons, which contain three quarks. In order to study quarks and gluons themselves we must probe hadrons and nuclei at high density. Before quarks and gluons were identified, the constituents of nuclei were known as "partons" based on a model developed by Bjorken [4]. This model was formulated in response to results from electron-nucleus collisions that showed the nucleus to be composed of point-like, loosely bound particles [5]. This is described in more detail below in Sec. 1.3.

Another convenient feature of QCD is the fact that cross sections can be factorized into perturbative and non-perturbative parts. This is known as the factorization theorem [6]. The pQCD cross section for the process $p + p \rightarrow h + X$ can be written as

$$E_h \frac{d\sigma^{pp\rightarrow h}_{hard}}{d^3p} = K \sum_{abcd} \int dx_a dx_b f_{a/p}(x_a, Q_a^2) f_{b/p}(x_b, Q_b^2) \times \frac{d\sigma}{dt}(ab \rightarrow cd) \frac{D_{h/c}(z_c Q_c^2)}{\pi z_c} \tag{1.5}$$

where $x_a = p_a/P_A$, $x_b = p_b/P_B$ are the initial momentum fractions carried by the interacting partons, $z_c = p_h/p_c$ is the momentum fraction carried by the final state hadron, $f_{a/p}(x_a, Q_a^2)$ are the parton distribution functions (PDFs) and the $D_{h/c}(z_c, Q_c^2)$ are the fragmentation functions for a parton with flavor c to fragment into h [7]. The Q^2 depend on the factorization scale chosen. Here the PDFs and the fragmentation functions require non-perturbative calculations, but fortunately they are measured by experiment.

1.2.2 Quark Gluon Plasma

QCD normally describes matter in which quarks are tightly bound to each other via the strong force. However, asymptotic freedom, discovered in 1973 [8], means that at high enough energies and temperatures quarks may exist in a deconfined state [9]. The study of quark matter in extreme conditions quickly became a growing field of research. The phase diagram for QCD matter is not known precisely, but an estimate of it is shown in Fig. 1.1. At sufficiently high temperature and/or density the system transitions to the deconfined state, known as a quark gluon plasma (QGP). Lattice QCD predicts this transition to occur at around $T = 192$ MeV, corresponding to an energy density of about 1 GeV/fm^3 [10]. A diagram of the energy density vs. temperature, indicating the transition point, is shown in Fig. 1.2. Here the y-axis, ϵ/T, is proportional to the degrees of freedom in the system, and the x-axis shows the temperature relative to the critical temperature T_c. An active area of research currently is the search for the existence and location of a critical point.

It is generally agreed that the RHIC experiments have succeeded in producing a quark-gluon plasma. Current investigations are focused on understanding the evolution of the collision and the dynamics of the produced medium. Below is a summary of what we know so far about the evolution of a heavy ion collision, including the role of heavy quark probes, and what we are still unsure of:

- When two nuclei at high energy collide, their partons (quarks and gluons)

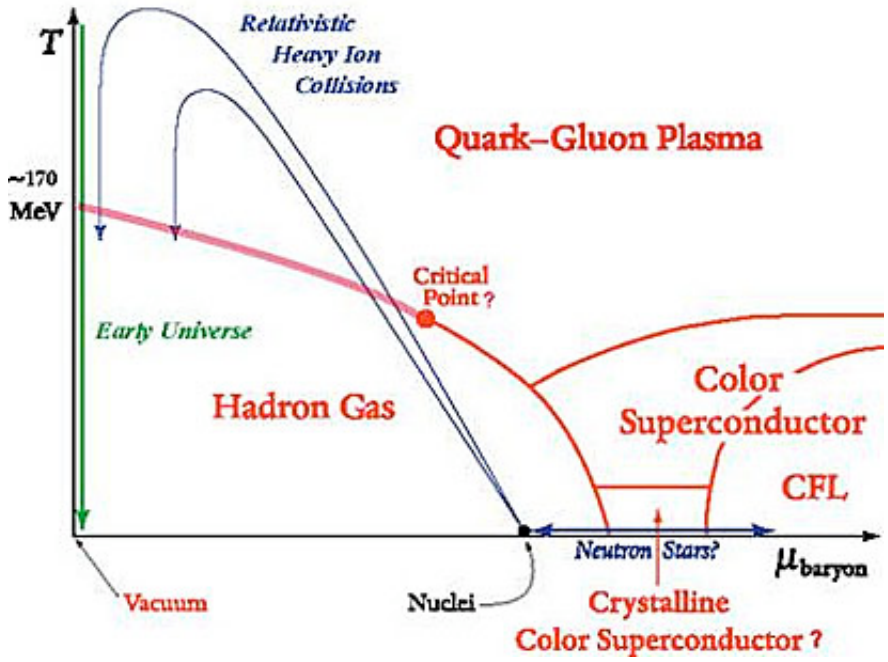

Figure 1.1: Theoretical phase diagram of quark matter as a function of temperature T and baryon chemical potential μ. From K. Rajagopal.

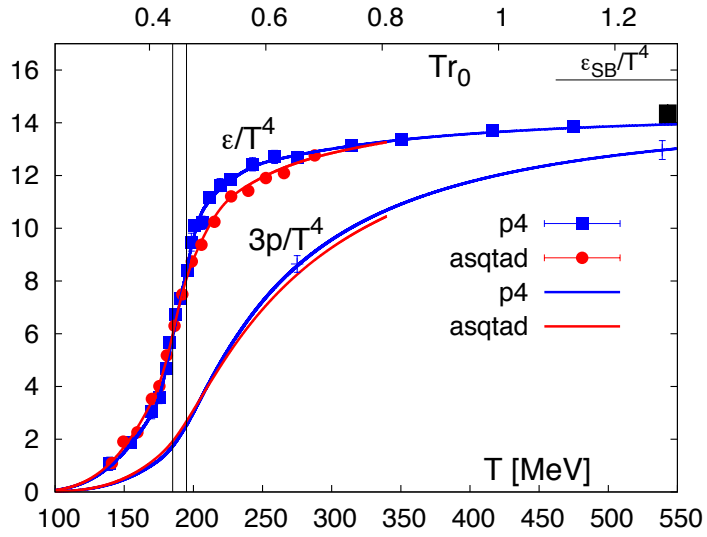

Figure 1.2: Lattice QCD results for the phase transition at $T_c \approx 170$ MeV, showing the results for different fermion actions. The band shows the phase transition region at 185 MeV $< T <$ 195 MeV [11]

may interact via hard scattering. This occurs when two high momentum partons interact to produce high momentum products, such as jets or heavy quarks. The amount of scattering that takes place depends on the distributions of partons inside the nucleus (see Sec. 1.3). From the study of d+Au collisions we have come to believe that parton densities are saturated at low fractional momentum, leading to suppression of particle yields in these collisions (Sec. 1.4.2). Further evidence for saturation has been found from the study of multiplicities in Au+Au collisions: these were found to be lower than expected (Fig. 1.3) [12], [13]. Charm is also found to be suppressed by a level similar to that of light mesons, an effect that is very relevant to this thesis [14]. It is important to

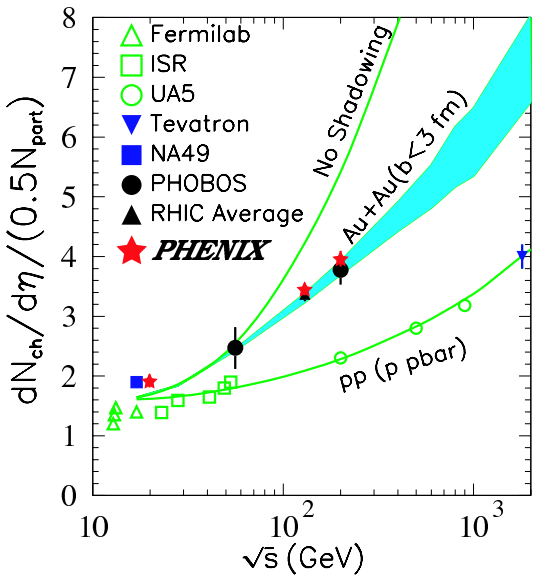

Figure 1.3: Measured multiplicity at PHENIX as a function of center of mass energy. A prediction based on pQCD alone is shown with the top green line, while the shaded band includes nuclear shadowing.

understand saturation so that we may disentangle it from other effects occuring at later stages in the collision.

- Shortly after the collision the interacting partons are thought to reach thermal equilibrium. The exact process by which this happens is not fully understood, but a thermalized medium is an initial condition required by theories describing later states (hydrodymanics, parton recombination [15] and see below). To match the data, the medium is estimated to thermalize very rapidly, at a time less than 1 fm/c [16].

- In the time between thermalization and freeze-out (see below), the ex-

panding medium may be described by hydrodynamical models. Because of the rapid thermalization, thermodynamic properties such as temperature and pressure are quickly well-defined, leading to a regime where hydrodynamics is applicable [17]. Hydrodynamics is suited to describing a strongly interacting medium, and describes a phenomenon known as "elliptic flow". This flow is due to the spatial anisotropy of the interaction region immediately after the collision, which resembles an almond for all but the most central (head-on) collisions. Because the hot quark matter is of oblong shape (it has a long axis and a short axis), pressure gradients are created. This causes the matter to flow as the spatial anisotropy is transferred into momentum space [18]. Even heavy quarks produced early in the collision are found to flow, presumably because they have lost energy in the medium [19]. From the amount of flow, the ratio of viscosity to entropy, η/s, may be measured. RHIC has found the produced medium to be almost a perfect fluid, with η/s only slightly above the limit of $\frac{1}{4\pi}$ conjectured by AdS/CFT calculations [20] [21].

- As the system continues to expand, the matter becomes too diluted to maintain a hydrodynamic state, and freeze-out occurs. As quarks and gluons lose energy, they become bound once again in a hadronic form. Because hadronization is a non-perturbative process, it is not well understood, and must be modeled using fragmentation functions that require data inputs [13]. At this time, the bare quarks may impart any features picked up in the medium (flow, energy loss) onto the formed

hadrons. This allows the experimental detection of these effects. One important effect arising from hadronization is the baryon anomaly: the baryon to meson ratio is higher in heavy ion collisions than it is in p+p collisions. [15]. There are various theoretical conjectures to explain this, including strong color fields [22]. It is also possible that charm baryons are enhanced, skewing the heavy flavor spectra in Au+Au collisions and making it seem that charm quarks are suppressed more than they really are [23].

Some of the most interesting probes of a heavy ion collision and the QGP are jets. They are produced through hard scattering early in the collision, then must travel through the medium before the byproducts can reach particle detectors. Jets were predicted to be suppressed in a QGP due to the interaction with the medium, and this was observed at RHIC [7] [24]. A comparison of jets in p+p and d+Au vs. Au+Au collisions is shown in Fig. 1.4; the suppression on the away side for central Au+Au collisions is clear. Because jets in d+Au collisions show no signs of suppression, the suppression in Au+Au is clearly a final state effect, and hence an effect of the medium. At RHIC, it is difficult to fully reconstruct jets in a heavy ion collision due to the vast number of particles created. For this reason hadron correlations are often used instead of jets, since high momentum hadrons correspond to jets. Detailed correlation studies have been done using light hadrons (pions, kaons, etc.), but few analyses so far have studied charm jets, which are more difficult to

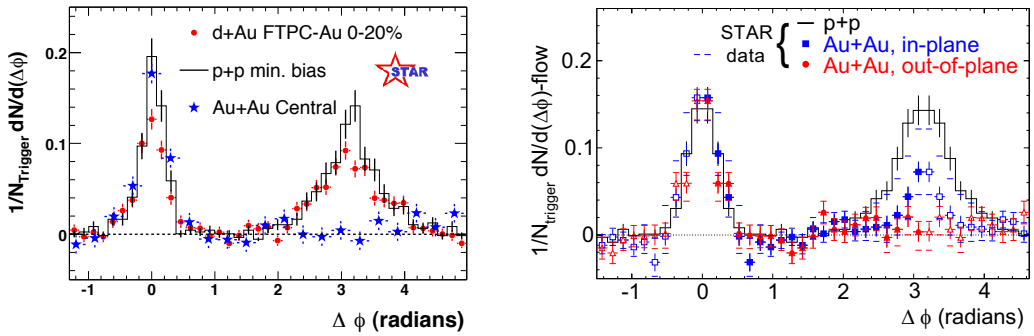

Figure 1.4: Dihadron per-trigger yield (a proxy for jet yield) as a function of azimuthal angle for p+p, d+Au, and Au+Au collisions at STAR [26]

analyze. Because charm quarks have been shown to lose a comparable amount of energy to light quarks in the medium, it is likely charm jets will show a similar away side suppression and modification [25] [14]. For this reason, the study of heavy quark correlations is important.

1.2.3 Collision systems

To study the quark-gluon plasma, RHIC uses Au+Au collisions at $\sqrt{s_{NN}} = 200$ GeV. Gold ions are sufficiently massive (197 nucleons) to cause a phase transition to the deconfined QGP when collided at that energy. Because of the complexity of the system in which thousands of particles are produced in each collision, it is necessary to have a baseline measurement to understand particle production at that energy. For this reason proton-proton collisions, also at $\sqrt{s} = 200$ GeV, are studied. If there are no effects on particle production and

propagation due to the created medium, experimental particle yields should be equivalent to the proton-proton yields scaled by the number of binary collisions. Any deviation from this scaling implies that the nuclear matter effects need to be accounted for.

Scaling of yields with respect to proton-proton collisions does not tell the whole story, though. There are separate effects that happen due to interactions with cold nuclear matter (both initial and final state effects) as well as interactions with the hot, dense medium. One way to isolate the cold nuclear matter (CNM) effects is to study d+Au collisions at the same energy. The CNM effects are not just useful as a baseline for Au+Au measurements, but are also interesting in themselves. Current d+Au analyses are probing initial state effects such as shadowing, as well as more exotic phenomena such as the Color Glass Condensate (see Sec. 1.4.2).

1.3 Parton Distributions Inside Nucleons

Modern atomic theory was born in 1909, when Ernest Rutherford's gold foil experiment was performed. At the time atoms were described by J. J. Thompson's "plum pudding" model, where negatively charged electrons ("plums") rotated through a positively charged medium (the "pudding"). Rutherford, along with his post doc Hans Geiger and his undergraduate research assistant Ernest Marsden, designed an experiment to confirm this model, involving a

beam of alpha particles projected at a thin gold foil [27]. A detector was fashioned surrounding the gold using zinc sulfide, which luminesces when struck by a charged particle, namely the recoiling alpha particles. According to the plum pudding model, a slight deflection should be seen in the alpha particles after they strike the gold, which would be an indication of the distribution of charge in the nucleus. Much to Rutherford's amazement, most alpha particles passed right through the foil undeflected, and the ones that did not were back scattered at very large angles. Rutherford took this to mean that charge and mass were not spread uniformly throughout the atom but were instead concentrated in a very small volume at the center, in a radius less than 1/4000th of the atom's diameter. The modern view of the atom had been uncovered, though what constitutes the nucleus remained a mystery.

A turning point came in the 1960's with the advent of the quark model. Murray Gell-Mann used group theory to create order for the wide variety of hadrons that had been discovered [28]. Quarks can be thought to form a fundamental representation of SU(3), assuming only three flavors exist; antiquarks make the complex conjugate representation. These can be decomposed into nine meson states, an octet and a singlet. Using the quantum numbers of charge and strangeness, the known mesons were found to fit this representation. A similar classification was devised for baryons. It was only much later that quarks were identified with partons in the nucleus. This was a difficult theory to verify since no free quarks can be observed (which we now know is due to asymptotic

freedom). Therefore to prove the quark hypothesis it was necessary to probe deep inside the nucleus, using scattering experiments similar to Rutherford's, but at a larger energy scale.

1.3.1 Deep Inelastic Scattering and Parton Distribution Functions

A series of deep inelastic scattering experiments, beginning in 1968 at SLAC, began to shed light on the inner structure of nucleons. If the nucleus only contained evenly-distributed charge, the results would be similar to what Rutherford expected from the plum pudding model: electrons would mostly pass through the proton and be scattered at small angles. This is in fact what was observed at low energy, however at high energy electrons were scattered at much larger angles, indicating that the proton is composed of point charges. Because it was not obvious that the particles observed inside nucleons were quarks they were named "partons", a term that is still used to refer to both quarks and gluons in the nucleus [29].

For a diagram of an electron-proton interaction, see Fig. 1.5. An electron with momentum k and energy E scatters off a proton of mass M and four-momentum p that is at rest in the lab frame. They interact by exchanging a virtual photon, which has momentum $q = k - k'$. This is also described by the

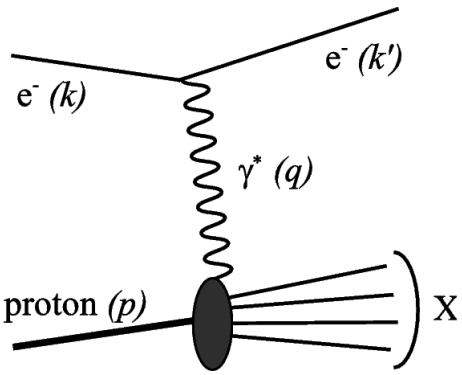

Figure 1.5: Kinematics of deep inelastic electron-proton scattering.

squared momentum transfer Q^2 [30],

$$Q^2 = -q^2 = -(k - k')^2 \tag{1.6}$$

The electron is scattered through an angle θ and has a final four-momentum k'. The hadronic system has a final momentum of p' and invariant mass W, defined by $W^2 = (q + p)^2$. The energy ν that the electron transfers to the hadronic system is

$$\nu = E - E' = \frac{q \cdot p}{M} \tag{1.7}$$

Other important variables include Bjorken-x, $x_B = \frac{Q^2}{2M\nu}$, which is the fraction of the proton's momentum carried by an individual parton. Also the fraction of the initial electron's energy carried by the virtual photon is defined as

$$y = \frac{\nu}{E} = \frac{q \cdot P}{k \cdot P} \tag{1.8}$$

When an electron is scattered and another electron appears in the final state,

the scattering has occurred through the neutral-current process. This means the interaction was mediated by either a photon or a Z boson. In a charged-current interaction (resulting in a final state neutrino) a W boson is exchanged. Because of the high mass of the W this type of reaction is suppressed at lower Q^2. For neutral-current reactions the final state lepton is measured, whereas in charged-current scattering the final hadronic states are measured as the final lepton is an undetectable neutrino.

For the case of scattering off a proton that is non-pointlike, the double differential cross section with respect to Q and ν can be written as

$$\frac{d^2\sigma}{dQ^2 d\nu} = \frac{4\pi\alpha_{em}^2}{Q^4}\frac{E'}{EM}\left[W_2(Q^2,\nu)cos^2\frac{\theta}{2} + 2W_1(Q^2,\nu)sin^2\frac{\theta}{2}\right] \tag{1.9}$$

where α_{em} is the electromagnetic coupling constant [3]. W_1 and W_2 are the structure functions, which measure the deviation of the differential cross section to that of simple elastic scattering involving point-like particles. In the elastic case, the structure functions reduce to

$$W_1^{el} = e_q^2\frac{Q^2}{4M}\delta\left(\nu - \frac{Q^2}{2M}\right) \qquad W_2^{el} = e_q^2 M\delta\left(\nu - \frac{Q^2}{2M}\right) \tag{1.10}$$

The structure functions may be experimentally determined, and related to the theoretical parton distribution functions (p.d.f.s). At leading order in the strong coupling α_s, the p.d.f.s give the probability for a parton to carry a fraction of the overall momentum, x_i. When the structure functions are

integrated over each constituent parton using the p.d.f. as weighting, we get

$$W_1 = \sum_i \frac{1}{2} e_i^2 f_i(x_B) \qquad W_2 = \sum_i M e_i^2 f_i(x_B) \frac{x_B}{\nu} \tag{1.11}$$

where the f_i are the p.d.fs. From this comes a definition of the structure functions F_1 and F_2:

$$F_1(x) \equiv W_1 = \frac{1}{2} \sum_i e_i^2 f_i(x) \tag{1.12}$$

and

$$F_2(x) \equiv \frac{\nu W_2}{M} = \sum_i e_i^2 x f_i(x) \tag{1.13}$$

F_1 and F_2 are solely functions of x, not of Q^2; this is known as Bjorken scaling [4]. It holds in the limit of Q^2 and $\nu \to \infty$, otherwise a Q^2 dependence is seen (see Sec. 1.3.3. The scaling was confirmed experimentally, leading to some confusion because it was shown that scaling behavior only holds for a field theory that is asymptotically free (coupling approaches 0 at a high renormalization scale). Of course the asymptotic freedom of QCD was discovered shortly thereafter, so Bjorken scaling was found to accord with physical theories. As a further note, the parton model allows x_B, an experimental obserable, to be identified with x, the theoretical momentum fraction carried by the struck parton. From the above structure function definitions comes the

Callan-Gross relation [31],

$$2xF_1(x) = F_2(x) \tag{1.14}$$

which holds for spin 1/2 fermions. Because experimental results have confirmed this relation holds, we have come to believe that the partons inside the nucleons are fermions (quarks).

The quark-parton model gave a consistent description of the DIS results even before the theory of QCD was formulated. Quarks appeared to act as free particles inside the nucleons because an electron probe interacts with a lifetime $\tau \sim 1/Q^2$, which is shorter than the parton lifetime. The partons therefore do not have time to interact with each other during the scattering process. Furthermore, it predicted the existence of gluons due to missing momentum in the nucleons. When F_2 is integrated it gives the total momentum carried by the charged partons: this is found to be closer to 0.5 than to 1, implying that only half the total momentum can be detected [3]. The rest is carried by something that is invisible to electromagnetic or weak probes. It was later discovered that gluons fit this criteria, because they are only subject to the strong force.

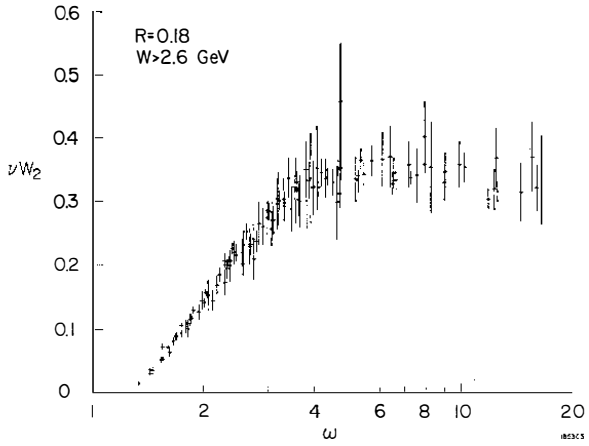

Figure 1.6: Scaling behavior of νW_2 as a function of $\omega = 1/x_B$ for a variety of Q^2, as measured by MIT-SLAC collaboration [5]

.

1.3.2 Experimental Determination of Structure Functions

The first experiment designed to detect quarks was performed at SLAC in 1968. SLAC is a linear accelerator that was initially able to accelerate electrons to 20 GeV to collide with a stationary proton. An electron beam in the energy range 4.5-20.0 GeV was directed through either a liquid hydrogen or a deuterium target, and the recoil electron was measured at a variety of angles [5]. A measure of νW_2, which is proportional to F_2, is shown in Fig. 1.6. The points were taken at a variety of Q^2 values from 1 GeV$^2/c^2$ to 12 GeV$^2/c^2$ and above. In Fig. 1.7 we see νW_2 as a function of Q^2 for a fixed x, showing that at least at $x = 0.25$ Bjorken scaling is clearly demonstrated.

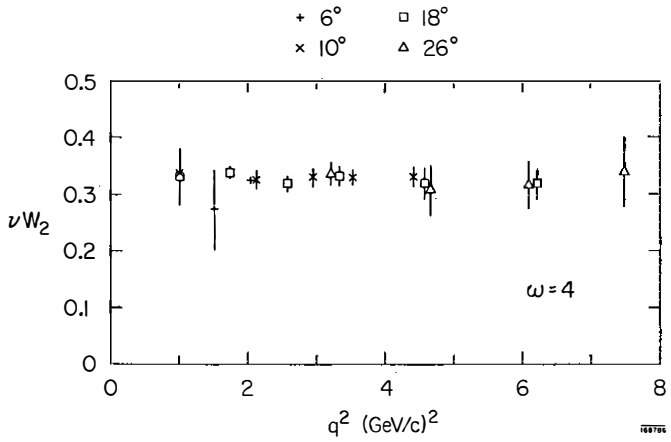

Figure 1.7: Value of νW_2 for $x_B = 1/\omega = 0.25$ as a function of Q^2 from MIT-SLAC collaboration [5].

Extensive research into deep inelastic scattering effects at high energy was performed at the HERA accelerator at the DESY lab in Hamburg, Germany. It was the world's first $e - p$ collider, and it consisted of a 6.3 km circumference ring that collides electrons or positrons at 27 GeV with protons at 820 GeV. Four experiments were set up around the ring, and the two which were most important for studying parton PDFs were H1 and ZEUS. The collider began operating in 1992 and finished operations in 2007. It provided a wider kinematic range for a more detailed study of DIS effects. As can be seen from the HERA data, Bjorken scaling tends to be violated at very small x (Fig. 1.8) [32]. For scaling to hold, the initial transverse momentum of the partons is supposed to be small. However at small x the partons radiate more hard gluons, leading to logarithmic scaling violations. This effect is more pronounced as Q^2 increases.

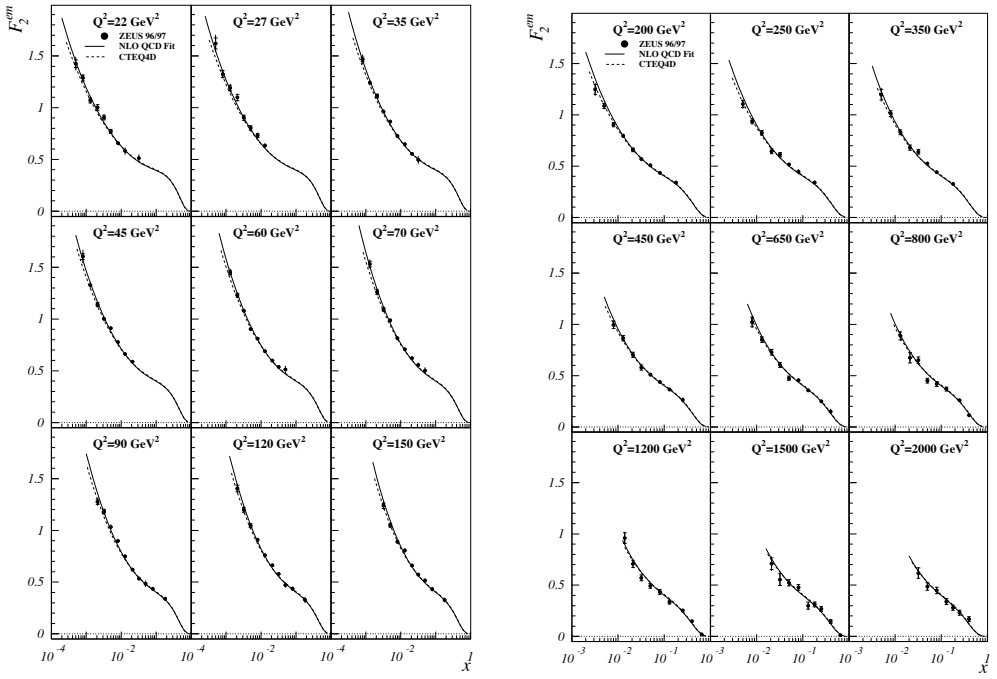

Figure 1.8: ZEUS measurement of F_2 as a function of x for variety of Q^2 values [32]. Comparison of data with NLO QCD predictions is shown.

1.3.3 Evolution Equations

While it is true that the structure functions are mostly independent of Q^2, they do show a slight growth with Q^2 as x decreases. An example of this can be seen in Fig. 1.9. This scaling violation shows the failure of the quark parton model, and the need for the "improved" quark parton model, that is, a model including QCD effects. At large x there is no predicted dependence on Q^2 since the distribution is here dominated by valence quarks; no more partons besides the three quarks are visible with a higher energy probe. However at smaller x the distributions are dominated by gluons and sea quarks, which evolve: gluons split into quark pairs, and quarks radiate gluons. This evolution is descriped by the DGLAP equation [33] [34] [35]:

$$\frac{\partial}{\partial \ln Q^2}\begin{pmatrix} q \\ g \end{pmatrix} = \frac{\alpha_s(Q^2)}{2\pi}\begin{bmatrix} P_{qq} & P_{qg} \\ P_{gq} & P_{gg} \end{bmatrix} \otimes \begin{pmatrix} q \\ g \end{pmatrix} \tag{1.15}$$

Where q and g are the quark and gluon distributions, and where $\otimes$ is a convolution in x as given by $f \otimes g(x) \equiv \int_x^1 \frac{dy}{y} f(\frac{x}{y}) g(y)$. The P_{fg} are the Altarelli-Parisi splitting functions, describing the probability of g to split into a daughter f along with other products. They may be expanded in powers of α_s,

$$P_{ij}(x, Q^2) = \frac{\alpha_s}{2\pi} P_{ij}^{(1)} + \frac{{\alpha_s}^2}{2\pi} P_{ij}^{(2)} + ... \tag{1.16}$$

Calculations at next-to-leading-order (NLO) keep only the first two terms.

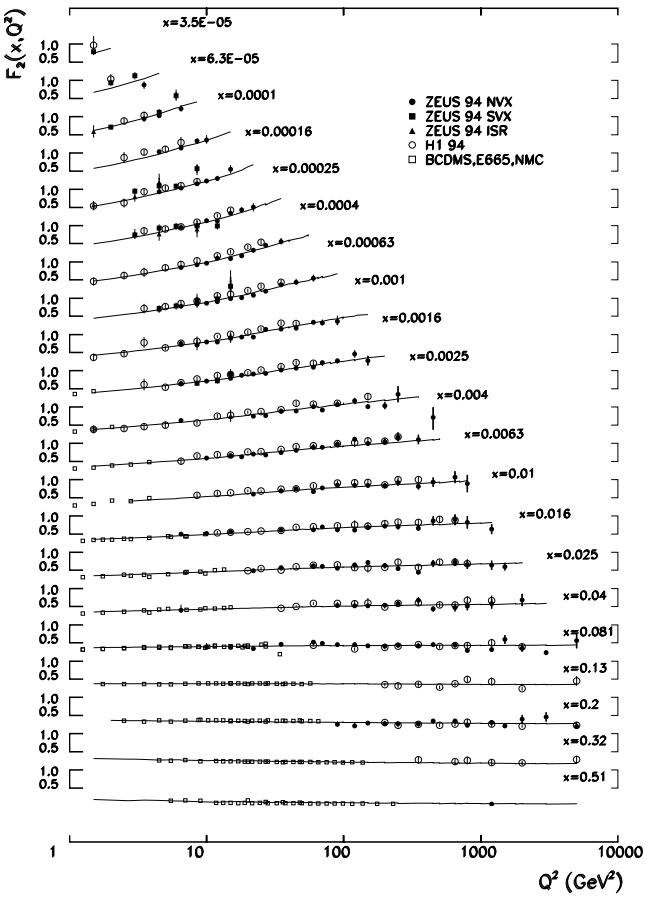

Figure 1.9: F_2 as a function of Q^2 for a variety of x values. Data taken from HERA experiments [32].

The necessity of introducing a factorization scale, μ_F^2, to remove collinear singularities leads to large logarithms that must be summed over in solving the DGLAP equations. Two regions require special handling of singularities. The first is the collinear region, involving terms of the form $\alpha_s \ln(Q^2/Q_0^2)$, that corresponds to emitted gluons that are strongly ordered in transverse momentum. The other is the soft region (terms like $\alpha_s \ln(1/x)$), where the gluons are strongly ordered in longitudinal momentum. The collinear region corresponds to large Q^2 and moderate x, and this is handled by the DGLAP equation. The soft region, though, corresponds to low x, which means that the terms of order $\alpha_s^n \log^{n-1}(1/x)$ cannot be dropped because they are of the order 1. NLO and NNLO DGLAP does not keep enough terms to handle this properly. A resummation of the logarithm terms leads to the BFKL equation, which describes the low x region [36] [37]. Because there is no longer ordering in tranvserse momentum (k_T), the BFKL equation gives the gluon density, $f_g(x, k_T^2)$ without integrating over k_T. It is of the form

$$\frac{\partial f_g}{\partial \ln(1/x)} = \lambda f_g \tag{1.17}$$

which for small x has a solution of the form,

$$f_g \sim x^{-\lambda} \tag{1.18}$$

where $\lambda = 12\alpha_s \ln(2/\pi)$ [38]. BFKL predicts the gluon distributions to grow exponentially at small x, leading to a violation of unitarity. This is resolved

by saturation effects involving gluon recombination; this is discussed in the next section.

As an aside, the QCD evolution equations cannot predict the parton distribution functions a priori. They can found using an initial value at some Q_0^2 and evolved from that starting point. Therefore experimental determination of structure functions is still essential.

1.4 Nuclear Modification Effects

Once the structure functions for protons and neutrons were understood, it was thought that structure functions of more complex nuclei would show little difference. The energy of the probe used in DIS is greater than any strong force energy scales known to exist within nuclei. Then in 1982 the European Muon Collaboration measured the structure functions of iron and found that it deviates from the values for those of a deuterium nucleus scaled up by the number of nucleons [39]. It was then found that the structure function F_2 for a nucleus exhibits either a suppression or an enhancement relative to that of deuterium depending on the x range probed. An outline of the effects is given below [40]:

- $x < 0.05 - 0.1$ constitutes the "shadowing" region. Here the ratio of F_2

in nuclei compared with deuterium,

$$R_{F2}^{A}(x,Q^2) = \frac{F_2^A(x,Q^2)}{AF_2^{nucleon}(x,Q^2)} \tag{1.19}$$

is less than 1. In this equation, $F_2^{nucleon} = F_2^{deuterium}/2$. This effect is described in more detail in the following section.

- $x \approx 0.1 - 0.2$ is known as the "anti-shadowing" region. Here the ratio R_{F2}^{A} is slightly larger than 1. It has been hypothesized that partons at lower x values are depleted because the uncertainty principle smears out their spatial distributions, causing them to fuse. Conservation of momentum then requires an enhancement of partons at larger values of x.

- $x \approx 0.2 - 0.8$ is the location of the "EMC effect", where R_{F2}^{A} decreases below 1 until it reaches a minimum at $x \approx 0.6$. While we are still lacking an understanding of the mechanisms that cause this effect, some of the theories include excess pions in the nucleus, effects due to the nuclear binding energy, or even nuclear "swelling."

- $x > 0.8$ is the region which exhibits Fermi motion, causing the ratio to again rise above 1. This arises from convolving the structure function for a free nucleon with the momentum distribution within the nucleus.

1.4.1 Shadowing at Low x

A decrease in the R^A_{F2} ratio with decreasing x is a well studied experimental result. Shadowing begins around $x \sim 0.1$ with a sharp decrease in R^A_{F2} until the effect saturates at very low x values. The amount of shadowing increases for larger nuclei, and decreases for higher values of Q^2 [41].

Some models of shadowing relate the supression to the multiple scattering that occurs when an external probe interacts with a nucleus. In hadronic collisions, the photon probe interacts with each nucleon individually, and the overall amplitude for the interaction with a nucleus is the sum of the individual nucleon interactions [40]. According to the vector meson dominance model (VMD), the interacting photon in DIS must be decomposed into all the states it may fluctuate into, which include the bare photon, electromagnetic pair states (e^+e^-), and hadronic states [42]. These hadronic states are composed of quark-antiquark pairs with the same quantum numbers as the photon, which means they become vector mesons. If the photon has fluctuated into a vector meson state the interaction effectively becomes hadronic. Because of the multiple scattering nature of these interactions, the vector meson will interact with the surface nucleons more frequently than with the nucleons in the interior; this allows only a fraction of the overall nucleons to be probed, which looks like suppression. This suppression begins to occur when the coherent limit is reached, that is, when the photon interacts with the nucleus as a whole rather than with individual nucleons. The time during which the

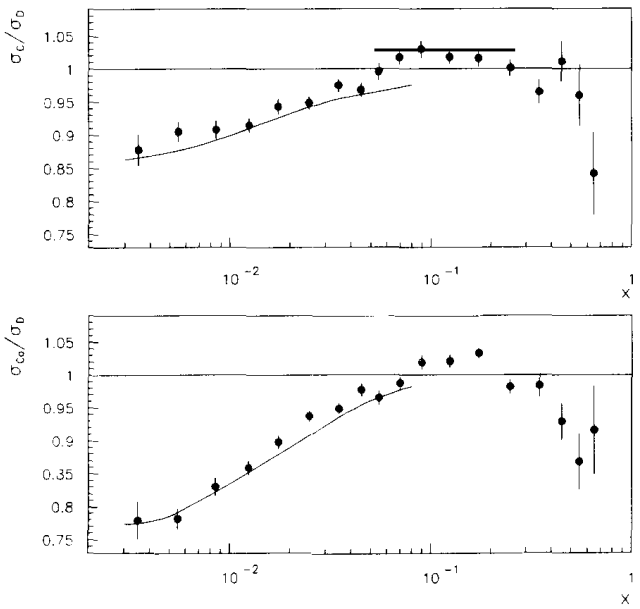

Figure 1.10: Comparison of generalized vector meson dominance model calculation to NMC data for carbon (top) and calcium (bottom). [40]

photon interacts with the nucleon in the nucleus's rest frame is given by

$$\tau \sim \frac{1}{Q} \times \frac{E_{lab}}{Q} \approx \frac{1}{2m_{nucleon}x} \tag{1.20}$$

where E_{lab} is the energy of the nucleon in the lab frame, and $\frac{Q}{E_{lab}}$ is the Lorentz factor. When τ is larger than the nuclear radius R_A the photon interacts with the entire nucleus, and from the above we get that for this to happen $x < 1/(2m_{nucleus}R_A) \sim 0.1A^{-1/3}$. This approximately corresponds to the x range at which the transition from shadowing to antishadowing occurs [41]. A comparison of a vector meson shadowing calculation to data from the CERN NMC experiment is shown in Fig. 1.10.

Another approach attempts to explain shadowing through parton recombination. Partons at low x inside a nucleon of momentum P_N are spread out a distance $\Delta z \sim 1/(xP_N)$ due to the uncertainty principle. The nucleons are themselves separated by $2R_N$ in the lab frame (where R_N is the nucleon radius) which corresponds to $\Delta z_N \sim 2R_N(M/P_N)$ in the Breit frame. The Breit frame is an infinite momentum frame where four momentum of the photon is $(0, 0, 0, -Q)$. For $x < 1/(2R_N M)$ the partons are spread out enough that they start to overlap with partons from other nucleons: this is the beginning of shadowing. When an x value of $1/(2R_A M)$ is reached (R_A being the nuclear radius), the parton is able to interact with the entire nucleus. Since partons at low x are mainly gluons, they tend to interact by fusing, $g \to gg$, thus leading to a reduction of partons at very low x. This also explains antishadowing, because the depletion of partons by recombination at low x must be balanced by an enhancement at higher x to conserve momentum. Figure 1.11 shows a comparison of shadowing results obtained from the NMC experiment at CERN to recombination theory predictions, which are shown to be in good agreement. The partonic recombination scheme does not directly conflict with the VMD theory, because multiple scattering in the rest frame can be viewed as recombination in the infinite momentum frame.

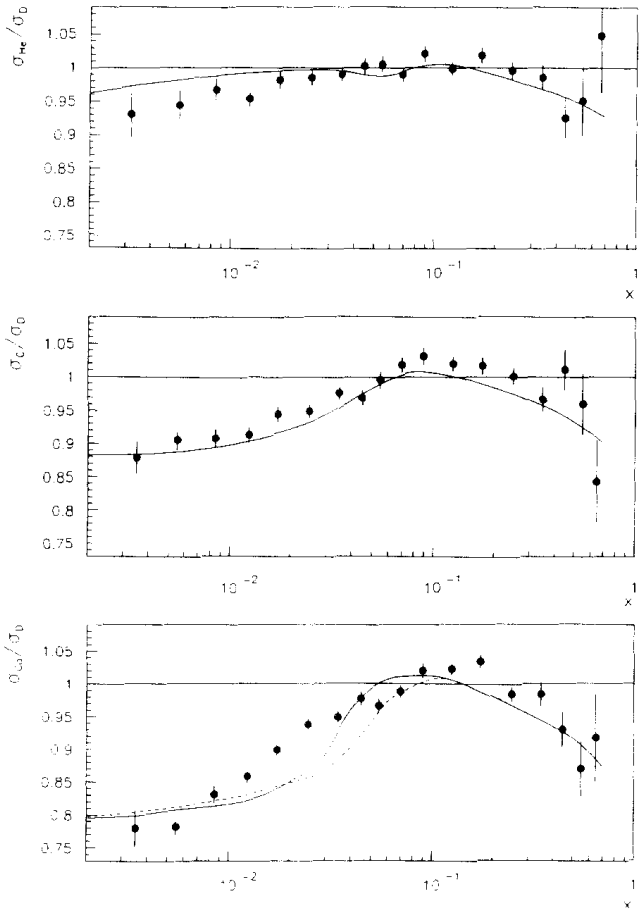

Figure 1.11: Partonic recombination calculations from Berger and Qiu (solid lines) and Close and Roberts (dashed line) compared with NMC results for helium, carbon, and calcium [40].

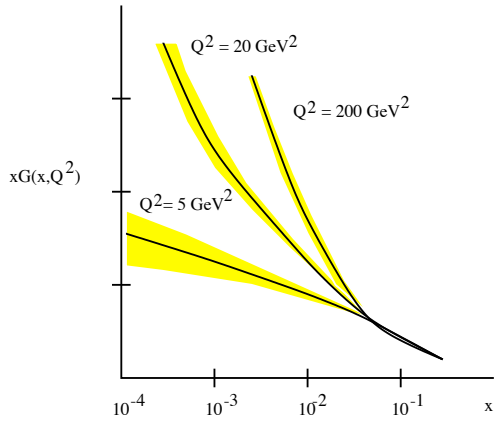

Figure 1.12: ZEUS data showing the rapid grown of the gluon structure function $xG(x, Q^2)$ as a function of x for different Q^2 values.

1.4.2 Color Glass Condensate

The saturation hypothesis of parton shadowing was eventually formulated into a coherent framework, known as the Color Glass Condensate (CGC). The BFKL evolution equation suggests that at low x the distributions show a power law growth (see Fig. 1.12). This leads to a violation of the Froissart unitarity bound [43], which stipulates that a cross section cannot grow faster than $(\ln E)^2$. A solution to this unitarity violation was formulated in the CGC model: gluons saturate the low x region in a dense, weakly coupled state (condensate) full of slowly evolving, disordered fields (similar to a glass) [44].

A high energy nucleus contains many short-lived fluctuations at a non-perturbative scale. If the time scale during which they exist is shorter than the interaction time of the probe used, they are invisible. Relativistic nuclei, though, have

their internal time scales dilated, so these fluctuations do look real when they are observed. This causes the nucleus to look denser at higher energies because there are more partons (predominantly gluons) at low x. The growth in the number of gluons obeys BFKL dynamics and remains linear until partons begin to overlap, and recombination becomes favorable. The crossover to the condensate regime begins at a saturation scale,

$$Q_s^2 \sim \rho\alpha_x \sim \frac{\alpha_s x G_A(x, Q_s^2)}{\pi R_A^2} \tag{1.21}$$

where $\rho \sim \frac{xG_A(x,Q^2)}{\pi R_A^2}$ is the number of gluons per unit area. For a diagram of the location of the saturation region in phase space, see Fig. 1.13. The partons at higher x are greatly slowed down by time dilation, and form frozen sources of color field. These give rise to a disorderly, classical gluon field at lower x.

Similar to earlier saturation models, the CGC predicts particle production to be suppressed at a range of approximately $x \lesssim 0.01$, corresponding to the forward rapidity region of collider experiments. CGC also predicts the existence of mono-jets, in which only one side of a back-to-back jet pair escapes from the dense condensate. Currently studies of single particle production and correlations at high rapidity are being undertaken to search for evidence of the existence of the CGC.

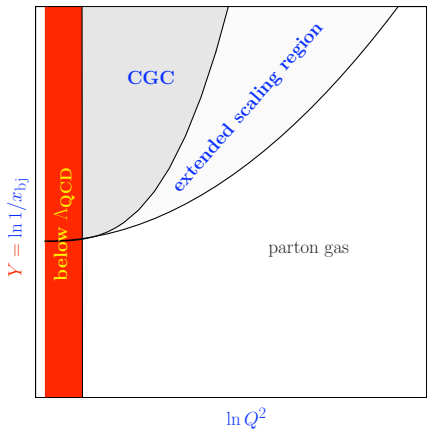

Figure 1.13: Location of CGC in phase space, as a function of Q^2 and x_b. The region is bounded by $Q_s(x_{bj})$ [45].

1.5 Experimental Detection of Cold Nuclear Matter Effects at RHIC

Experimental evidence for nuclear shadowing has existed for several decades. With RHIC, though, collisions are at high enough energy to probe the kinematic range where effects of the CGC could be observed. This would occur at an x range below 0.01, as opposed to an onset of shadowing effects at $x \approx 0.1$. Though CGC gluon suppression will cause effects in a Au+Au collision, the natural system to observe this would be in d+Au. This is because medium effects would obscure CGC suppression, whereas any change in d+Au observables (relative to those in p+p) would be caused solely by cold nuclear matter interactions. This is because the deuteron is so loosely bound it effectively acts like a proton, but without the isospin effects.

There are two main observables used to test for the presence of modification caused by the CGC. The first is particle yield suppression, especially at a p_T value that is below the saturation scale. This scale is given by $Q_s^2 \approx 0.13 N_{coll} e^{\lambda y}$ where $\lambda \sim 0.3$ as determined by HERA data [46]. The yield suppression is quantified by

$$R_{dAu} = \frac{Yield(d+Au)}{< N_{coll} > Yield(p+p)} \tag{1.22}$$

where N_{coll} is the number of binary collisions that occur in a collision. The number of hard scattering processes that occur in a collision is expected to be proportional to N_{coll}. Suppression of particle yields is expected because gluons are suppressed at low x, so fewer are available to interact to create hadrons in the collision. This is especially evident at large forward rapidity (defined as the deuteron-going direction) because there the low x partons in the gold nucleus are probed using the valence quarks in the deuteron. The opposite is expected in the backward (gold-going) direction: the kinematics shift soft particle production to backward rapidities in d+Au collisions, so an enhancement is seen relative to the p+p baseline. Forward suppression of hadrons is seen by BRAHMS, PHENIX, and STAR [47] [48] [49], and the measurements agree with each other as well as with the CGC predictions [46] (see Fig. 1.14). An enhancement at mid rapidity relative to p+p is also seen, and this is expected due to the Cronin effect [50]. Because of this effect, particle production at $p_T > 2$ is enhanced due to initial state scattering. This

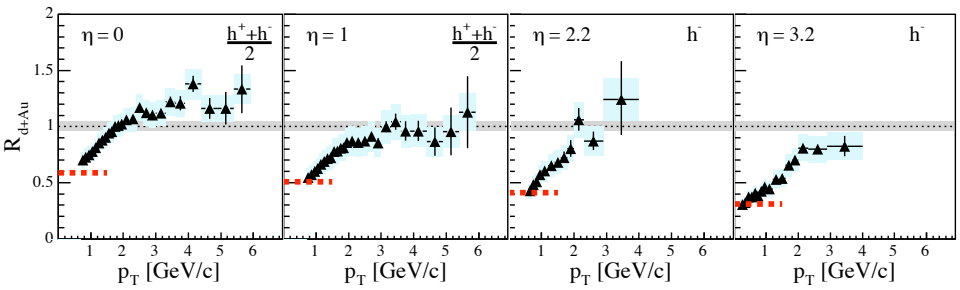

Figure 1.14: Suppression at at a range of forward rapidities in d+Au collisions as measured by BRAHMS [47]. Plotted is R_{dAu} of hadrons as a function of p_T for four rapidity ranges.

effect is in fact predicted to be even stronger at forward rapidity, so the fact that suppression at this p_T range is seen in d+Au instead is evidence of the large amount of suppression. PHENIX has also measured R_{dA} at backward rapidity and found it to be enhanced relative to p+p; it is possible that some of the suppression at large rapidity is due to the shifting of soft production to backward rapidity [51].

The other major predicted observable that is evidence of CGC effects is the presence of monojets. In the nuclear interaction, if a dijet is created, one of the jets may be absorbed in the dense gluonic medium. Therefore we should see a suppression in the dijet (or equivalently dihadron) yield because only one jet will escape. It is also expected the correlation functions may be broadened due to multiple interactions within the CGC. Studies have been done at both STAR and PHENIX that measure the azimuthal correlations of dihadrons, where one is in the forward region and the other in the central [52] [49].

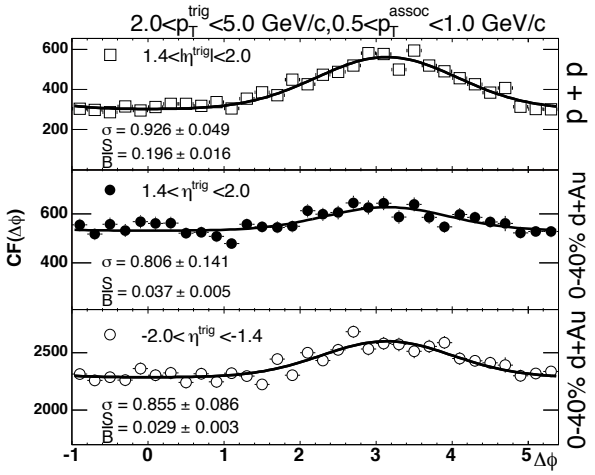

Figure 1.15: Measurement of dihadron correlation functions in PHENIX for forward rapidity p+p collisions (top), d+Au collisions (center), and backward rapidity d+Au collisions (bottom) [48].

This probes a low x region, though not as low as is seen with forward hadrons alone. So far neither experiment has clearly detected either jet suppression or azimuthal broadening, though STAR sees a slightly larger effect than PHENIX (see Figs. 1.15, 1.16).

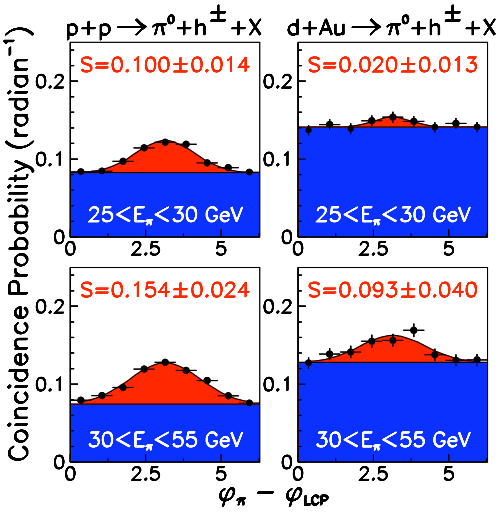

Figure 1.16: STAR pion-hadron correlations in p+p collisions (left) and d+Au collisions (right) at forward rapidity as a function of $\Delta\phi$ for different pion energy ranges [49].

Chapter 2

Heavy Flavor Production in Hadronic Collisions

When the quark model was postulated by Murray Gell-Mann in 1964 [53], only three flavors were needed to explain the experimental data up to that point: up, down, and strange. Because four, not three, leptons were known then (e, μ, ν_e, and ν_μ), Bjorken and Glashow speculated that having a fourth quark would provide more symmetry in the nascent standard model [54]. A more compelling argument for the charm quark was recognized a few years later by Glashow based on the electroweak theory of Weinberg and Salam [55]. In order to be renormalizable, the theory requires "strangeness changing neutral currents", where s quarks decay into d quarks [56]. These transitions are not seen in nature, though: for example, $K^+ \to \mu^+\nu$ is observed, but the neutral current $K^0 \to \mu^+\mu^-$ is not. However, the term that gives rise to these strangeness changing neutral currents is cancelled when a new, heavier quark

is added into the theory. The addition of a new quark, the charm quark, is known as the GIM mechanism [57]. Because of these theoretical developments it was no surprise when experiments detected the first charmed particle, the J/Ψ, in 1974.

2.1 The Discovery of Charm

The first particle containing charm to be discovered was the J/Ψ, which is composed of $c\bar{c}$. This is most likely because it exhibits a very clean, narrow peak in the e^+e^- spectrum. The discovery was announced by two different experiments on the same day: November 11th, 1974. It was discovered at the BNL AGS facility by a MIT group led by Samuel Ting, where it was named the J particle [58]. At this experiment, 31 GeV proton beams were collided with a Be target. A peak was found in the e^+e^- spectrum at 3.1 GeV. The J/Ψ was also discovered by the SPEAR experiment at SLAC-LBL, with a group led by Burton Richter and Gerson Goldhaber, where it was named the Ψ [59]. This experiment collided electrons and positrons together at energies of up to 4 GeV each. Because of the simultaneous nature of the discovery, both groups got credit and the particle was given a combination of both names. Only 10 days later SPEAR announced the discovery of the Ψ', another $c\bar{c}$ bound state with a mass peak at 3.69 GeV [60].

The mass peak observed for the J/Ψ was unexpectedly narrow: it was pre-

dicted to be even wider than that of lighter resonances because the high mass should give the decay electrons a large momentum kick, smearing the kinematics of the reaction. This is partially explained by the Zweig rule, which states that particle decays involving the annihilation of a quark and an antiquark are suppressed [61]. The only way for the J/Ψ to decay is by the c and $\bar{c}$ annihilating: this is because $J/\Psi \rightarrow D^- D^+$ is prohibited by phase space. The suppression of this effect leads to a longer lifetime, and hence to a narrower peak. A better description of the width is given by the "super Zweig rule," formulated by David Politzer and Thomas Appelquist [62]. This includes the effects of asymptotic freedom and the QCD linear confinement potential to predict the long lifetime of the J/Ψ.

To be sure that what they had detected is charm, experimentalists turned their search to open charm particles. These are particles that contain one charm quark and at least one other (lighter) quark. This discovery occurred in 1976, again with the SPEAR experiment. A team led by Goldhaber and Francois Pierre found mass peaks in the $K\pi$ and the $K\pi\pi\pi$ spectra around 1.87 GeV. The presence of kaons indicated charm, since the strange quarks in the charm are produced by $c \rightarrow s$ charged current weak decay. Further observations involving neutrino emulsion experiments at FNAL and CERN confirmed the discovery of the D^+/D^- and the D^0, as well as the χ_c [56].

2.2 Discovery of Bottom

Similarly to charm, the bottom quark was first discovered through the observation of a resonance state, in this case the Υ. It was discovered in 1977 at Fermilab experiment 288 (headed by Leon Lederman), which collided a proton beam with a platinum target. A small peak was found in the dimuon spectrum at a mass of approximately 9.5 GeV [63]. Shortly afterwards two higher mass resonances, the Υ' at a mass of 10.0 GeV, and the Υ'' at 10.4 GeV, were identified. These discoveries were confirmed at DORIS (e^+e^- collider at DESY in Germany) and at the Cornell e^+e^- collider [64].

2.3 Heavy Quark Production in Hadronic Collisions

In order to study heavy quark production at RHIC, we need to have a good theoretical understanding of rates and production mechanisms. As with other hard QCD processes, heavy quark production obeys the factorization theorem, meaning that the cross section is calculable from the perturbative hard scattering process and the non-perturbative p.d.f.s and fragmentation functions [65]. This is true even for lower momentum processes because the large quark mass sets the hard scale. Charm production, however, is notoriously hard to predict. Since the earliest experimental results it was found that actual charm

production in hadronic collisions lies well above leading order theoretical expectations. This indicates that higher order corrections play a large part in charm processes.

Heavy quark yields are calculated using a perturbative QCD expansion (pQCD). In pQCD, when multiple scales are present, terms arise that are proportional to the logarithms of these scales. For heavy quarks, the large mass introduces another scale and hence more logarithm terms, beyond those already proportional to the scales set by s and Q^2. Because the quark mass (M) is much higher than the typical parton mass (m), terms of the order m/M are dropped in the calculation [65]. This is expected to be valid because both the charm and bottom masses are much greater than Λ_{QCD}. However the charm mass is of the order of the nucleon masses, which are described by a nonperturbative scale, so the argument for charm being heavy is not so clear cut [66]. Also, leading order calculations do not accurately describe the charm x_f distribution, the quarkonium absorption in nuclear matter or the correlation of charm hadrons with quantum beam properties, as well as the overall cross section [67]. Including higher twist effects could partially explain these discrepancies. These effects, along with the uncertainty in the quark mass, the magnitude of α_s, and uncertainty in the structure functions make the cross section very difficult to predict.

If next-to-leading order effects are included, there are three main ways that charm can be created [68]:

- **Pair creation** is the leading order process, and it includes $gg \to Q\bar{Q}$ and $q\bar{q} \to Q\bar{Q}$. Because antiquarks are necessarily sea quarks, and these are less abundant than gluons in the nucleus, the gluon fusion process is dominant. This will tend to produce charm pairs that are back-to-back in azimuth. Gluon radiation is possible in either the initial or final state, but this will mostly shift the kinematics of the process rather than change the rate.

- **Flavor excitation** is a next-to-leading-order (NLO) effect, involving the processes $Qq \to Qq$ and $Qg \to Qg$. This involves a heavy quark being put on its mass shell by a parton in the other beam, which means a heavy quark already has to be present before the interaction takes place. It is generally created through a gluon splitting process, $g \to Q\bar{Q}$, so the total interaction is effectively $gq \to Q\bar{Q}q$ or $gg \to Q\bar{Q}g$. Heavy flavor distributions vanish for $Q^2 < m_Q^2$, so the virtuality must be greater than m_Q^2 for this process to occur. One heavy quark is involved in the hard scattering vertex.

- **Gluon splitting** involves $g \to Q\bar{Q}$ in either the initial or final state. No heavy flavor is involved in the hard scattering. The gluon splitting tends to occur in the final state, since in the initial state the time-like gluon is restricted to have smaller virtuality (also this would be classified as flavor excitation in our scheme).

These three methods of charm production cover different kinematic ranges.

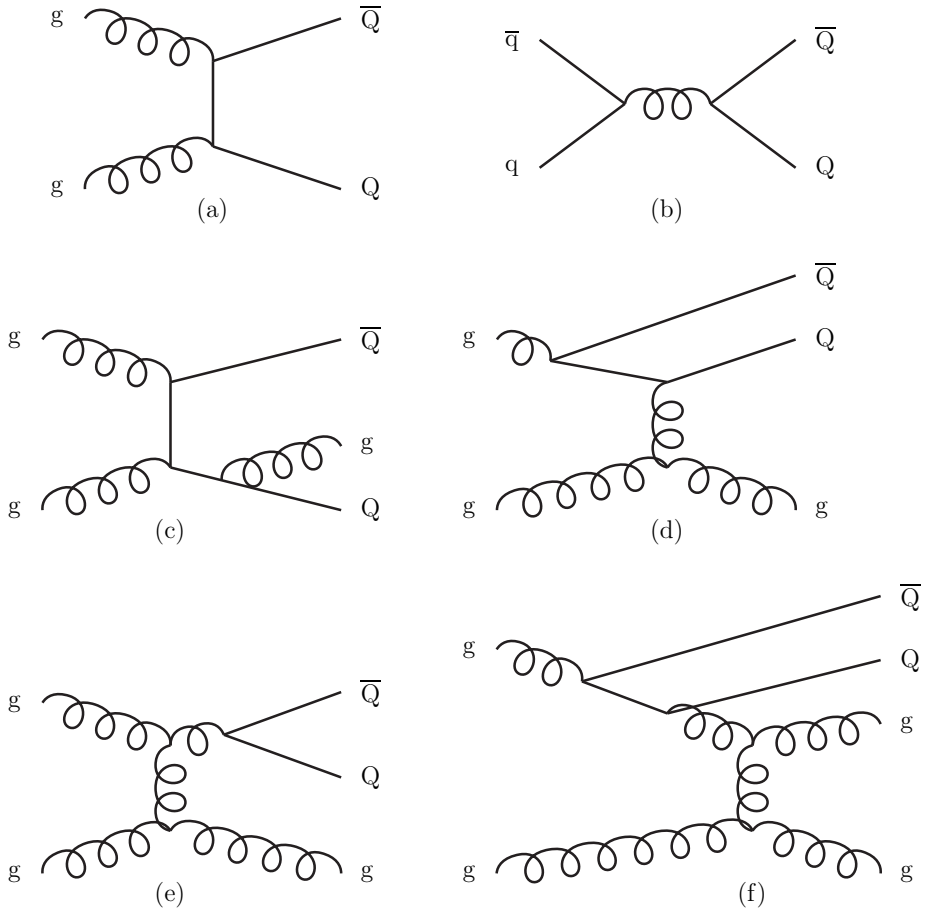

Figure 2.1: Heavy quark production mechanicsm, from [68]. (a, b) are leading order fusion diagrams, (c) is same but with final state gluon radiation, (d) flavor excitation, (e) gluon splitting, (f) gluon splitting but similar to flavor excitation.

At the lowest center of mass energy, pair creation dominates. As the energy increases flavor excitation overtakes it, and at the highest energies gluon splitting is the dominant process. This is because flavor excitation and gluon splitting require more phase space, so they turn on at higher energies. At RHIC energies of $\sqrt{s} = 200$ GeV, the charm cross section for flavor excitation is several times as large as that for pair creation, whereas for bottom, pair creation still dominates (see Fig. 2.3). It is also possible to segregate the different processes into separate kinematic ranges. For example, contributions from intrinsic charm (via flavor excitation) are enhanced in the low p_T region, where low momentum sea quarks can combine with collinear valence quarks to produce heavy hadrons [67]. The lower p_T limit is still bounded by the charm quark mass, as mentioned above. Furthermore, as described in [68], pair creation yields a strong back-to-back peak in $\Delta\phi$, while the other processes show little to no peak (the same is true to a lesser extent in the invariant mass spectrum of heavy quark pairs). This means that the azimuthal distribution can give insight into which processes are producing the heavy flavor.

2.3.1 Calculating the Charm Cross Section

The two main schemes used to calculate cross sections in QCD are next-to-leading order (NLO) and fixed-order-next-to-leading logarithm (FONLL). The NLO cross section is the partonic cross section directly calculated from QCD, with inputs being the heavy quark mass and the renormalization and factor-

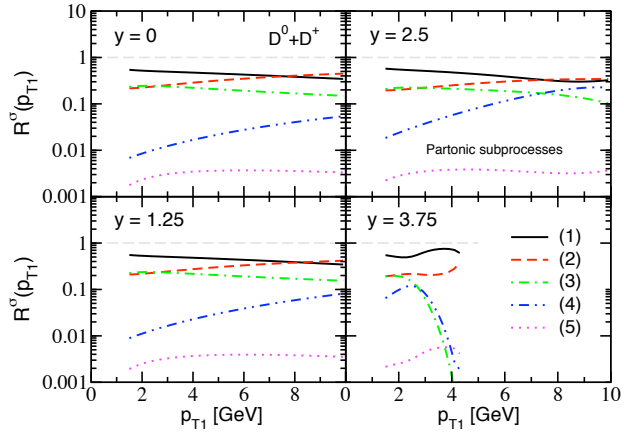

Figure 2.2: Fractional contribution to total $D^0 + D^+$ production in 200 GeV p+p collisions from various charm processes as a function of p_T for different rapidity regions: (1) $cg \to cg$, (2) $cq(\bar{q}) \to cq(\bar{q})$, (3) $gg \to c\bar{c}$, (4) $q\bar{q} \to c\bar{c}$, and (5) $c\bar{c} \to c\bar{c}$. Leading order calculation performed using a K factor of 2 [69]

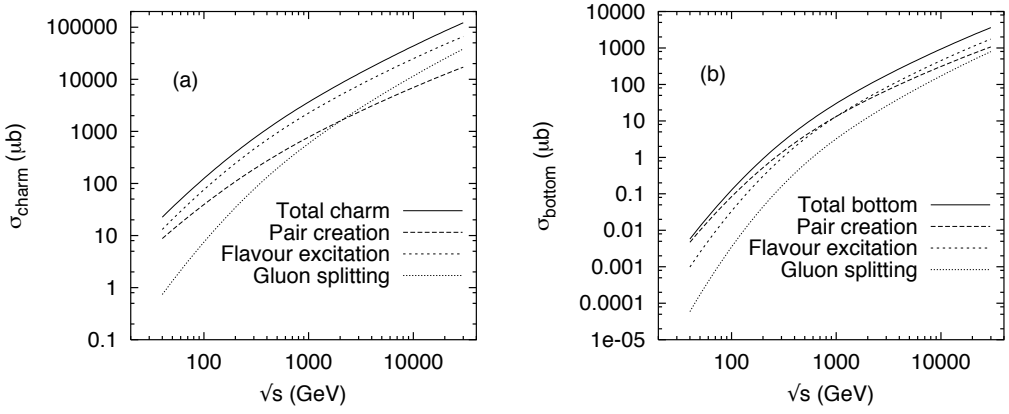

Figure 2.3: Contribution of various production processes to charm and bottom cross sections as a function of beam energy [68].

ization scales. Charm is always treated as a heavy or "inactive" flavor. To evaluate the FONLL cross section, the differential $Ed^3\sigma_Q/dp_Q^3$ is evaluated at fixed order NLO. Then large terms of the order $\alpha_s^n \log^k(p_T/m)$ are resummed with next-to-leading logarithm accuracy. To get the full cross section this must be integrated over the p_T and rapidity distributions, so kinematic inputs are required. Also, charm is treated as an active flavor for $p_T >> m$. Because of this FONLL might be more accurate at the highest p_T ranges, while NLO is perhaps best overall. Calculations have shown the total NLO and FONLL cross sections to be consistent with each other [70].

2.4 Cold Nuclear Matter Effects on Heavy Flavor Production

Heavy quarks have long been regarded as a useful probe of the medium created in a heavy ion collision. Production is thought to be controlled by pQCD, making the expected yield easier to calculate than that of light quarks. Heavy quarks were first thought to lose less energy in the medium than light quarks due to the "dead cone" effect [71]. RHIC results have shown that in fact the energy loss is approximately equal to that of lighter quarks, providing a useful testing ground for energy loss models. The charm quark mass lies in a region that makes it sensitive to many types of effects: it is heavy enough that its mass is governed by a hard scale, but after hadronization the binding

energy of the D meson is of the order a few hundred MeV, which is sensitive to soft physics [69]. The lifetime of a D meson is around 10^{-12} sec, which is much longer than the lifetime of the QGP ($\approx 10^{-23}$ sec) so it is able to transmit information out of the medium. Although closed charm and bottom resonances are affected by many interesting nuclear effects, we will limit our discussion to open charm, which is the topic of this thesis. Open charm is thought to be a cleaner probe of charm production than the J/Ψ because its interactions with the nuclear matter are less complex.

To understand heavy flavor in heavy ion collisions, we must understand the cold nuclear effects in p+Au and d+Au collisions. This is because these effects are impossible to disentangle from the medium interactions that occur during a Au+Au collision. Isolating the cold nuclear matter interactions helps us to understand how initial and final state multiple scattering changes charm and bottom observables. This scattering can either be incoherent, in which case we see p_T broadening, or coherent scattering, involving small transfers in longitudinal momentum p_L which lead to shadowing [69]. Initial state elastic scattering causes the Cronin effect, seen in the data as an enhancement in the open charm spectrum at moderate p_T. Shadowing is expected to have a large effect since it causes the depletion of gluons, and charm production is strongly dependent on the gluon distribution.

One of the biggest surprises of the charm Au+Au results from RHIC is that charm is suppressed by a similar amount to pions. Open charm is also found

to be suppressed at forward rapidity in d+Au collisions at RHIC (see Sec. 2.5). This suppression is larger than what can be explained by shadowing effects alone, and is in a rapidity region smaller than that where CGC effects are expected to be dominant. Theorists are divided over whether the CGC can explain suppression in this kinematic range, or if other mechanicsm are at work. Vitev attributes this suppression to radiative initial energy loss effects of the deuteron passing through the nuclear material [69]. An average parton is found to lose $\approx 10\%$ of its energy while interacting with a gold nucleus. Combining energy loss with higher twist shadowing gives a reasonable match to data at RHIC energies, and is especially effective at high p_T. Another mechanism that might cause charm suppression in Au+Au collisions is the predicted enhancement of charm baryons relative to mesons in the medium [23]. Because charmed baryons such as the Λ_c have a smaller branching ratio to electrons than D mesons, fewer heavy flavor electrons are produced, mimicking suppression. Baryon enhancement is also measured in d+Au collisions, though the effect is not nearly as great as in central Au+Au [72].

While charm in the forward direction is suppressed in d+Au collisions, the overall cross section is higher than expected from pQCD calculations. Some of this is explained by the NLO processes discussed in the last section. Another source of charm in the nucleus has been proposed with the intrinsic charm model (see Ref. [73]). Charm that exists in the nucleus is typically the result of gluon splitting in the initial state and obeys DGLAP evolution.

Intrinsic charm, though, arises from quantum fluctuations that create a state like $|uudQ\bar{Q}>$. One model, known as BHPS, finds charm arising from higher Fock states, creating charm quarks with a higher momentum fraction than can arise from standard evolution equations. Another model, known as the meson cloud model, sees the nucleus fluctuating into a charmed baryon plus charmed meson state. It also predicts a hard spectrum, and a slight asymmetry between charm and anticharm that has not yet been experimentally verified. In order to predict the open charm spectrum in d+Au, a scattering calculation must be performed which involves a diffuse projectile containing charm hitting a dense nucleus of CGC-type matter. Even with nuclear saturation effects included a higher than expected charm yield is predicted.

2.5 Open Heavy Flavor results at RHIC

There are two main ways to detect D and B mesons at RHIC: directly, through the reconstruction of the D via its decay products, or indirectly through the measurement of decay leptons. Both PHENIX and STAR have measured central rapidity single electrons from heavy flavor decays, and PHENIX has made a similar forward single muon measurement as well [74–76]. In each case, the charm cross section calculated from these measurements was higher than FONLL predictions by a factor of 2-4 (see Fig. 2.4). This may indicate the presence of additional sources of charm not well understood by current

theory. The STAR measurements consistently lie about a factor of two above PHENIX measurements for all collisions systems (Fig. 2.5). However this has recently been discovered to be caused by a hidden problem with the STAR measurements involving an underestimate of the backgrounds from its Silicon Vertex Tracker [77]. PHENIX has additionally measured the charm cross section using dileptons, since electrons from heavy quark decays dominate the mass spectrum above 1.1 GeV [78]. The results were found to be consistent with the PHENIX charm cross setion from single electrons.

Single electrons have also been measured in Au+Au collisions [79; 80]. This led to the discovery that charm at high p_T is suppressed at a similar rate to light quarks in hot nuclear matter (Fig. 2.6). These findings showed the dead cone effect to be insignificant, with charm energy loss dominated by both radiative and collisional processes. It is also possible the R_{AA} is artificially lowered by the enhancement of Λ_c in the medium, which has a smaller semileptonic branching ratio than D mesons, potentially skewing the results. The total charm cross section still obeys binary scaling, however, because high p_T events only make up a small fraction of the overall cross section. Electrons were also found to exhibit v_2, showing that the charm quarks participate in collective flow in a comparable way to light quarks.

Even the "direct" detection is not that direct in that the D itself cannot be detected, since this would require a detector extremely close to the vertex (a D^+ only travels about 0.3 mm before decaying). While PHENIX does not

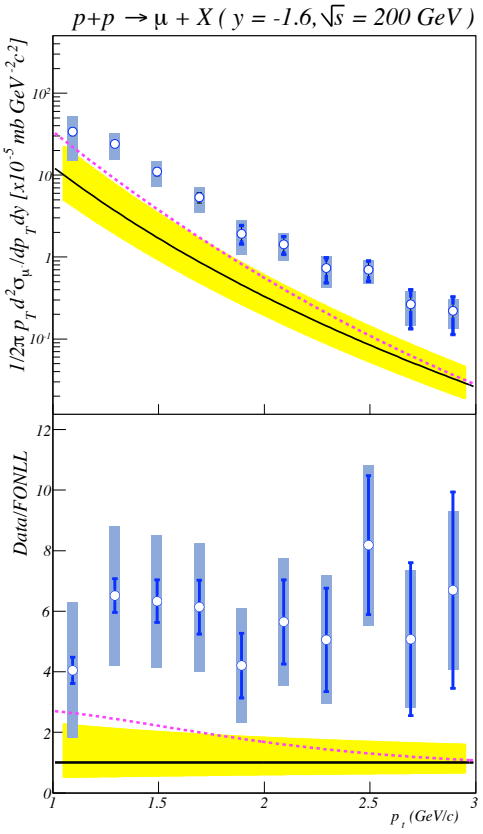

Figure 2.4: PHENIX charm cross section derived from single muon measurement in p+p at forward rapidity. Top shows charm cross section as a function of p_T compared with FONLL predictions; bottom shows the ratio of data to FONLL for each p_T point along with the associated error [75].

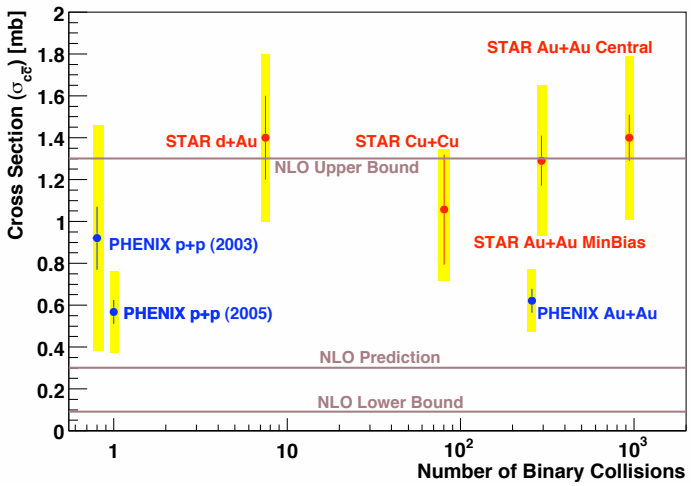

Figure 2.5: Comparison of integrated $c\bar{c}$ cross sections from STAR and PHENIX for a variety of collisions systems as a funcion of the number of binary collisions. These points are compared with NLO charm predictions.

yet have the detectors installed to do this, STAR can, using its Silicon Vertex Tracker. It has reconstructed the decay $D^0 \rightarrow K^-\pi^+$ (and equivalent for $\bar{D^0}$) in d+Au collisions by identifying the invariant mass peak of the D in K$-\pi$ pairs. Again, a higher than expected yield was found, and a resolution to this conflict with NLO predictions remains unclear.

Heavy flavor correlations yield a crucial piece of information missing from the singles measurements, which is the c-to-b ratio. This is very important for interpreting the suppression in heavy ion collisions, because bottom quarks are thought to lose much less energy than charm. If the bottom contribution to the single electron spectrum is less than we have assumed, this could explain the low R_{AA}. The charm to bottom ratio is not calculable with our current

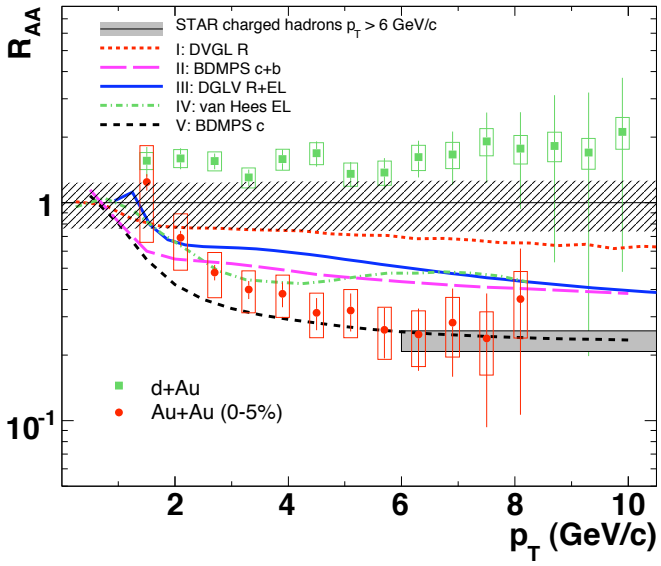

Figure 2.6: R_{AA} as a function of p_T for charm as measured at STAR using single electrons. Results shown both for d+Au as well as central Au+Au collisions, with comparison to theory curves incorporating different energy loss schemes. [80]

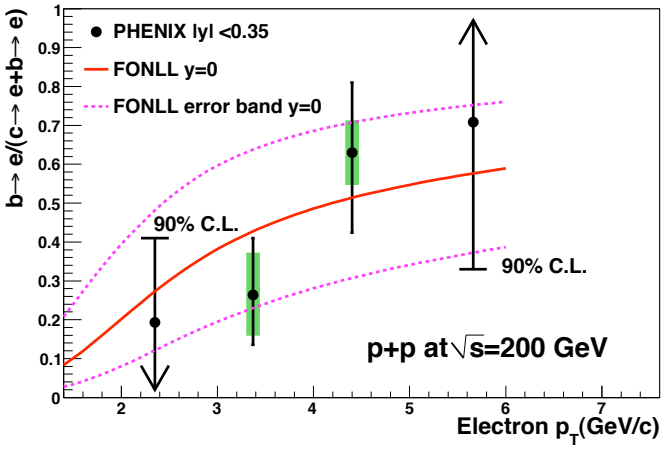

Figure 2.7: Fraction of bottom contribution to electrons in p+p collisions at PHENIX as a function of p_T. [81]

understanding of QCD and must be determined by experiment. PHENIX has done this by measuring electron-kaon invariant mass spectra, which come from either a D or B decay chain [81]. These spectra were compared with Pythia simulations, and the fits were performed to determine the fractions of charm and bottom. A plot of the c-to-b ratio as a function of p_T is shown in Fig. 2.7. STAR found a similar result with electron-kaon azimuthal correlations [82].

2.6 Modeling Charm Correlations with Monte Carlo

Creating a proper Monte Carlo simulation of charm correlations is a bit more difficult than modeling single charm decay products, such as single electrons and muons. There are a variety of fixed order next-to-leading logarithm (FONLL) and next-to-leading order pQCD generators available, but these are generally not set up to handle pairs. In order to simulate electron-muon pairs, the topic of this thesis, we are left with either Pythia (the standard generator) or POWHEG, which creates full NLO heavy flavor events.

2.6.1 Pythia

Pythia is a very good leading-order hadronic interaction event generator that simulates both initial state hard scattering and final state showering. While only leading order terms are used to calculate the hard scattering matrix elements, the simulated fragmentation process includes non-perturbative fragmentation functions as well as a perturbative parton shower in which hard radiation is emitted. It is suited to studying heavy flavor, including measuring cross sections, because pQCD calculations apply to processes involving such massive quarks. The drawback is that it is a leading order generator, with some higher order corrections. Heavy flavor is primarily generated through

gluon fusion, especially when Pythia is set to run charm or bottom exclusively (by turning the factor "MSEL" to 4 or 5 respectively). When run in minimum bias mode, corrections are made to include initial state gluon radiation and final state gluon splitting. While these corrections match the data reasonably well, they do not quite provide NLO accuracy, rather approximating next-to-leading logarithm [83].

On a practical level, there are quite a few Pythia settings that must be altered to get reasonable results. Most importantly the K-factor must be set: this fudge factor is necessary in the absence of a complete NLO description of the event. For the results in this thesis, the K-factor is set to 3.5, in accordance with previous PHENIX heavy flavor analyses [78]. A minimum p_T must also be set, so that cross sections do not become divergent as $p_T \to 0$. We have set a limit of 1.0 GeV/c for this. Finally, Pythia heavy flavor runs fastest when using either the charm or bottom flag, but this only simulates gluon fusion processes. For a more accurate simulation we must run Pythia in minimum bias mode and filter out heavy flavor events, which is very time- and memory-intensive. For a complete list of settings used in running Pythia to produce charm, see Appendix B.

2.6.2 POWHEG

One type of simulator that incorporates all NLO effects is called POWHEG, standing for Positive Weight Hardest Emission Generator. It is not a full event simulator, but rather creates initial hard scattering events that can then be showered by a shower Monte Carlo. In a POWHEG event, the hardest radiation is generated first, using exact NLO matrix elements [84]. The data is written out to a Les Houches format file [85], which allows it to be interfaced to a variety of Monte Carlo generators (Pythia, HERWIG, etc.). It yields similar results to another NLO event generator, MC@NLO, though without requiring the negative event weighting that that generator does. Because of the increased accuracy relative to Pythia, no K-factors or other settings are required.

POWHEG was chosen as an NLO generator for its ability to simulate pairs (something FONLL calculations cannot easily do), and for its ability to be used with Pythia, making a comparison between it and standalone Pythia easier. It helps us make a comparison between the contributions of different charm production processes to the e$-\mu$ spectrum. For the results of the POWHEG analysis, see Sec. 6.3.

2.6.3 Modeling of e-μ Pairs

Both Pythia and POWHEG were used to model the expected signal of electron-muon pairs in p+p collisions. Pythia was run in charm production mode, with the settings described in Appendix B. The K-factor was set to 3.5 as described above. The azimuthal angular correlation of electrons and muons in a kinematic range similar to that measured by PHENIX is seen in Fig. 2.8. Because a clear peak is seen in the $\Delta\phi$ correlation, this is the variable used to study the e$-\mu$ pairs. The peak becomes less significant when we look at the distribution with NLO effects included, using POWHEG (Fig. 2.9). Here POWHEG has been run to produce charm in the initial hard scatterings, and the results have been showered using Pythia. This distribution, though, better matches the data, as will be discussed later.

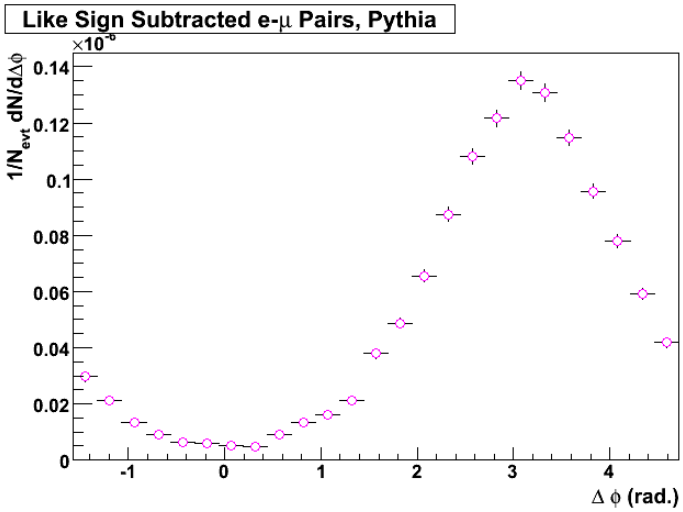

Figure 2.8: Pythia azimuthal angular correlation of e$-\mu$ pairs for muon $p_T > 1.0$, electron $p_T > 0.5$, muons between $1.4 < |\eta| < 2.1$ and electrons between $|\eta| < 0.5$.

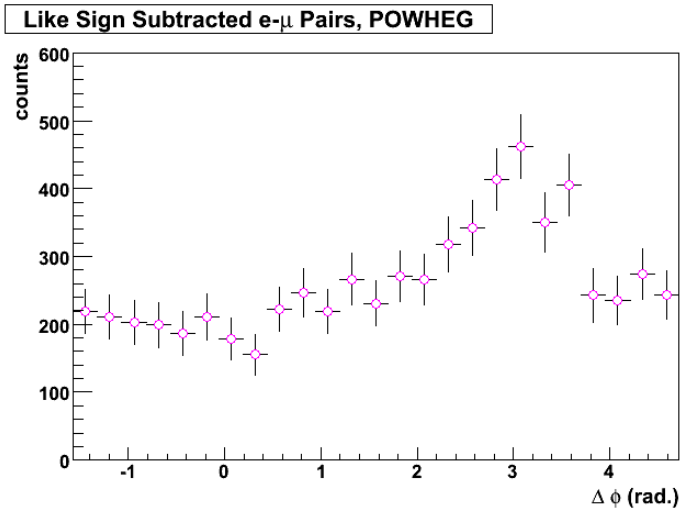

Figure 2.9: POWHEG azimuthal angular correlation of e$-\mu$ pairs for muon $p_T > 1.0$, electron $p_T > 0.5$, muons between $1.4 < |\eta| < 2.1$ and electrons between $|\eta| < 0.5$.

Chapter 3

Experimental Setup

The PHENIX detector is located at Brookhaven National Laboratory in Upton, New York. The lab was established in 1947 and has a long history of important physics discoveries. It is currently home to the Relativistic Heavy Ion Collider (RHIC), at which PHENIX is situated.

3.1 Experimental Facilities

3.1.1 RHIC

RHIC was designed to survey a large portion of the phase diagram of QCD matter, including the detailed study of the quark-gluon plasma and the search for the QCD critical point. A range of proton and heavy ion systems may be collided, including p+p, d+Au, Au+Au, and Cu+Cu, at energies up to 200

GeV. Asymmetric collisions are possible because the two counter-circulating beams travel through independent rings with separate steering magnets. RHIC is also capable of colliding polarized proton beams, enabling the study of nucleon spin structure, at energies of up to 500 GeV. The beams intersect at six different points, and RHIC was designed so that detectors may be stationed at each of these points. Originally experiments were located at four of these crossing points: two large detectors with a wide range of physics goals (STAR and PHENIX) and two others with more specialized ones (PHOBOS and BRAHMS). PHOBOS ended operations in the summer of 2005, and BRAHMS finished a year later. The first data run occured in the summer of 2000, and there has been a run every year since.

Beams are supplied to RHIC from two different sources, depending on whether protons or heavy ions are being collided. Protons are supplied from a 200 MeV linear accelerator (Linac), and are then transferred to the Alternating Gradient Synchrotron (AGS) Booster, where they are accelerated further (see Fig. 3.2). In order to supply heavy ions, the Tanden Van de Graff strips atoms of their electrons using static electricity, and then accelerates the ions. In the case of gold atoms, typically 32 electrons are removed in the Tandem. Ions are then transfered through the Tandem-to-Booster line, where they are further accelerated using magnetic fields to 5% the speed of light. At this point they have been stripped of all but the two most tightly bound electrons. The ions enter the Booster and are accelerated still more. After a beam has left the

Figure 3.1: RHIC and AGS complex as seen from above. Shown is the RHIC accelerator ring, the AGS initial accelerator, and the beam sources (LINAC and Tandem).

Booster it enters the AGS, whose synchrotron completes the acceleration by using 240 alternating gradient magnets until the ions are moving at 99.7% the speed of light. The beam is then sent through a transfer line to RHIC, where the gold ions lose their remaining electrons. A switching magnet directs the beam into either the clockwise-circulating ring or the counterclockwise one. Once a beam is delivered to RHIC it may last several hours, with proton beams lasting longer than gold beams due to smaller inter-beam scattering effects. For a diagram of beam intensities versus time see Fig. 3.3.

In the 2008 run used in this analysis, beams of deuterons were collided with gold ions. The deuterons were obtained from a TiD_2 source. In an asymmetric collision, it is important to make sure the beams have the same energy per nucleon, and therefore the same velocity. [86]. At RHIC up to 112 particle bunches may be injected per ring, and at maximum capacity the time between bunch crossings is 106 ns. A typical beam bunch has a longitudinal spread of about 25 cm. In this analysis we use the data from the 2006 p+p run, and also from the 2008 d+Au run. For Run 6, the integrated luminosity measured by PHENIX was 45 pb^{-1}, the emittance (a measure of beam spread in phase space) was $18 - 23$ μm, and the number of protons per bunch was 135×10^9 (Fig. 3.4). The instantaneous luminosity was 18×10^{30} $\text{cm}^{-2}\text{s}^{-1}$. For Run 8, the luminosity was 38 nb^{-1}, the emittance was $16 - 28$ μm, and the number of ions per bunch was 1.5×10^{11} (Fig. 3.5). The instantaneous luminosity was 13.5×10^{28} $\text{cm}^{-2}\text{s}^{-1}$.

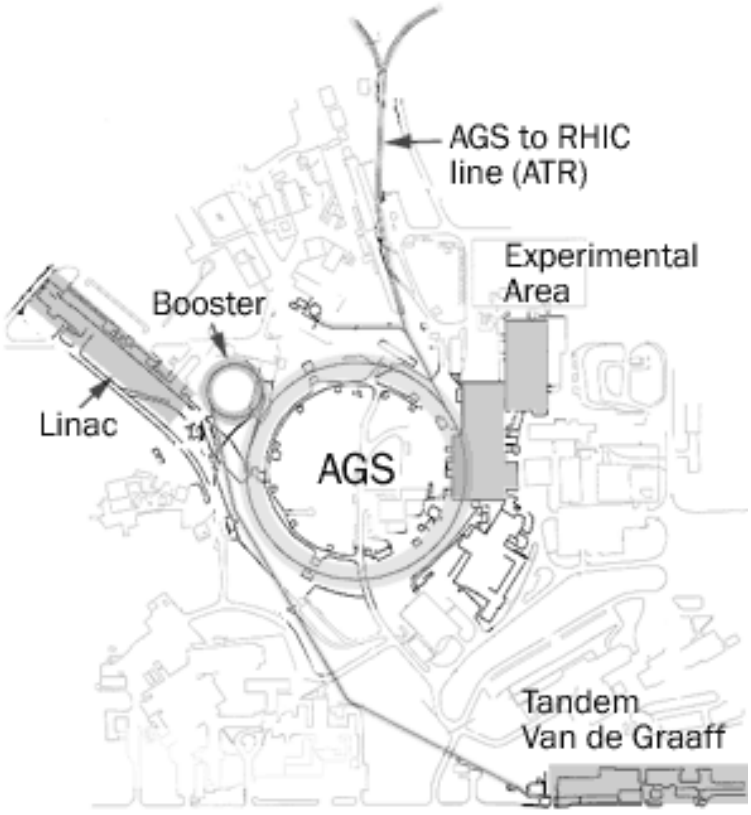

Figure 3.2: Diagram of AGS booster, Linac, and Tandem Van de Graaff used to produce and accelerate beam particles. They are connected to the main RHIC ring via the AGS to RHIC line.

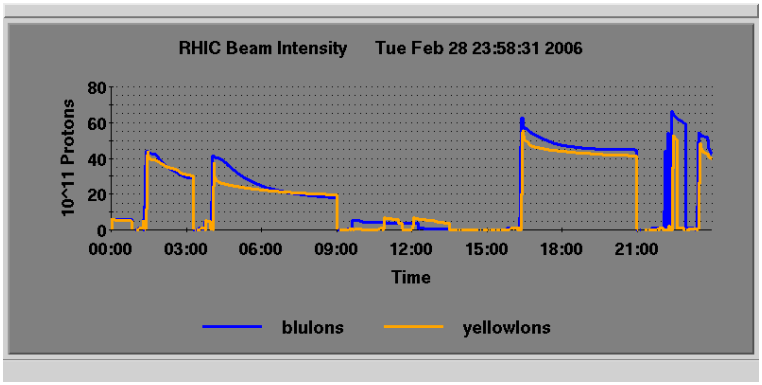

Figure 3.3: Strength of beam vs. time for selected day during RHIC Run 6, showing several typical stores. The two counter-circulating beams are denoted by the yellow and blue lines.

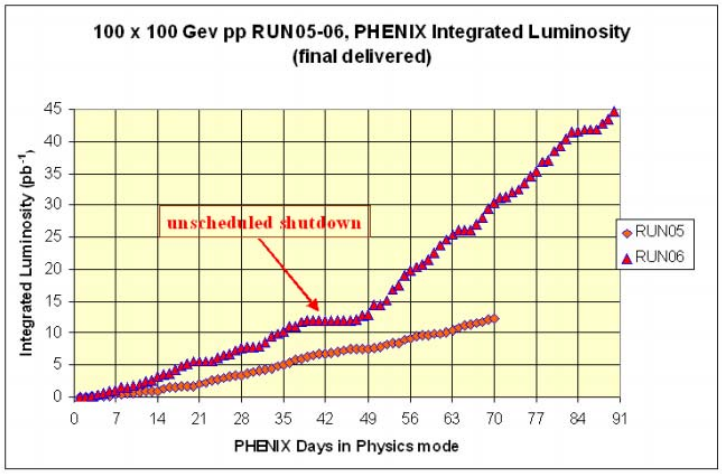

Figure 3.4: Total integrated luminosity for the 2006 RHIC run (Run 6), as compared with the previous year's run.

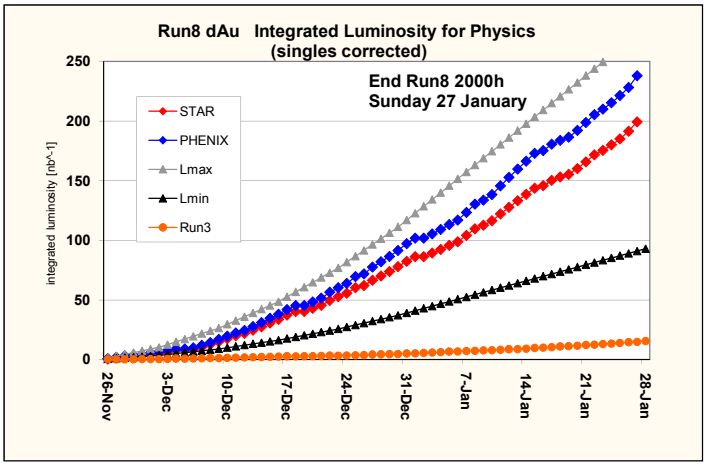

Figure 3.5: Total integrated luminosity for the 2008 RHIC run (Run 8). Comparison shown between PHENIX and STAR, as well as from the previous d+Au run (Run 3).

3.2 PHENIX

PHENIX, also known as the Pioneering High Energy Nuclear Interaction eXperiment, is a 4000 ton detector that was designed to study a wide range of phenomena. The acceptance region covered by the central arms is 180 degrees in azimuthal angle, and between $-0.35 < \eta < 0.35$, while the forward arms have full azimuthal coverage and a range of approximately $1.2 < |\eta| < 2.2$ (see Fig. 3.6). Although azimuthal and rapidity coverage is limited, PHENIX is very good at detecting hard and rare processes thanks to excellent momentum and energy resolution. The central arm detectors are optimized for studying charged tracks: the Drift Chamber (DC) and Pad Chamber (PC) measure the the position and momentum with high accuracy, providing information for

track reconstruction. The Electromagnetic Calorimeter (EMCal) is used to determine the energies of photons and electrons. The Ring Imaging Cerenkov Detector (RICH) is the primary tool to identify electrons; it detects the characteristic Cerenkov light emitted by electrons that are moving at a speed greater than the speed of light in a medium. The RICH has a π/e rejection factor of 1 part in 10^4, which is crucial for separating electrons from the abundance of hadrons produced in a collision. In the forward region the primary detectors are the Muon Tracker (MuTR) and the Muon Identifier (MuID). These detectors were designed to find dimuon resonance peaks, and are also used for single muon and forward hadron analyses. A diagram of the detector configuration for the 2006 run is shown in Fig. 3.7.

Before describing the PHENIX detector subsystems, a note must be made on detector geometry. The z-axis of the detector coordinate system is defined by the beam, and the z-vertex position (or z_{vtx}) is the event position along this axis. Positive values of z correspond to forward rapidity, and negative values of z correspond to backward rapidity (for a discussion of rapidity see Appendix C). The azimuthal angle ϕ is defined in the x-y plane perpendicular to the beam direction.

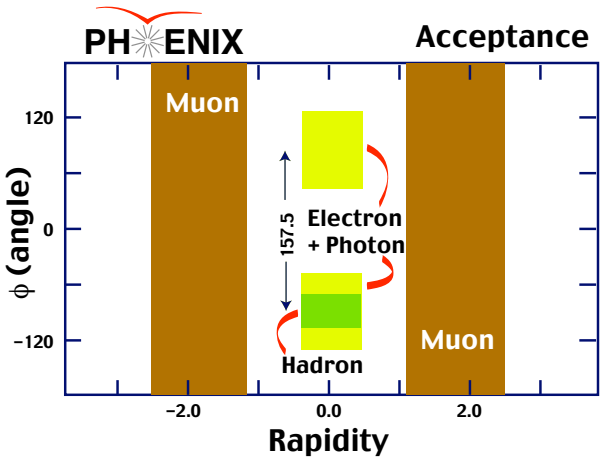

Figure 3.6: PHENIX detector acceptance during the 2006 run. Shown as a function of azimuthal angle (y-axis) vs. rapidity (x-axis). The muon arms cover full azimuthal acceptance in the forward and backward region, while the inner tracking detectors, RICH, and EMCal cover a limited azimuthal region at central rapidity. The green band shows the location of the Time of Flight detector, which is not used in this analysis.

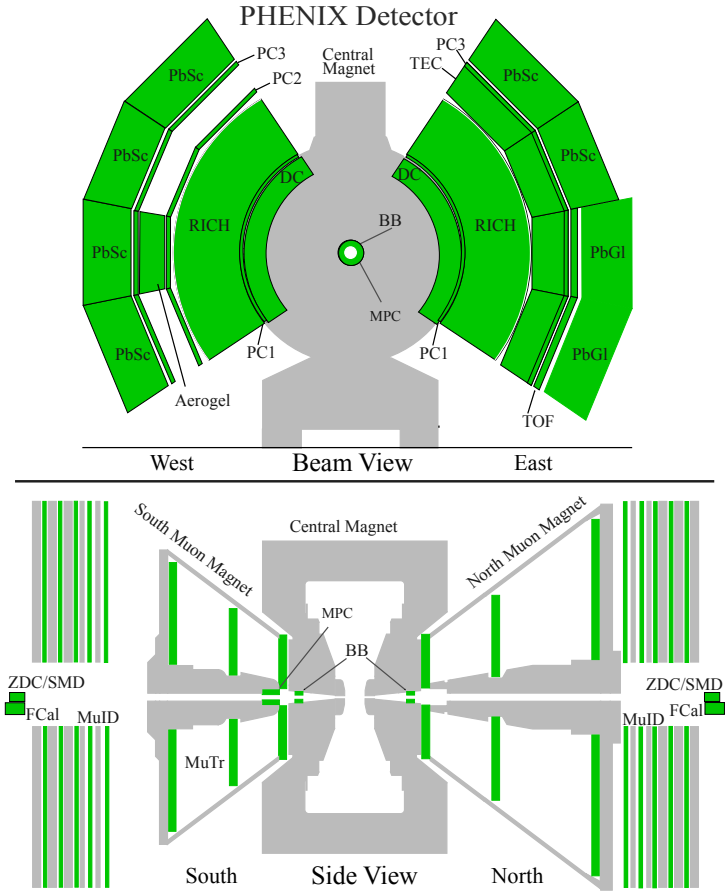

Figure 3.7: PHENIX detector setup for the 2006 p+p run. Steel is shown in grey, and active detectors in green.

3.2.1 Global Detectors

Beam-Beam Counters

The two beam-beam counters (BBCs) sit just outside the poles of the central magnet (at a position along the z axis of ± 144 cm) and in front of the MuTR, at $3.0 < \eta < 3.9$ [87]. Their purpose is to measure the time the collision takes place, to provide input to the Level-1 trigger and also to measure the collision vertex position. Each BBC is composed of 64 hexagonal quartz crystals coupled to 1" diameter photomultiplier tubes. These crystals act as Cerenkov radiators, generating Cerenkov light for particles with a velocity greater than the index of refraction (approximately 1.5). The detectors were designed to be radiation hard, capable of operating correctly in a wide range of event multiplicities, and able to withstand a high magnetic field.

The BBCs work by detecting the Cerenkov light produced by charged particles that hit the detector. The signal is digitized using flash analog to digital converters (ADCs) on each beam crossing. Information on the number of hits in each arm, timing, and vertex position are read out to the Level 1 Trigger, and if an event satisfies the requirements it is classified as a minimum bias event (see Sec. 3.2.4). By measuring the time at which leading particles hit each of the north and the south BBC, the vertex position of the event along the z axis may be reconstructed. For p+p collisions, the BBC has a vertex resolution of ± 2 cm.

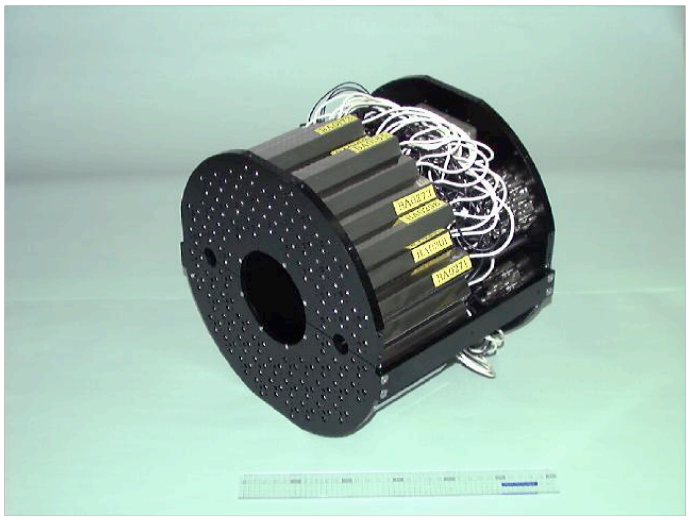

Figure 3.8: Photo of one of the BBC detectors.

Zero Degree Calorimeters

The zero degree calorimeters (ZDC), together with the BBCs, provide centrality information for heavy ion collisions [88]. They are hadron calorimeters located at a z-position of 18 meters from the interaction point. The ZDCs are effectively at zero degrees in rapidity ($\theta \leq 4$ mrad) so that almost all of the energy deposited in them comes from spectator neutrons (see Fig. 3.9). Any charged particles from the collision (such as protons) are bent away from the direction of the ZDCs by dipole magnets. The ZDCs can also be used as a minimum bias trigger and to monitor the luminosity; because these requirements were common to all four RHIC experiments the same ZDC was installed in each one. For this analysis, however, the BBC was the primary detector used as a minimu bias trigger.

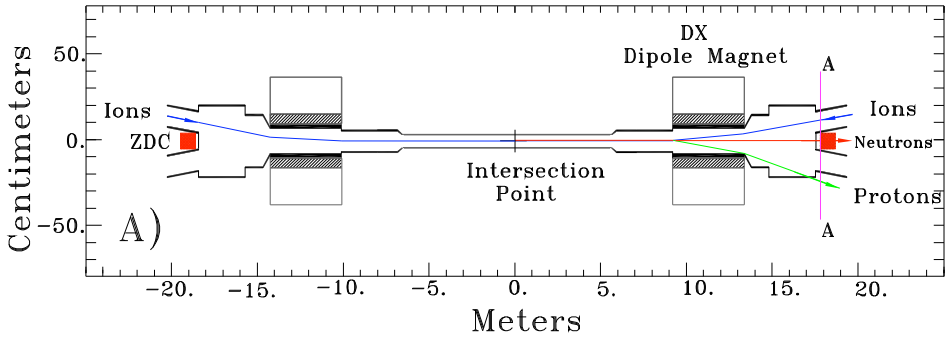

Figure 3.9: ZDC positioning with respect to dipole magnets and interaction region. Position along the z direction shown on the x axis.

3.2.2 Central Detectors

Central Magnets

An axial magnetic field is created through the central interaction region of PHENIX by two pairs of concentric coils inside a steel yolk. This causes charged tracks to bend in the r-ϕ plane. The bend angle can be measured with the Drift Chamber, providing accurate momentum determination. The magnetic coils can either operate in the same direction and add together (the "++" configuration) or go counter to each other (the "+ −" configuration). In ++ mode, the magnetic field reaches a maximum of 9000 Gauss along the beam axis, while in +- mode the field is 0 along the beam and rises to over 3000 Gauss at a distance of 1 m from the beam. At the distance of the DC (2.2 m) all magnetic field configurations drop to effectively 0. This allows for the reconstruction of straight line tracks within the DC. The magnets achieve

a maximum field integral of $\int Bdl = 1.15$ T·m in the ++ or − − (reverse) configuration, which are the configurations used in this analysis.

Drift Chamber

The innermost detector in the PHENIX central arms is the Drift Chamber (DC), which is the detector primarily used for track reconstruction and momentum determination [89]. Drift chamber detectors are filled with gas, which is ionized when a high energy charged particle passes through. Inside the DC there are charged wires, which attract and accelerate ionization electrons, causing them to produce more electrons in a cascade. By calculating the time a charged particle enters the DC (based on the event timing) and the time the charge registers on the anode wires, as well as knowing the electron drift velocity in the gas (about 50 microns/nsec), we may calculate the position at which the initial ionization occurs. This gives us an accurate way to measure track positions. Tracks may be resolved to within 165 μm in the r$-\phi$ plane.

The DC is divided into two segments (along with the rest of the central arms), spanning 90 degrees in ϕ each, 180 cm in z, and covering the radial region between 2.02 and 2.46 meters. The drift chambers are enclosed by a titanium framework, and filled with gas that is a mixture of 50% argon and 50% ethane. Each arm is divided into 20 equal sectors covering 4.5 degrees in ϕ, called "keystones". In each sector there are 6 types of radially stacked wire modules,

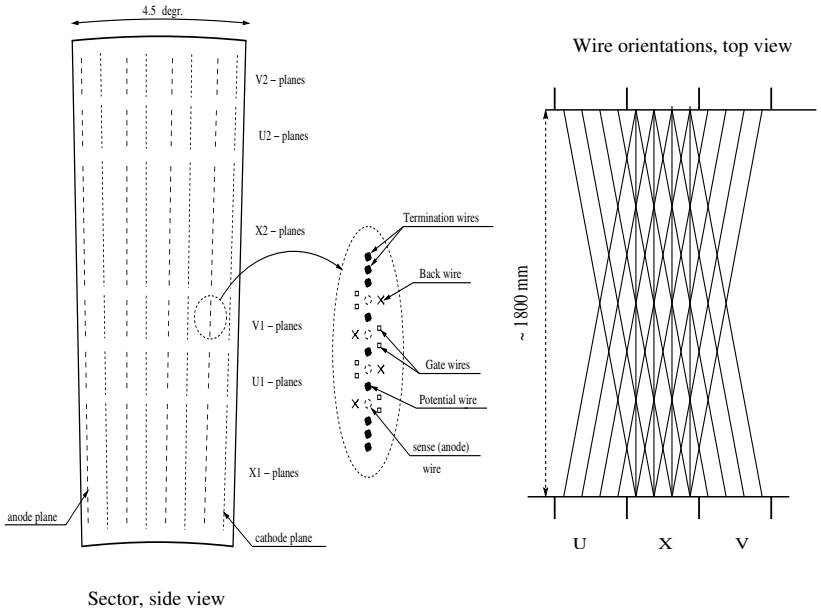

Figure 3.10: Layout of wires in Drift Chamber showing orientation of stereo angles. The drawing on the left shows a single keystone from the side, while the drawing on the left shows the stereo angle of the wires visible from above.

called X1, U1, V1, X2, U2, and V2. The modules contain 4 anode (sense) planes and 4 cathode planes, with a space of length 2-2.5 cm in which electrons may drift between them. Within each plane the X modules contain 12 sense wires, while the U and V modules contain 4. The X module wires run parallel to the beam, while the U and V wire nets are tilted with respect to the X at about a 6 degree angle to provide stereo resolution (see Fig. 3.10). Each sense wire is separated into two halves (corresponding to $z > 0$ and $z < 0$), and the halves are read out independently. This helps to fulfill the requirement of being able to reconstruct 500 tracks in an event. In total the DC has 6500 anode wires, which corresponds to 13,000 readout channels.

A problem that must be dealt with when designing a drift chamber is left-right ambiguity. If there are two tracks which pass within an equal distance of the anode wires, but one is to the left of them while the other is to the right, the timing will be exactly the same. This means it is impossible to determine which of these two positions is the true track location. To resolve this dilemma, blocking wires are placed to one side of each anode wire to prevent tracks from that side from depositing charge on the wire. The position of the blocking wires alternates between to the right and to the left for every other anode wire. For a diagram of this configuration see Fig. 3.11.

Pad Chambers

The Pad Chambers (PC) are multiwire proportional chambers that consist of three separate detectors, the PC1, the PC2, and the PC3 [89], [90]. The first sits directly behind the DC, the second covers only the west arm and is located behind the Ring Imaging Cerenkov detector, and the third lies in front of the Electromagnetic Calorimeter in both the east and west arms (See Figs. 3.7 and 3.12). The PC1 is used in conjunction with the DC to determine the primary track vector as it passes through the inner detectors. It makes a more accurate measurement of the z position of the track than the DC can provide. Combining this with the precise resolution in $r - \phi$ that the DC provides, the track's position in all three dimensions may be measured. The outer pad chambers are used to help match the tracks to hits in the outer detectors, and

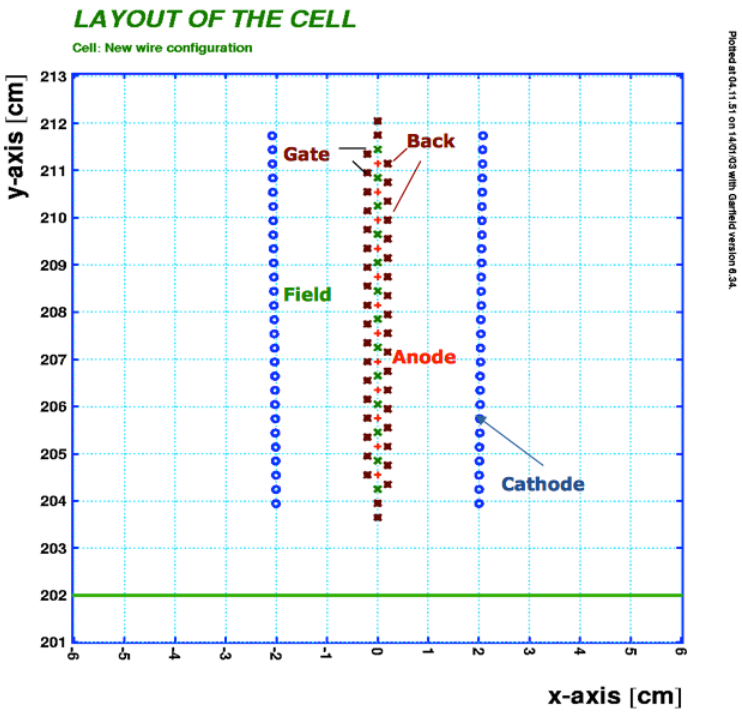

Figure 3.11: Position of the wires in the DC. Cathode wires create the field, while the back wires block electrons drifting from the wrong side in order to resolve the left-right ambiguity. From PHENIX Focus talk, S. Butsyk 2003.

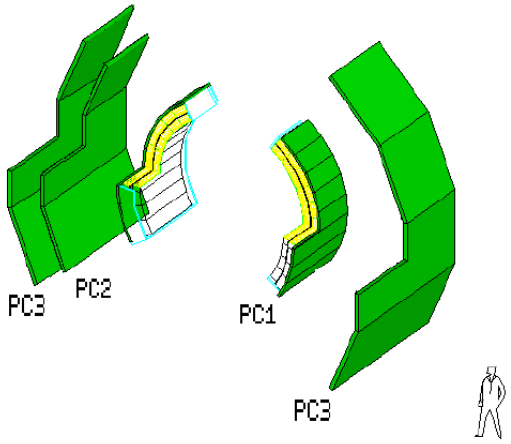

Figure 3.12: Schematic of pad chamber layout, some sections removed for clarity.

determine which tracks in the EMCal are primary as opposed to secondary decays or multiple scattering. It is important to have these detectors because they are the only way to measure track positions at distances between the DC at 2-2.5 m and the EMCal at twice that distance. If the tracks were not followed through this volume they could not be reconstructed with as high an accuracy as they may be currently.

The pad chambers consist of a plane of anode wires surrounded by gas and fitted between two cathode plates, one of which has fine pixel segmentation. The pixel readout cells are very small (8.4×8.4 mm^2) so the position may be resolved very precisely. The readout cells each contain three pixels, and are organized in groups of 3×3 cells called pads to make the readout more efficient. A hit is required to deposit charge on all three pixels in a cell,

greatly suppressing background due to noise. In total the PC has 172,800 readout channels. The PCs were designed in units of cathode panels, and do not require a frame because they support themselves with a stiff honeycomb sandwich structure (thus eliminating some dead regions). The small size of the pixels allows the PCs to have a very high position resolution: ± 1.7 mm in the z direction and ± 2.5 mm in the $r - \phi$ direction.

Track Reconstruction

Tracks are reconstructed using a combinatorial Hough transform [91]. Hits in the DC are mapped in terms of their polar angle ϕ and inclination angle α, which are illustrated in Fig. 3.13. Two angles are required because tracks are expected to bend in the magnetic field, and the bend is proportional to their momentum (therefore α is larger for lower momentum tracks). The angles α and ϕ are calculated for hit pairs that are separated in azimuthal angle by a physically reasonable amount. Hits that are very far from the proto-track are given a low weight (approaching 0) so that noise hits are not included in the fit. The tracking algorithm first looks for tracks that cross both the X1 and X2 regions, and then looks for tracks that only cross either X1 or X2.

The drift chamber alone is able to reconstruct tracks that are entirely perpendicular to the beam direction, but finding tracks that are not in the bend plane requires z information. The DC does not accurately find hit positions

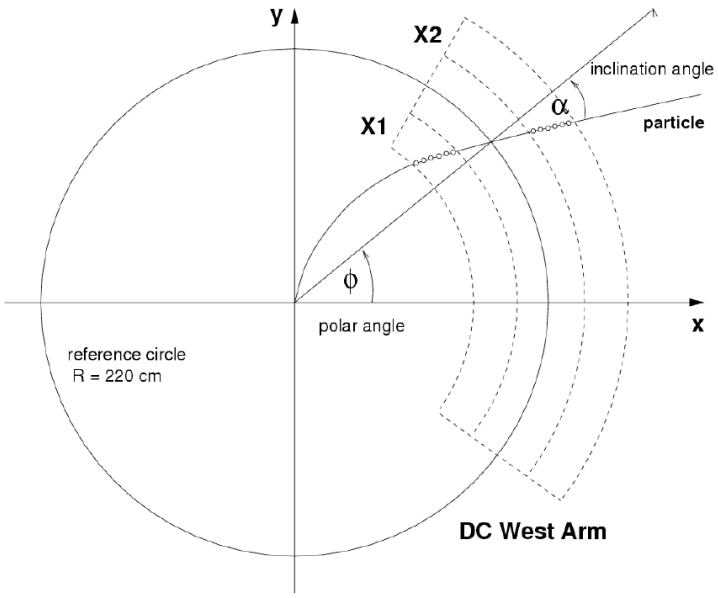

Figure 3.13: Illustration of angles used in Hough transform in the drift chamber, looking along the beam axis. The circles indicate hits along the particle's trajectory.

in z, but the PC1 is capable of resolving z position to a fine resolution, as described above. The track finding algorithm looks for hits near a straight line projection to the PC1. If there is a hit, the track vector outside of the bend plane is defined by the PC1 hit as well as the z vertex position. If there are multiple matching PC1 hits then the hit with the most associated hits from the U and V layers is used. Finally, if there is no corresponding PC1 hit, this vector has to be determined from the stereo wires alone. The momentum resolution of the reconstructed tracks is $\delta p/p \simeq 0.7\% \oplus 1.0\% p/\mathrm{GeV}$ where the first term results from multiple scattering before the DC and the second term comes from the intrinsic angular resolution.

Ring Imaging Cerenkov Detector

A useful way to detect electrons in heavy ion collisions is through the use of Cerenkov light. When a charged particle travels faster than c/n (where n is the index of refraction) in a medium, the surrounding molecules are polarized. They then emit photons in order to return to their ground state. Because the particle is traveling faster than the radiation it emits, a coherent shock front forms. The photons are emitted in a cone surrounding the charged particle, with a half angle given by

$$\cos\theta = \frac{1}{n\beta} \tag{3.1}$$

The number of photons produced per unit path length is equal to

$$\frac{d^2N}{dEdx} = \frac{\alpha z^2}{\hbar c}\sin^2\theta_c \tag{3.2}$$

where α is the fine structure constant, ze is the charge of the particle, and θ_c is the emission angle [30].

The purpose of the Ring Imaging Cerenkov detector (RICH) is to capture Cerenkov light emitted by electrons in a gas enclosure in order to identify them. The light is reflected by spherical mirrors at the back of the detector, where it is focused onto photomultiplier tubes. The RICH provides e/π discrimination below the pion Cerenkov threshold, of about 4.7 GeV/c [92]. The design goal is to limit misidentification of hadrons as electrons to 1 part in 10^4. It is the primary detector used for identifying electrons.

To limit the number of conversion pairs created in front of the EMCal, the total amount of material traversed was limited to 2% of a radiation length. There are two RICH detectors for the east and west arms, each with a volume of 40 m^3, an entrance window 8.9 m^2 and an exit window of 21.6 m^2 in area. The volume is filled with CO_2 (index of refraction = 1.00045), which has a 4.65 GeV/c Cerenkov threshold for pions compared with a 17 MeV/c threshold for electrons. On average 12 photons are produced for a particle with $\beta \approx 1$ that traverses a path length of 1.2 m. The Cernekov light is captured by 48

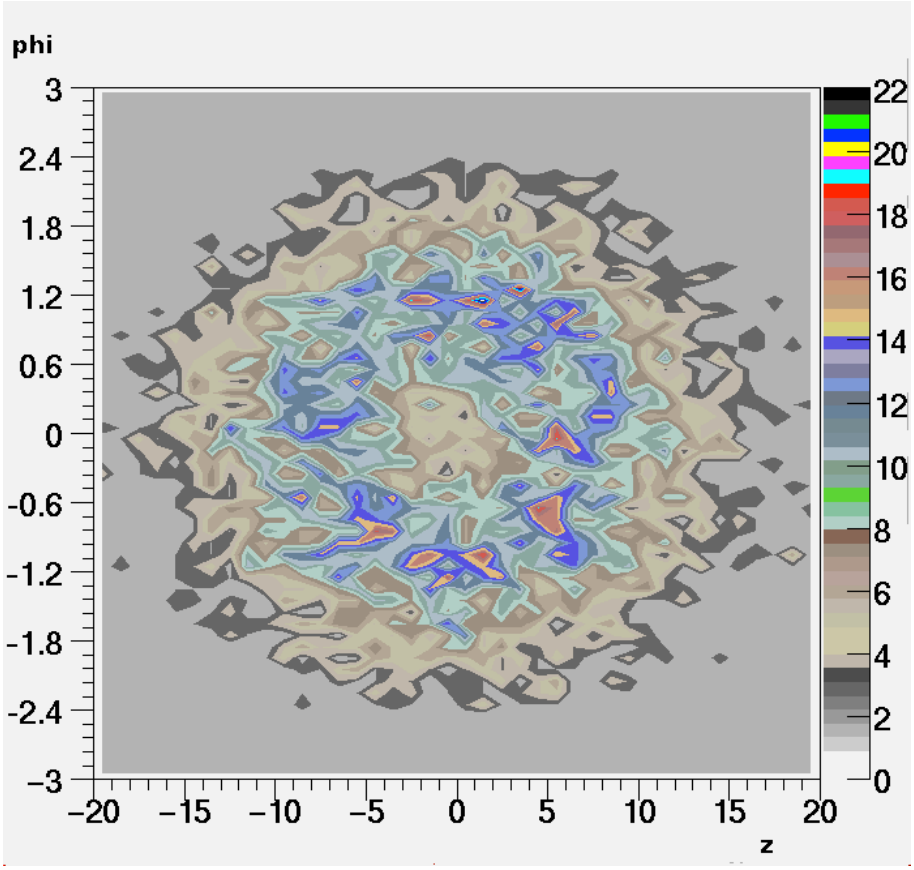

Figure 3.14: Image of a typical electron ring in the RICH. Azimuthal angle is shown on the y axis, z position is shown on the x axis.

composite mirror panels, with a total reflecting area of 20 m^2. The mirrors focus the conical radiation onto a ring where the photomultiplier tubes are located. A ring is identified as belonging to an electron if it is of radius 3.4 cm $< r <$ 8.4 cm. An average ring is of diameter 11.8 cm and consists of 11 photoelectrons, and a picture of a typical ring is shown in Fig. 3.14. The signal from these photoelectrons is then read out to the front end electronics. For a diagram of the RICH see Fig. 3.15.

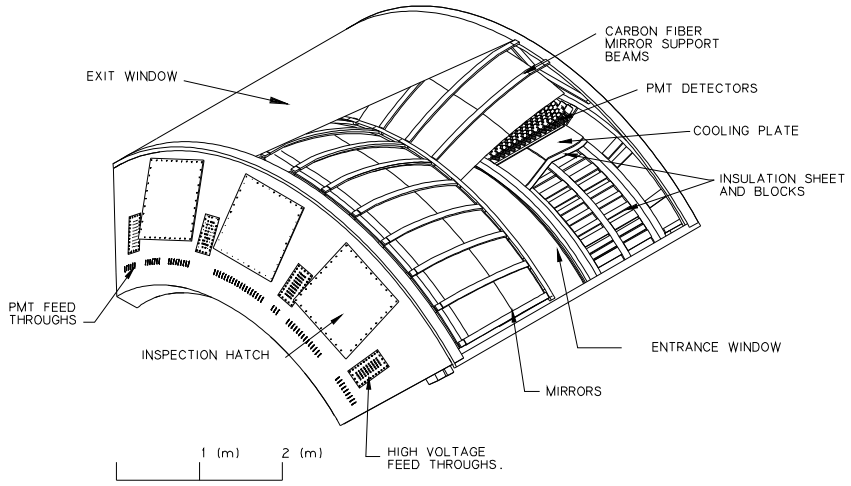

Figure 3.15: Cut-away diagram of the Ring Imaging Cerenkov detector. The plane on which the mirrors are located is farthest from the interaction region.

Electromagnetic Calorimeter

The electromagnetic calorimeter is used for identification of photons and electrons. An electromagnetic calorimeter (EMCal) contains atoms with a high atomic number (in this case, lead) [30]. When an electron passes through the material the high electric field of the electrons surrounding atoms causes the original electron to change direction. The radiation emitted from this acceleration is known as bremsstrahlung radiation. The photon that is radiated is then converted into another electron and a positron. The combination of bremsstrahlung photons and pair production leads to an electromagnetic shower that is detected by the calorimeter. Because muons are so much heavier than electrons they are barely deflected when passing through the lead,

so no photon is emitted and no shower is produced. This is why a separate detector is required for finding muons.

The PHENIX EMCal spans both the east and west arms, 180 degrees in azimuth and between $70^\circ < \theta < 110^\circ$ [93]. It consists of eight sectors, six of which are lead-scintillator calorimeters while the other two are lead-glass Cerenkov calorimeters. These two types of calorimaters use very different technologies, and are each a check on the energy measurements of the other. They also have separate strengths and weaknesses: for example the PbGl calorimeter is better at energy measurements but the PbSc is better at timing.

The PbSc detector is composed of four sectors in the west arm and two in the east arm. It has 48 m^2 of area, and 15,552 towers that are arranged in groups of four to a module. It consists of alternating layers of lead absorber and scintillating plastic, totaling 18 radiation lengths (one radiation length is 18 cm). The scintillator produces photoelectrons when an electromagnetic shower occurs, which, along with the initial electromagnetic radiation, are picked up by phototubes at the back of the towers. The Moliere radius of the shower is 30 mm. The PbSc has a nuclear interaction length of 0.85 cm. Hadrons are not detected because the modules are only one interaction length long: most hadrons do not shower inside the lead, and if they do the shower does not have a chance to amplify to a significant level in such a short distance. Each tower in the PbSc covers 0.011 units in $\Delta\eta$ and 0.008 radians in $\Delta\phi$. The energy resolution is $8.1\%/\sqrt{E} \oplus 2.1\%$. For a diagram of a PbSc module, see Fig. 3.16.

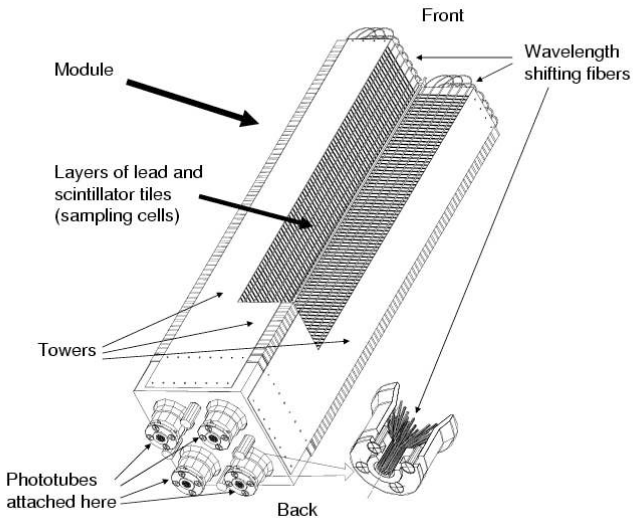

Figure 3.16: Cutaway view of a PbSc module.

The PbGl was not actually built for PHENIX, it was first used in the WA98 experiment at CERN. It consists of 9,216 towers grouped into 192 supermodules, covering two sectors in the east arm. The detectors find Cerenkov light from, and are therefore used to detect, electrons and positrons. The PbGl has a radiation length of 2.8 cm, and the energy resolution is $6\%/\sqrt{E}$. Its Moliere radius is 37 mm. Each tower in the PbGl covers 0.011 units in $\Delta\eta$ and 0.008 radians in $\Delta\phi$. A schematic of a PbGl supermodule is shown in Fig. 3.17.

3.2.3 Muon Spectrometers

The primary detectors in the forward region are the muon arms, consisting of the Muon Tracker (MuTR) and the Muon Identifier (MuID). They were

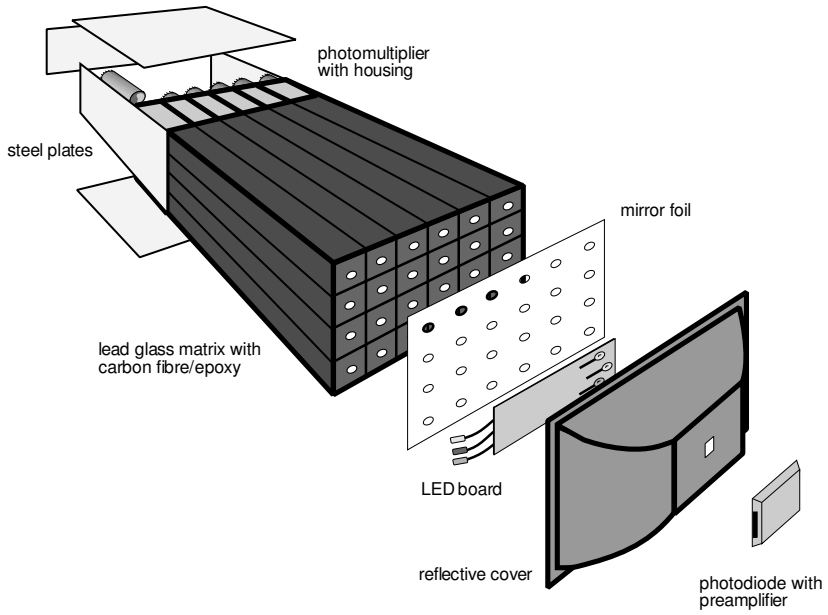

Figure 3.17: Schematic of a PbGl supermodule.

designed primarily to measure J/Ψ, Υ, and vector meson mass peaks using muon pairs [94]. The MuTR provides finely segmented tracking even in a high multiplicity Au+Au collision, and the MuID contains steel absorbers to remove hadrons and identify the muon tracks. The muon detectors are enclosed by the muon magnets, with the central "piston" defining the lower bound on the polar angle acceptance and the "lampshade" defining the upper (see Fig. 3.18). The magnets produce a radial field which has an integral proportional to the polar angle. The magnetic field integral ($\int B \cdot dl$) along a polar angle of 15 degrees is 0.72 T·m for the north arm and 0.75 T·m for the south arm. The minimum polar angle for the north is 10° compared with 12° in the south, giving acceptances of $1.1 < \eta < 2.4$ in the north and $-2.2 < \eta < -1.2$ in the

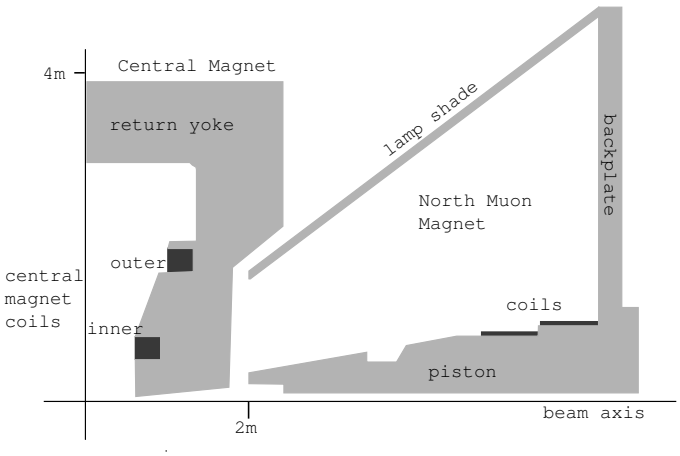

Figure 3.18: Schematic of PHENIX magnet positions showing both the central and muon arms. The magnets are the shaded grey areas.

south. The muon arm backplates also serve as the first absorber layer of the MuID, providing 30 cm of steel in the north and 20 cm of steel in the south. The north MuTR and magnet extends farther in z than that in the south arm, with magnet backplates at positions of 630 cm in comparison to -480 cm.

Muon Tracker

The MuTR was designed to provide a mass resolution of $\sigma(M)/M = 6\%/\sqrt{M}$ for muon pairs, or equivalently a spatial resolution of 100 microns. This is enough to give a significant separation in mass peaks of the ρ/ω from the ϕ and the J/ψ from the ψ'. The tracker gives a momentum resolution of $\sigma_p/p \approx 5\%$ [75]. The detector consists of three stations per arm of tracking

chambers with cathode-strip readout, with each station in the shape of an octant (see Fig. 3.19). The strips are constructed using positive anode wires with negative copper cathode strips, all inside a gas volume (gap). Half of the cathode planes contain strips that run parallel to the anode wires, and half are tilted at stereo angles ranging from 3.75° to 11.25°. The cathode strips were created using photolithography, electro-mechanical etching, and mechanical routing for stations 1, 2, and 3 respectively. There are three gaps per station except in station three, where there are only two (due to budget issues during construction). For each gap, every other cathode strip is read out.

Support for the MuTR comes from a honeycomb panel design for stations 1 and 3. Station 2, though, was required to have a smaller thickness (less than 0.1% of a radiation length) so it is made of thin anode and cathode planes held together by thick aluminum support planes. The gaps are filled with a mixture of 50% Ar, 30% CO_2, and 20% CF_4. The gas is operated under a high voltage of 1850 V, with a gain of 2×10^4.

If a level 1 trigger is fired, all information from MuTR channels is digitized and read out to the PHENIX data collection module (DCM) via the Front End Electronics (FEE). Up to five events can be stored locally before being read out. Because there is not enough space to place the electronics directly on the stations they are read out using 60 cm cables (45 cm in the case of station 1). About 21,000 cathode strips are read out in total.

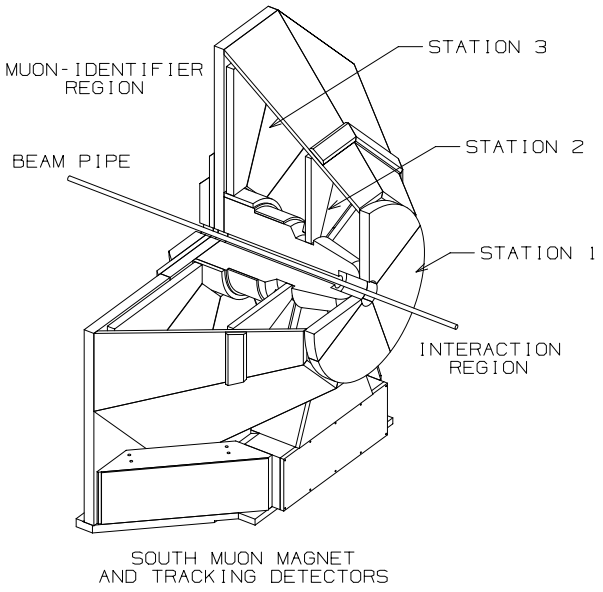

Figure 3.19: Diagram of MuTR south arm. Interaction region to the right, MuID to the left.

Table 3.1: Positions of gaps in MuID in distance from interaction region, as well as depth of absorber layers. The absorber depth refers to the layer that lies in front of the given MuID gap.

Arm	Gap	Near z (cm)	Far z (cm)	Absorber Depth (cm)
North	0	686.96	704.24	30
North	1	728.46	745.74	10
North	2	768.76	786.04	10
North	3	815.86	833.14	20
North	4	861.36	878.64	20
South	0	-686.96	-704.24	20
South	1	-728.46	-745.74	10
South	2	-768.04	-786.04	10
South	3	-815.86	-833.14	20
South	4	-861.36	-878.64	20

Muon Identifier

For every muon that is produced in a collision at PHENIX, 1,000 pions are produced as well. This results in an incredible background to muon detection because it is hard to tell muon tracks from hadron tracks. The only way to separate out hadrons is to stop them in an absorber before measuring the tracks: this ensures that only muons are found because they mostly pass through absorbers without interacting. In the muon arms, the rate at which pions from the vertex are misidentified as muons is set by design to be 2.5×10^{-4}. This ratio is achieved by using 90 cm of steel to absorb hadrons, corresponding to 5.4 hadronic interaction lengths. The steel absorbers consist of the muon magnet backplane, as well as the layers of absorbers that make up the Muon Identifier (MuID). By segmenting the absorber into layers the multiple scattering of muons is reduced.

The MuID consists of five gaps (numbered 0-4) which alternate with steel absorber layers. The first absorber is just the muon magnet backplane, which has a depth of 30 cm for the north arm and 20 cm for the south arm. There are four more absorbers within the MuID of depth 10, 10, 20, and 20 cm from nearest to the vertex to farthest. For a table of the gap positions see Table 3.1. The first two gaps have less steel to make it easier to identify light vector mesons (such as the ω). The 90 cm total steel absorber in the north arm corresponds to about 5.4 hadronic interaction lengths.

The gaps consist of panels of Iarocci tubes, which are planar drift tubes with eight gold-coated CuBe anode wires in the center of a graphite-coated plastic cathode. The inside of the tubes contain a gas mixture of 92% CO_2 and 8% isobutane. These tubes were chosen because they are durable and can affordably cover large areas. In order to read out the tube information two adjacent tubes are OR-ed together to form a "twopack". This is done to increase the efficiency and to decrease the volume of data read out. There are 3170 twopacks per arm. Each gap contains six panels of varying sizes which overlap at the edges to eliminate dead regions (see Fig. 3.20). The panels contain a layer of horizontal and a layer of vertical panels, so both projections can be measured. The size of the gap overall is 13.1 meters high by 10.7 meters wide.

Signals from the twopacks are amplified and sent over a 30 m cable to the Front End Electronics rack. There they are processed by Readout Cards (ROC), where they are digitized. Each ROC takes information from 96 readout channels. Because the MuID is used in the Level 1 trigger (LVL1), the digitized hit information is sent both to LVL1 as well as to the Data Acquisition System. There are a variety of LVL1 muon triggers used at PHENIX, but all depend on hit information as a function of gap position. For more information on the muon triggers used in this analysis see Sec. 3.2.4.

Figure 3.20: Photo of MuID under construction showing the panel structure within a gap. Square hole in middle is the region of avoidance along the beam.

Muon Track Reconstruction

In order to reconstruct particle tracks in the muon arms, tracks are reconstructed separately in the MuID and the MuTR. In the MuID, proto-tracks (referred to as "roads") are initialized using seed hits in the second gap. The roads are then projected forward and backward to match hits in other gaps, and the roads formed in both directions. The projections are straight lines, a valid assumption because there is no magnetic field throughout the MuID. The forward and backward roads are matched to each other by requiring that they differ by fewer than two hits, and contain hits from at least two gaps.

The roads found in the MuID are then used as seeds to reconstruct tracks in the MuTR [95]. First, hits found on different gaps in the same MuTR station

are fit to straight lines: these are called "stubs". The stubs for the last station of the MuTR are first matched to all potential roads that terminate at gap 0 of the MuID. Once these are matched the track is connected to other hits in station 2 and finally station 1 using a Kalman filter algorithm. This takes into account multiple scattering as the track is projected forward into the region with the most potential background. The final track then extends through the MuTR to at least gap 2 in the MuID: any shallower tracks are not kept.

3.2.4 Triggers

PHENIX is not capable of processing and recording the information from every collision event that occurs during a run. The detector must be able to record events in a wide variety of conditions, from high frequency p+p collisions to of order one thousand tracks in central Au+Au collisions. This is why triggers are used to determine which events are worth recording. There are two general types of triggers used at PHENIX, known as Level-1 (LVL1) and Level-2 (LVL2) [96]. The simpler of these are the LVL1 triggers, which are specific to each subsystem and are based on low-level quantities like number of hits and tower energies. The triggers makes a decision on every beam crossing, using the 9.4 MHz RHIC beam clock. LVL2 triggers are based on more complicated algorithms after the LVL1 requirements have been met, and are processed on partially reconstructed events. Because this analysis does not use LVL2 information this will not be described in any more detail.

The LVL1 trigger receives input from each subsystem, and the direct detector input is known as the Local Level-1 (LL1). Algorithms are run on the LL1 input to process the data, which is then output in a reduced form. The Global Level-1 (GL1) trigger takes these as inputs, as well as any busy signals that may have fired, in order to make a decision on the event. The BBC LL1 trigger (BBCLL1) is used as a minimum bias trigger, which is the least selective trigger that can be fired while still ensuring that an event occurred. It is defined to be the coincidence of a hit in both the forward and backward rapidity BBCs.

Even with selective triggers, there may be too much data collected to be read out for all events. PHENIX allows for the option of "scaling" the triggers, meaning only a predetermined fraction of all events will be read out. If a trigger has a "scaledown" factor of n, then only one event will be read out for every $n + 1$ events. An event that is actually read out is said to have fired the "scaled" trigger. An event that satisfies the trigger conditions but is not necessarily read out is said to have fired a "raw" trigger. Finally, a raw triggered event that may or may not be scaled but is read out (not fired during trigger dead time) is a "live" triggered event.

Single Muon LL1 Triggers

The muon arm triggers allow for triggering on single tracks or double tracks, but as the double tracks are used primarily in the analyis of J/Ψ they will not

concern us here. There are actually three types of single muon triggers: Muon 1-Deep (M1D), Muon 1-Shallow (M1S), and Muon 1-Hadron (M1H). The first two triggers were implemented in both Run 6 and Run 8, while the M1H only came into effect during the Run 8 d+Au run. The deep trigger requires a track to pass through the MuID without being absorbed, meaning that the particle is most likely a muon. It requires the deepest hit corresponding to the MuID road occur in gap 3 or gap 4 of the MuID, with three or more hits in total. The hadron trigger requires that the track stops within the MuID volume (the road contains a hit in gap 3 but not in gap 4), excluding most muons. Finally, the shallow trigger requires a hit in one of the first two MuID layers, with two or more hits total. A logic diagram for each of these triggers can be seen in Fig. 3.21. Tracks beginning with hits in the first MuID gap are projected back through the detector, accounting for angular spread due to multiple scattering or a steep incoming angle. An event needs to fire MuID tubes satisfying at least one of the trigger algorithms to issue a LL1 "accept". These triggers are then combined with the BBCLL1 minimum bias trigger, and the GL1 issues either an "accept" or "reject" accordingly. In this analysis, only the M1D trigger is used.

3.2.5 Data Acquisition System

Every PHENIX detector has a system of Front End Electronics (FEE) that takes the direct detector output and turns it into a standardized digital output

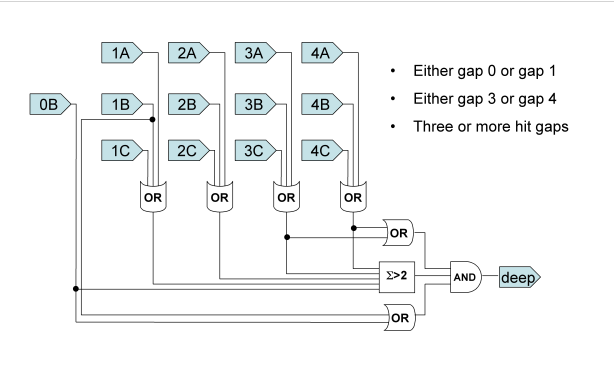

(a) 1-deep trigger

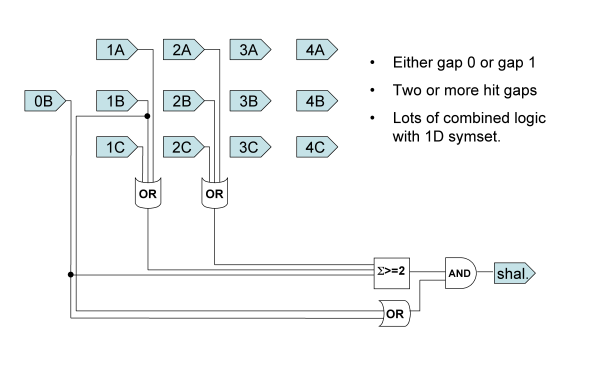

(b) 1-shallow trigger

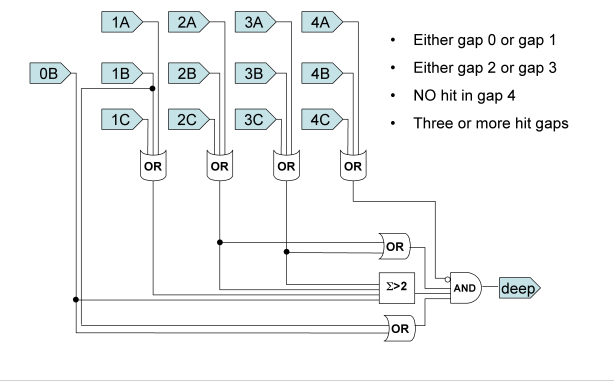

(c) 1-hadron trigger

Figure 3.21: Single muon triggers. The columns correspond to MuID stations, and the rows correspond to logical groups of hits. (from D. Hornback [95]

[96]. The FEEs sit near the detectors in the interaction region; all further processing takes place in the counting room, which is separated from the detectors and the radiation emitted from the collisions. LVL1 trigger information is sent to the FEE with the RHIC beam clock, allowing events to be discarded before they have been fully processed. Because beam crossings occur ever 106 ns, the data must be buffered while awaiting the trigger decision: the LVL1 trigger rate can reach 25 KHz, sufficiently slower than the RHIC clock at 9.4 MHz. The buffering can last for up to 40 beam crossings, with a deadtime of about 5% at full luminosity.

If events pass the triggers they are digitized and sent over fiber optic cables to the Data Collection Modules (DCMs) in the counting room. At this point data has been reduced to a standard packet format, so information from all detectors can be combined and checked for errors and zero-suppressed. The next stage in the process is the Event Builder, which finishes the job of assembling the events. The Event Builder is made up of Sub Event Buffers (SEBs) and Assembly Trigger Processors (ATPs), and can handle data rates up to 60 MByte/s (a single minbias Au+Au collision may contain 160 kBytes). The SEBs pull the data from the DCMs and buffer it in order to be processed by the ATPs. This is where the LVL-2 trigger algorithms are run. Finally the data is ready to be read to disk, and it is sent to one of four "buffer boxes" which can store large quantities of data. When the buffer boxes are full, the data is sent to the High Performance Storage System (HPSS) tape archive,

and it is then ready for analysis.

Chapter 4

Electron-Muon Event and Track Selection in p+p and d+Au

4.1 Analysis Overview

This analysis is the first study of correlated, opposite sign electron-muon pairs from heavy flavor decay done at RHIC. We look at azimuthal correlations because the signal is easily identified from the peak at $\Delta\phi = \pi$. This peak is due to momentum conservation from the produced back-to-back $c\bar{c}$ pairs, and it gives a clear indication that the electron and muon result from a charm pair. The angular correlation also allows us to probe the jet properties of the charm pairs. Single electrons and muons have been measured in various collision systems, but this analysis is the first to study double semi-leptonic heavy flavor decay. A diagram of the decay is shown in Fig. 4.1. Semi-leptonic decay is the

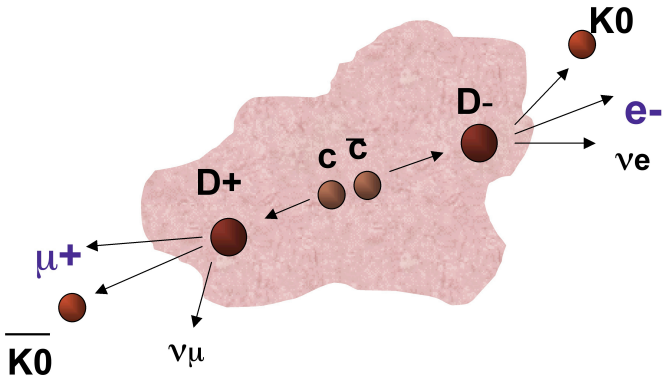

Figure 4.1: Cartoon of process by which opposite sign e$-\mu$ pairs are created.

primary means by which heavy flavor is measured at PHENIX, at least until the silicon vertex detector upgrades make it possible to find D meson decay vertices. This is because PHENIX is very good at measuring single leptons, but due to restrictions on particle identification it is more difficult to reconstruct $D \rightarrow K\pi$ channels. A complementary analysis of electron-hadron pairs from heavy flavor in p+p and Au+Au has also been performed. This measurement studied the charm jet shape in heavy ion collisions, but is subject to higher backgrounds due to the inability to isolate heavy flavor hadrons. Because of this it is difficult to get a clean signal in the high multiplicity environment of Au+Au collisions [97].

The electron-muon analysis has the advantage over similar analyses in that the signal is very clean. Single leptons have large backgrounds from two sources:

photonic electrons, resulting from photon conversions as well as π^0 and η Dalitz decays, and hadronic sources, which are primarily light meson decays. Because these sources do not produce correlated, opposite sign e-μ pairs, they do not affect the signal. Any leptons produced from these sources are equally likely to form opposite-sign e$-\mu$ pairs as they are to form like-sign pairs, so a like-sign subtraction removes these backgrounds. There are many sources of lepton pairs including thermal leptons, resonance decays, and Drell Yan production, but these produce pairs of the same species such as e^+e^- or $\mu^+\mu^-$. This leaves us with a clean, if rare, process.

Because the azimuthal distribution of e-μ pairs reflects the distribution of charm produced in the collision, an extra dimension of information is yielded above what single leptons can give us (charm is by far the dominant contributor to e-μ pairs at the p_T range we study here). The width of the distribution can tell us to what extent NLO effects contribute to the production of e-μ pairs, in comparison to LO gluon fusion. Also the shapes of the opposite and like sign distributions are different for charm and bottom production, so it should be possible to use these to extract the ratio of charm to bottom (though that is beyond the scope of this analysis). Changes in the angular width between p+p and d+Au collisions might indicate cold nuclear matter effects on charm. Nuclear effects will also be evident as a suppression of the total e-μ yield in d+Au as well.

While theoretically there is very little background to the e-μ measurement,

in practice potential backgrounds still need to be evaluated to make sure detector effects do not give unexpected results. This is especially important for the PHENIX muon detectors: because they were optimized for J/Ψ measurments rather than single muons, the absorber is not maximally thick. As a result about 1 in 250 hadrons "punch-through" the steel and are misidentified as muons (see Sec. 3.2.3). Muons are also produced via light meson decay (primarily from pions and kaons), and are not distringuishable from prompt muons on an event-by-event basis. If the hadrons that either punch through or decay result from D decay themselves, they might have a correlation with electrons detected in the central arms. For this reason both of these backgrounds had to be estimated. Furthermore, the background due to photonic electrons was evaluated as a test of the method. Photonic electrons are those that result from the Dalitz decay of light mesons, or from photon conversions in the detetor material. The results of these tests of the backgrounds, and the final spectra for p+p and d+Au, are found later in this section.

4.2 Run and Event Selection

The analysis performed for this thesis uses 200 GeV proton-proton data from RHIC Run 6 and 200 GeV deuteron-gold data from Run 8. The data was taken using the PHENIX detector. The dataset used in this thesis was obtained using the MUID LL1 deep muon triggers, described in Section 3.2.4.

A QA analysis was performed to remove runs with poor data quality. The criteria we use to cut out bad runs includes: runs with no magnetic field, runs lasting less than eight minutes, too many bad high voltage channels, and too many dead front end electronics modules [98]. Also, importantly, the rate of muons and electrons per minimum bias event must be checked. The rate changes both because of detector malfunctions, as well as changes in the arrangement of detectors and absorber material. For example, during each year-long run there are several converter runs, where extra material is added to the interaction region to help determine the photonic background to electron measurements. This creates many more electrons per event, and because of the high background these runs must be removed from the run list. Also for the last few runs in Run 6 the Hadron Blind Detector was installed, which again created many more conversion electrons. These runs were removed as well. For examples of the rates requirements see Figs. 4.2 and 4.3. Runs with anomalously high or low rates were removed from the good run list.

Because the north and south muon arms are physically separated and have different electronics, an independent QA analysis had to be performed for each arm. This leads to good run lists that differ slightly by arm. The total number of minimum bias events used in this analysis after the QA cuts is shown in Table 4.1. Only events with a vertex between -25 and 25 cm in z_{vtx} are used in this analysis, to make sure the collision is not affected by any detector components that might be in the way. The vertex distributions for

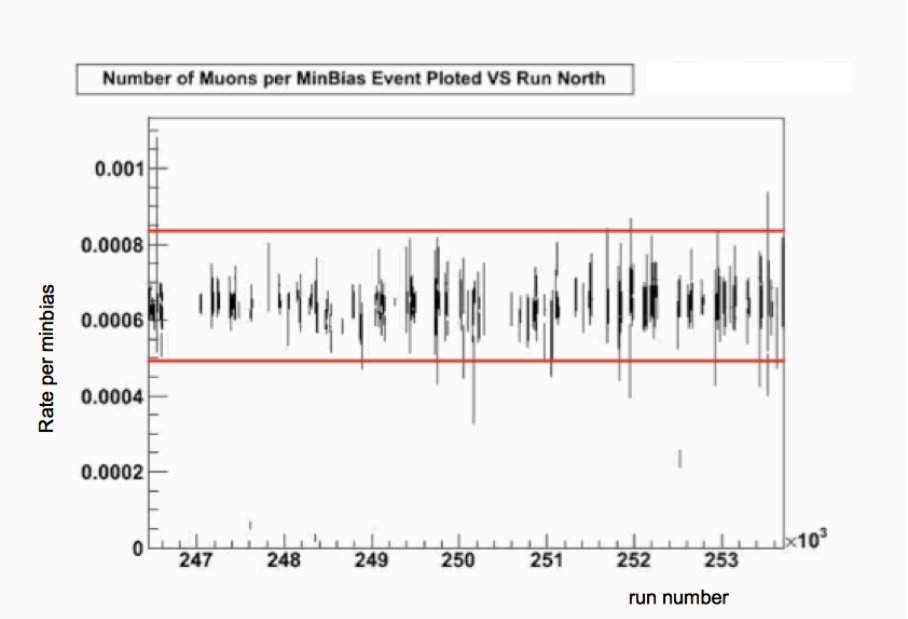

Figure 4.2: Number of muons per minimum bias event vs. run number , Run 8, north arm. Runs with a rate of greater than 0.00085 or less than 0.00045 were removed.

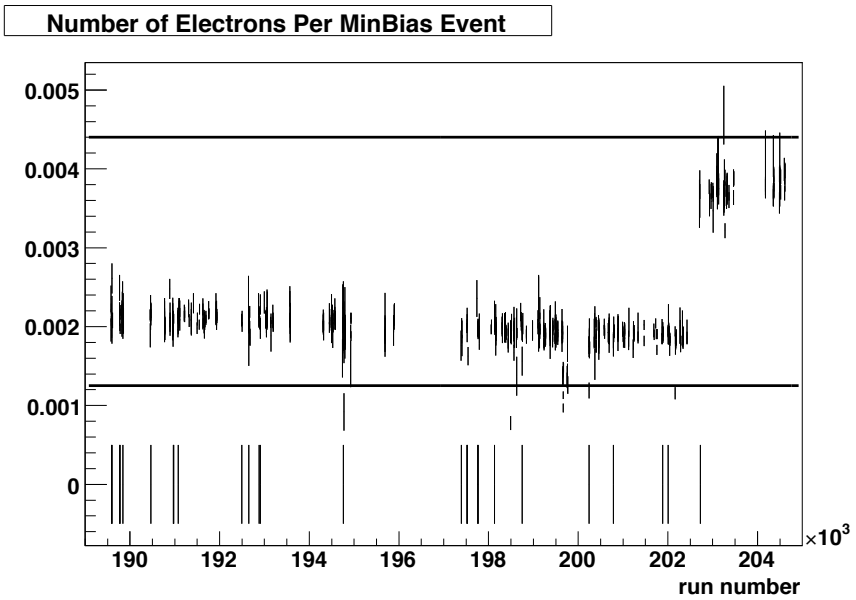

Figure 4.3: Number of electrons per minimum bias event vs. run number, Run 6. Runs with rates above and below the horizontal lines were removed. The spike in rate at later runs is due to the installation of the hadron blind detector.

Table 4.1: Number of minimum bias events sampled in analysis by run and arm.

Run	Minimum Bias events north	Minimum Bias events south
Run 6 pp	5.984×10^{10}	6.008×10^{10}
Run 8 dAu	3.934×10^{10}	1.378×10^{10}

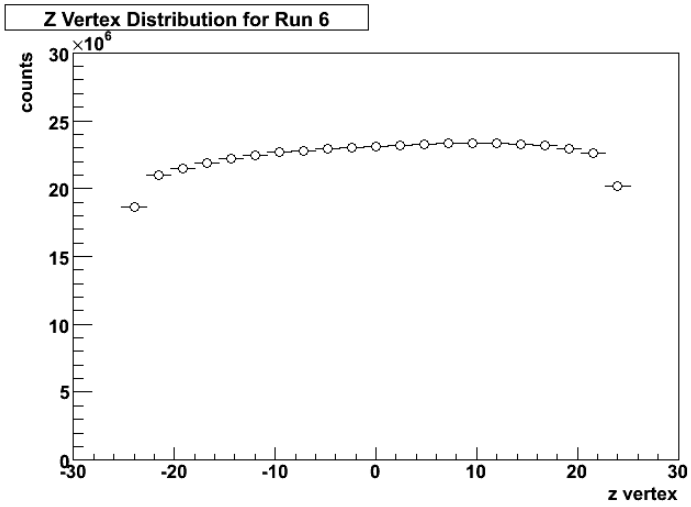

Figure 4.4: z_{vtx} distribution for minimum bias sampled events from the Run 6 p+p dataset.

Run 6 and for Run 8 are shown in Figs. 4.4, 4.5.

4.3 Track Selection and Analysis Cuts

Track reconstruction is done by the PHENIX offline code, which reconstructs tracks from raw data (described in Chapter 3). From the reconstructed tracks, we make analysis cuts to determine which tracks are most likely to be electrons

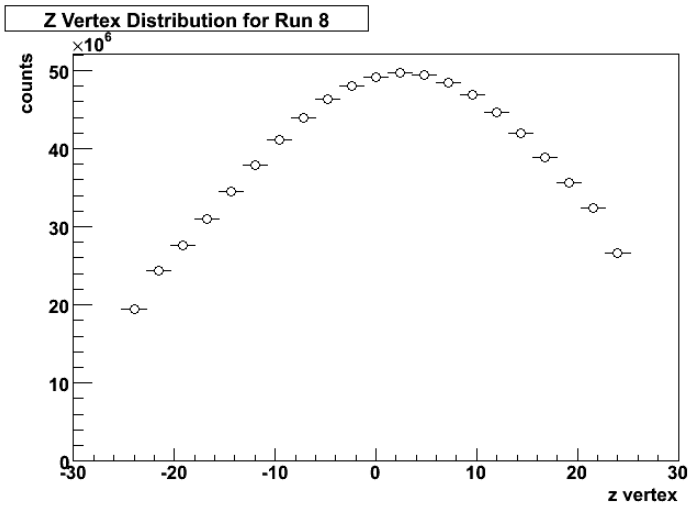

Figure 4.5: z_{vtx} distribution for minimum bias sampled events from the Run 8 d+Au dataset.

or muon. Cuts on muons remove fake tracks, muons that have multiply scattered in the detector and drastically changed direction, or hadrons. Similarly, electron track cuts separate electrons from the many hadrons and photons that are also detected in the central arms. First the track requirements for muons will be described, then we will move on to electrons.

4.3.1 Muon Track Requirements

Definitions

In order to understand the muon cuts, some definitions must be given.

- **Number of MuTR hits**: The MuTR consists of three stations, con-

taining eight layers total (three each in the first two stations and two in the last). A track can create up to two hits per layer, for a maximum of 16 hits.

- **DG0**: stands for "Distance at Gap 0." Tracks in the MuTR are projected back to MuID gap 0 so that they can be matched up with roads in the MuID, forming a complete track. DG0 is the linear offset distance between the road and the track, measured in centimeters.

- **DDG0**: similar to DG0, but it is the angular displacement between the road and the track, measured in degrees.

- **Reference Radius (RefRad)**: this is a projection of the MuID road back to $z = 0$. It is found from the positions and slopes of the track at MuID gap 0. If the RefRad is too large, the track most likely did not come from the collision region, and it must be discarded.

- **Road Slope**: the slope of the MuID road found at gap 0. The slope must not be too low or the track will enter a region of no acceptance at large η in the MuID.

- $p\delta\theta$: this variable measures the extent of multiple scattering caused by the steel absorbers before the track reaches Station 1 in the MuID. It is defined as,

$$P\delta\theta_{sta1} = Pcos^{-1}(\frac{\vec{P_{sta1}} \cdot \vec{R_{sta1}}}{P_{sta1} \cdot R_{sta1}}) \tag{4.1}$$

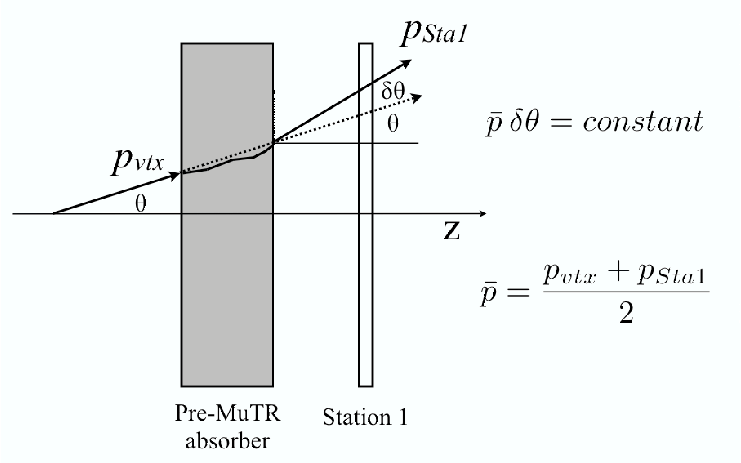

Figure 4.6: Diagram of deflection measured by the quantity $p\delta\theta$ [75].

Where R_{sta1} is the position vector and P_{sta1} is the momentum vector of the track at MuTR Station 1. The position vector has its origin at the z_{vtx} of the event, not at $z = 0$. Also $\vec{P} = \frac{P_{vtx}+P_{sta1}}{2}$, an average of the momentum at station 1 and the momentum of the track extrapolated back to the vertex [95]. The angular deflection is multiplied by the momentum to compensate for the fact that a smaller deflection naturally occurs with larger momentum (see Fig. 4.6). This allows a cut that is the same for all momentum regimes.

The representative distributions of cut variables from the Run 6 dataset are shown in Figs. 4.7 and 4.8.

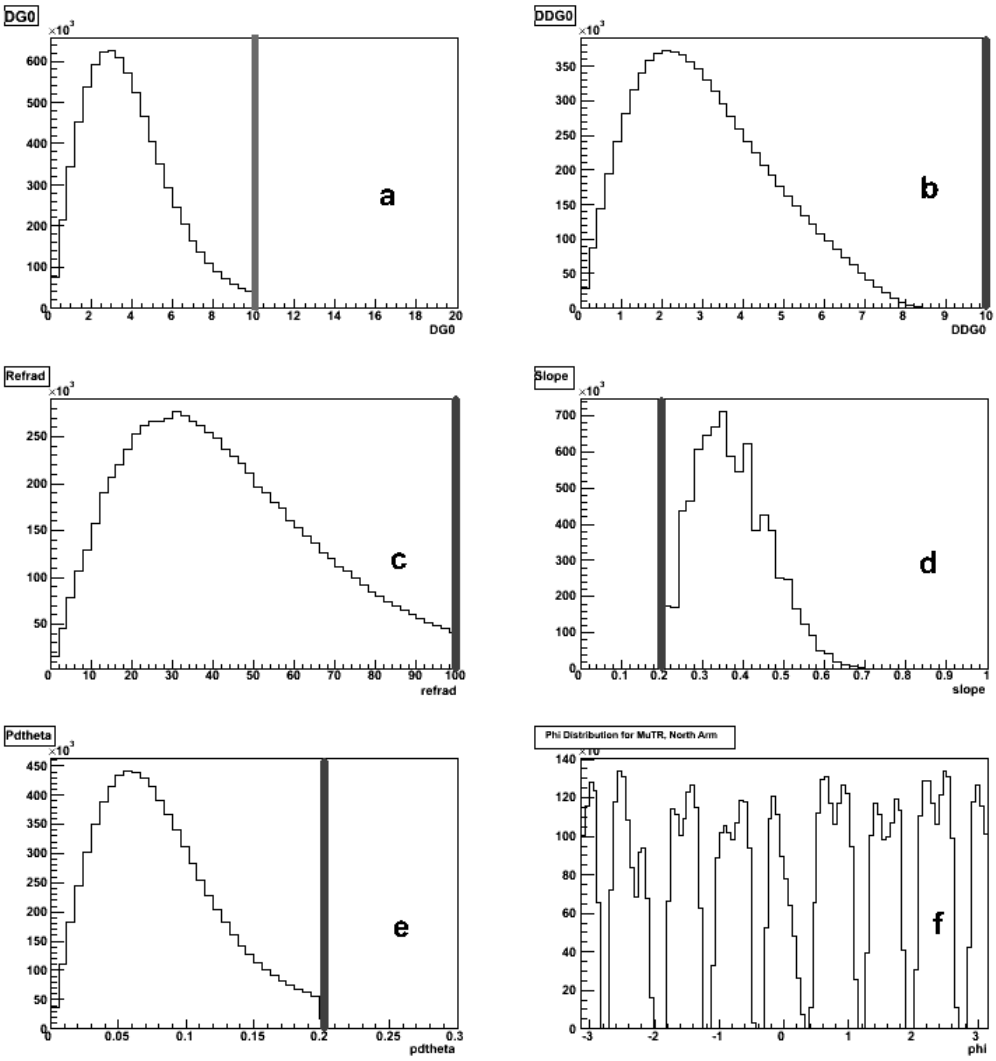

Figure 4.7: Muon variables for Run 6 north arm: (a) DG0 (b) DDG0 (c) Refrad (d) Slope (e) $p\delta\theta$ (f) ϕ at MuTR. Lines show location of cuts.

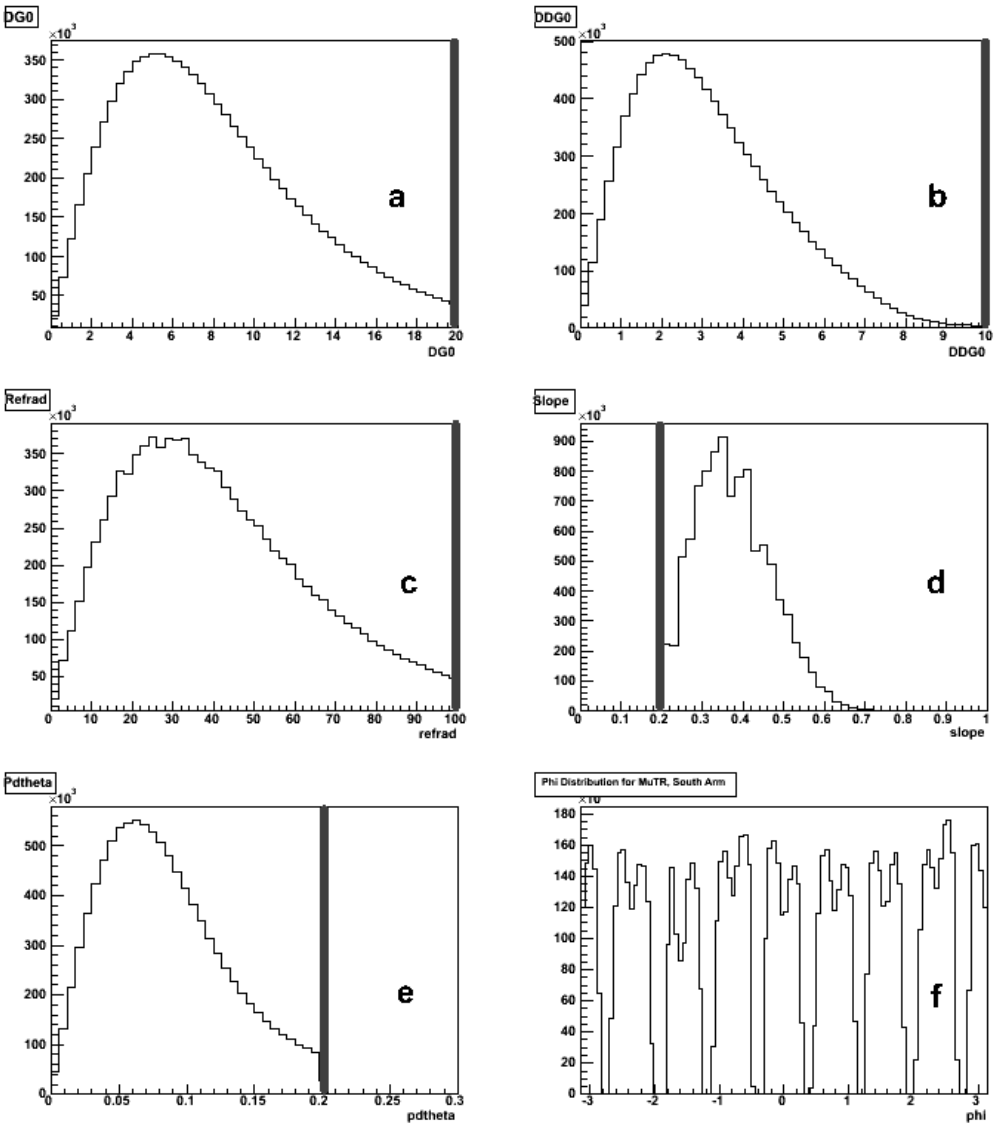

Figure 4.8: Muon variables for Run 6 south arm: (a) DG0 (b) DDG0 (c) Refrad (d) Slope (e) $p\delta\theta$ (f) ϕ at MuTR. Lines show location of cuts.

Muon Cuts

A restricted acceptance range was used for the muon arms, $1.4 < |\eta| < 2.1$. This was chosen to help minimize the effect of vertex position on the muon acceptance, and to reduce beam related effects at higher rapidities [75]. Fiducial cuts were required to remove dead regions in the MuTR. These are graphical cuts, made using the TCutG function of the plotting program ROOT. The cuts are applied station by station for both MuTR arms (Fig. 4.9, 4.10). Also, p_T was required to be greater than 1.0 GeV/c, because the muon arms have a very low acceptance at momentum lower than this. A number of additional cuts were used:

- Track reaches gap 4 (the last gap) in the MuID.
- Number of MuTR hits is greater than or equal to 12.
- Slope > 0.2
- RefRad < 100 cm
- DG0 < 10 cm (north arm), DG0 < 20 cm (south arm)
- DDG0 < 10 degrees
- $p\delta\theta < 0.2$

Because the several of the muon variables measure similar properties of the tracks (slope and vertical offset) it is not obvious that these are all independent

Table 4.2: Muon variable correlations, Run 6 North

Variable	$\mathcal{C}$
DDG0 and DG0	0.154
slope and DG0	0.111
refrad and DG0	0.189
$p\delta\theta$ and DG0	0.022
slope and DDG0	0.123
refrad and DDG0	0.953
$p\delta\theta$ and DDG0	0.013
refrad and slope	0.213
$p\delta\theta$ and slope	-0.003
$p\delta\theta$ and refrad	0.015

quantities. The correlation between any two variables is given by $\mathcal{C} = \frac{cov}{\sigma_1\sigma_2}$ where cov is the covariance and the σs are the standard deviations of each variable. The covariance is defined as $cov(x,y) =< xy > - < x >< y >$. A representative table of $\mathcal{C}$ is shown in Tab. 4.2. For the correlated pairs, special care has to be taken to find the systematic errors, as will be described later. Most variable pairs have a low degree of correlation except for RefRad and DDG0.

After all cuts were applied, a total of 9.27×10^6 muons in the north arm and 1.16×10^7 muons in the south arm are found in Run 6. For Run 8, 4.53×10^7 muons are found in the north arm. The kinematic distributions of muons passing all of the applied cuts as a function of rapidity vs. p_T is shown in Figs. 4.11 and 4.12.

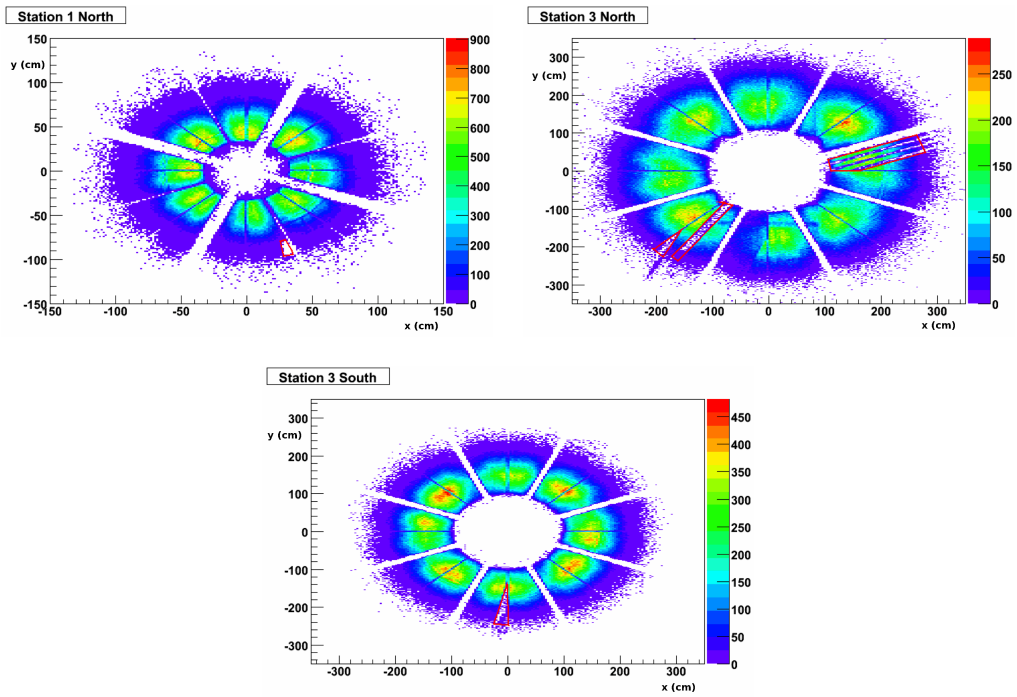

Figure 4.9: Graphical fiducial cuts on MuTR for Run 6. Plots are of y position (y axis) vs. x position (x axis) in cm. Cuts are shown as red lines. Top left, north station 1. Top right, north station 3. Bottom, south station 3.

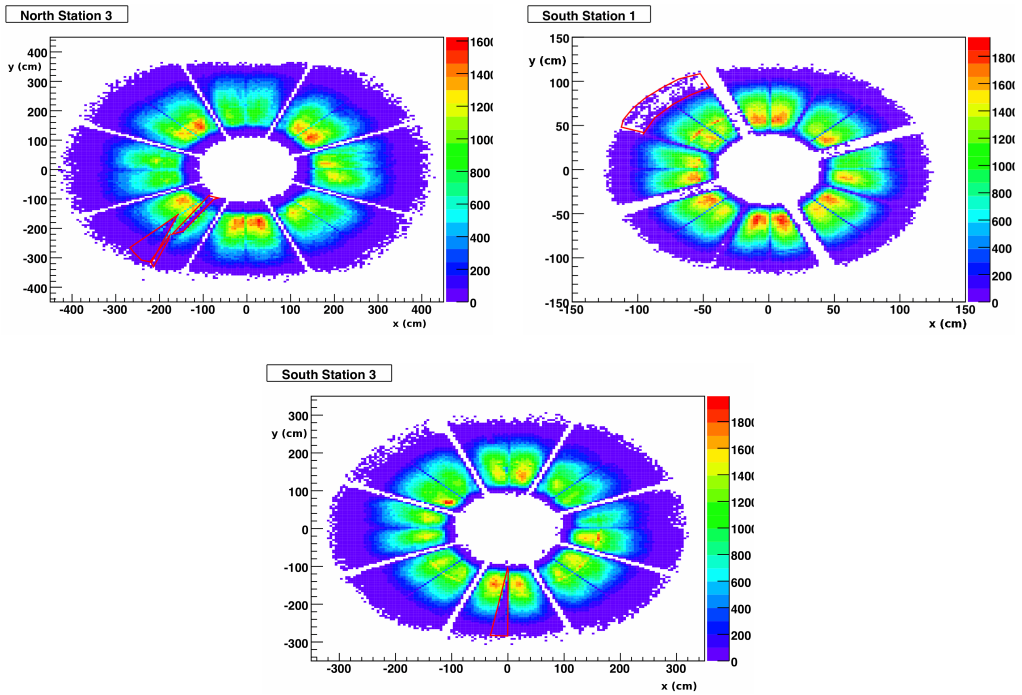

Figure 4.10: Graphical fiducial cuts on MuTR for Run 8. Plots are of y position (y axis) vs. x position (x axis) in cm. Top left, north station 3. Top right, south station 1. Bottom, south station 3.

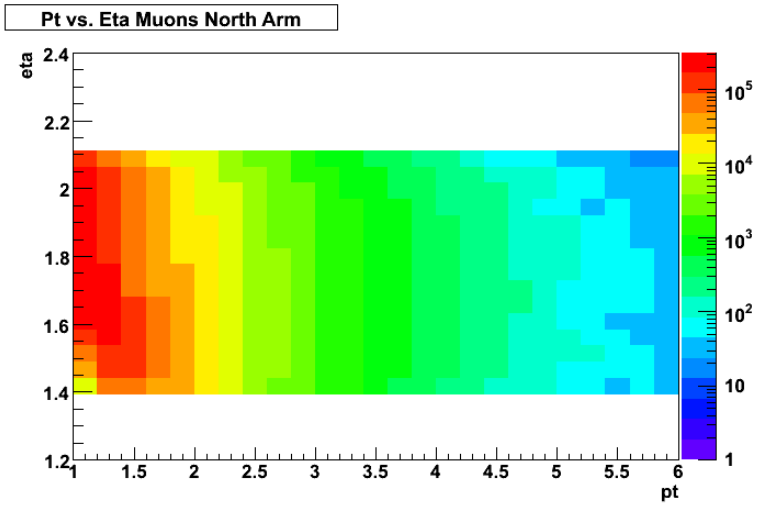

Figure 4.11: p_T vs. η for muons in the north arm in the Run 6 dataset.

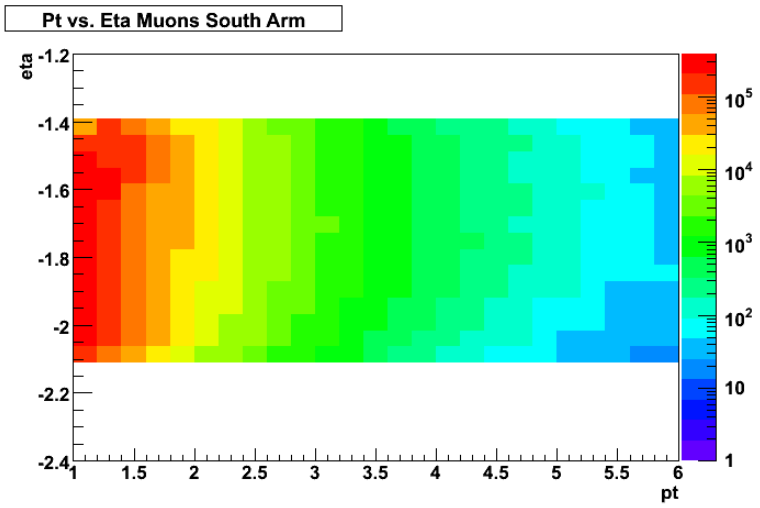

Figure 4.12: p_T vs. η for muons in the south arm in the Run 6 dataset.

4.3.2 Electron Track Requirements

Electron variable definitions

Again we must start with some definitions of the quantities used to determine good electron tracks.

- **quality**: this is a combination of Drift Chamber and Pad Chamber information in the form of a binary bit pattern. The lowest order bits (0, 1) indicate that the X wires, running parallel to the beam in the DC, have hits. The next highest bits register if hits were found (bit 2) and were unique (bit 3) in the stero UV wires. Finally the highest bits indicate that a hit was found in the PC1 (bit 4) and that it was a unique hit (bit 5). Therefore the highest quality value is 63, corresponding to a

track with the maximum number of unambiguous hits.

- n_0: this is the number of hit PMTs in the RICH within the region where a Cerenkov ring is expected to be found. For an electron the expected ring radius is 5.9 cm, and PHENIX searches for the ring in a region of outer radius 8.4 cm and inner radius 3.4 cm (to account for position resolution effects). This measurement is very sensitive to proper RICH alignment.

- n_1: the number of hit PMTs in the RICH within a radius of 11 cm from the track projection. This quantity is less sensitive than n_0 to alignment, but is more affected by noise hits.

- **prob**: the probability that a cluster in the EMCal is electromagnetic, rather than hadronic. It is calculated from the reduced χ^2 that comes from comparing the shower profile to that of an electromagnetic shower.

- *dep*: this is the deviation in sigmas of the E/p value from 1. It is defined as

$$dep = \frac{E/p - 1}{\sigma(p)} \tag{4.2}$$

  A sharp peak at $E/p = 1$ is expected for electrons. The *dep* variable includes corrections based on momentum dependence, taking into account how the width of the E/p peak varies with p_T. A plot showing this dependence is found in Fig. 4.13.

- **emc matching**: this is the radial distance from the projected track to

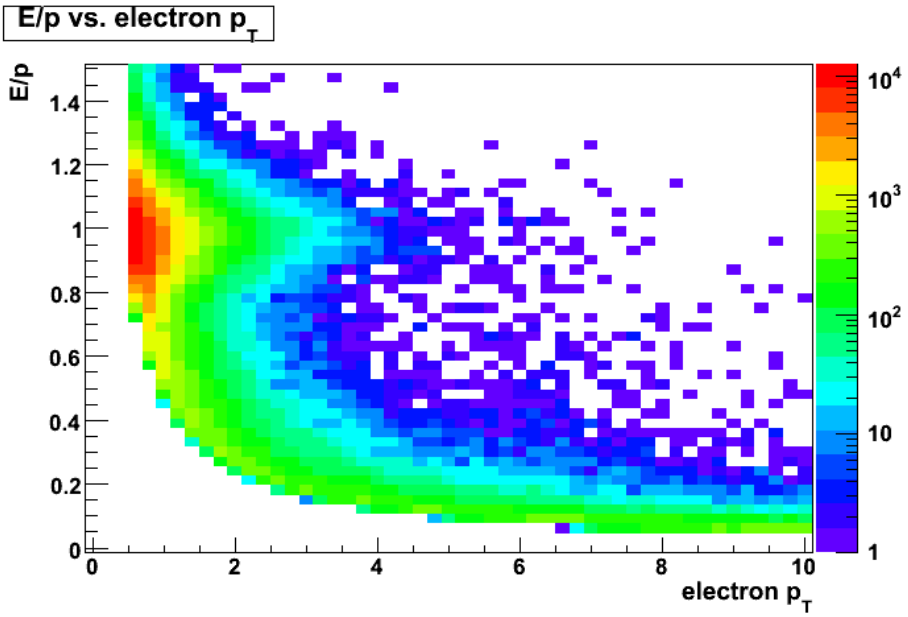

Figure 4.13: E/p vs. p_T for electron candidates. The peak at $E/p = 1$ is due to electrons that have an energy approximately equal to their momentum due to their low mass. The tail at lower E/p is mostly due to tracks from conversion electrons, which are misreconstructed to have a higher momentum than they actually have because they do not originate at the vertex (their energy is properly measured in the EMCal however).

the actual hit in the EMCal.

Electron Cuts

The electron cuts used in the e$-\mu$ analysis are based on those used in single electron analyses. However they were loosened a bit to enhance the acceptance of the rare e$-\mu$ pairs. We could accept the possibility of somewhat larger backgrounds in the electron measurement because those backgrounds are not

expected to contribute to the charge-correlated e$-\mu$ pair signal. The cuts used are as follows:

- $p_T > 0.5$
- $n_0 > 1$
- $n_1 > 1$
- quality$>$ 7 (loosened to improve statistics)
- emc matching$< 3\sigma$
- prob > 0.01 if $p_T < 5.0$ and prob > 0.2 if $p_T > 5.0$
- -2.0 $< dep <$ 3.0 for Run 6, -1.5 $< dep <$ 3.0 for Run 8. The reduced range for Run 8 is due to additional background from the presence of the HBD (see Sec. 4.3.2).

Along with the above cuts, towers that were either hot (firing significantly more than nearby towers) or dead were identified and used to cut out regions of the electron acceptance. Representative distributions of the cut variables for data from Run 6 are shown in Fig. 4.14.

Electrons variables are generally uncorrelated, as they include information from different detectors. An exception though is n_0 and n_1, which are essentially measuring the same thing (the number of electrons within a potential

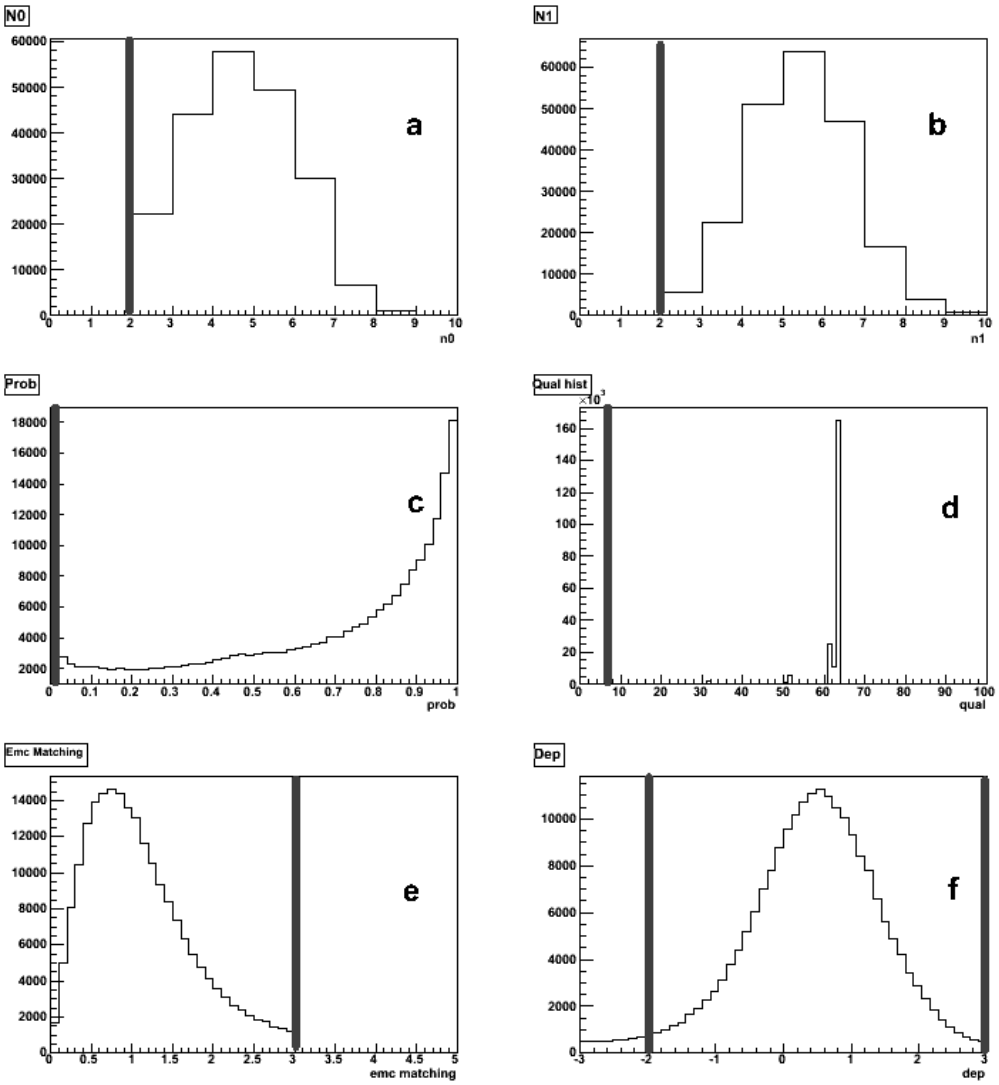

Figure 4.14: Electron cut variables for Run 6: (a) n_0 (b) n_1 (c) prob (d) qual (e) emc matching (f) dep. Vertical lines show locations of cuts.

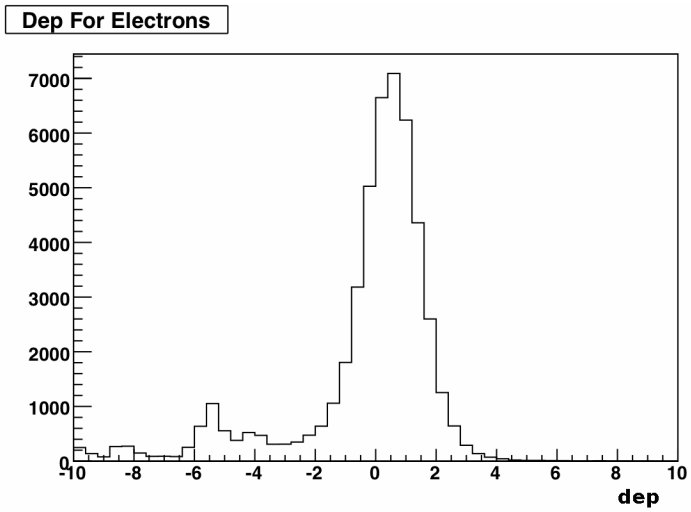

Figure 4.15: Dep distribution for electron candidates from Run 6. The tracks at low *dep* are due to photonic conversion background.

RICH ring). From analysis of the Run 8 data, the degree of correlation between these variables was found to have $\mathcal{C} = 0.76$. While both cuts are still used in this analysis, this degree of correlation was taken into account in the final systematic error.

Electron Fiducial Cuts

While no fiducial cuts were required for the Run 6 data, several were required for the Run 8. This is mostly due to the fact that the Hadron Blind Detector (HBD) had been installed in between these runs, and its support structure turned out to be a large source of conversion electrons. The background electrons landed at the very edge of the DC acceptance, the positrons in the west

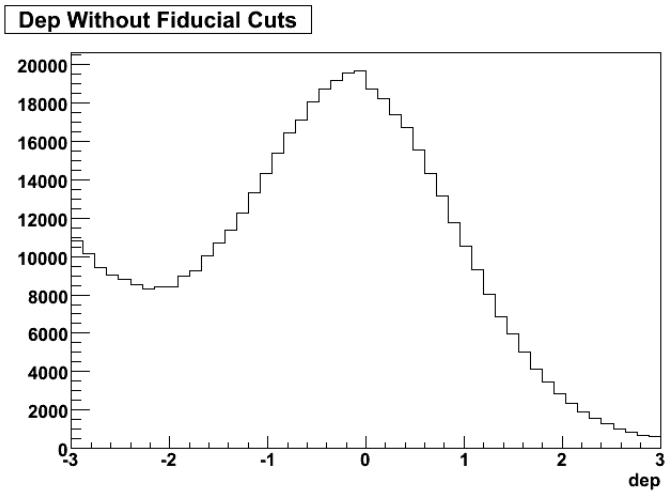

Figure 4.16: Dep distribution for electron candidates without fiducial cuts from Run 8. The high background at dep$<$ 1.5 is due to background electrons from the HBD.

arm and the electrons in the east arm. This is due to the charge separation caused by the magnetic field: different signs bend in different directions. The signs then flipped when the magnetic field was switched from ++ to −− in the middle of the run (see Fig. 4.17).

Additionally, a large segment of the PC1 went dead in the middle of the run, as can also be seen in Figs. 4.18 and 4.19. This area was removed with a fiducial cut for the appropriate run groups. A plot of *dep* for electrons after making all fiducial cuts is shown in Fig. 4.20. While much background is removed, the cut at $dep < -1.5$ is maintained to remove the remaining background photonic electrons.

After all cuts are applied, we are left with 278,642 electron candidates in

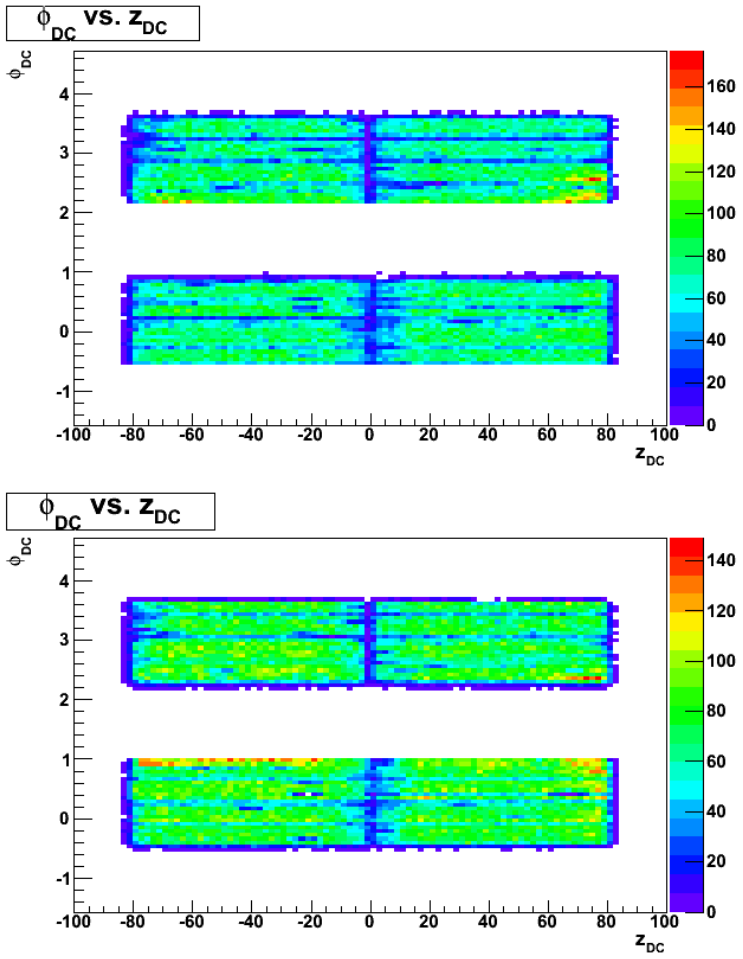

Figure 4.17: Distribution of electrons in Drift Chamber , e^+ on top and e^- on bottom for magnetic field in ++ configuration. Plotted is ϕ of DC in radians vs. z of DC in cm. Enhanced yield along inner edges is due to HDB conversion electrons

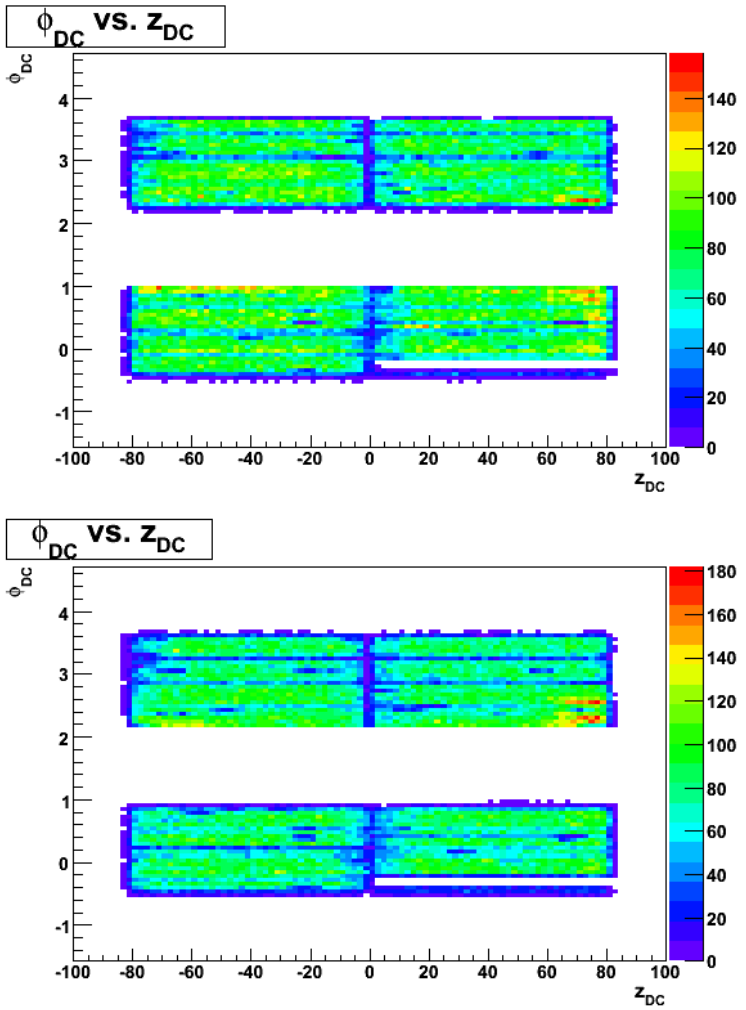

Figure 4.18: Distribution of electrons in Drift Chamber , e^+ on top and e^- on bottom for magnetic field in ++ configuration after dead area in PC1 occurred. Plotted is ϕ of DC in radians vs. z of DC in cm.

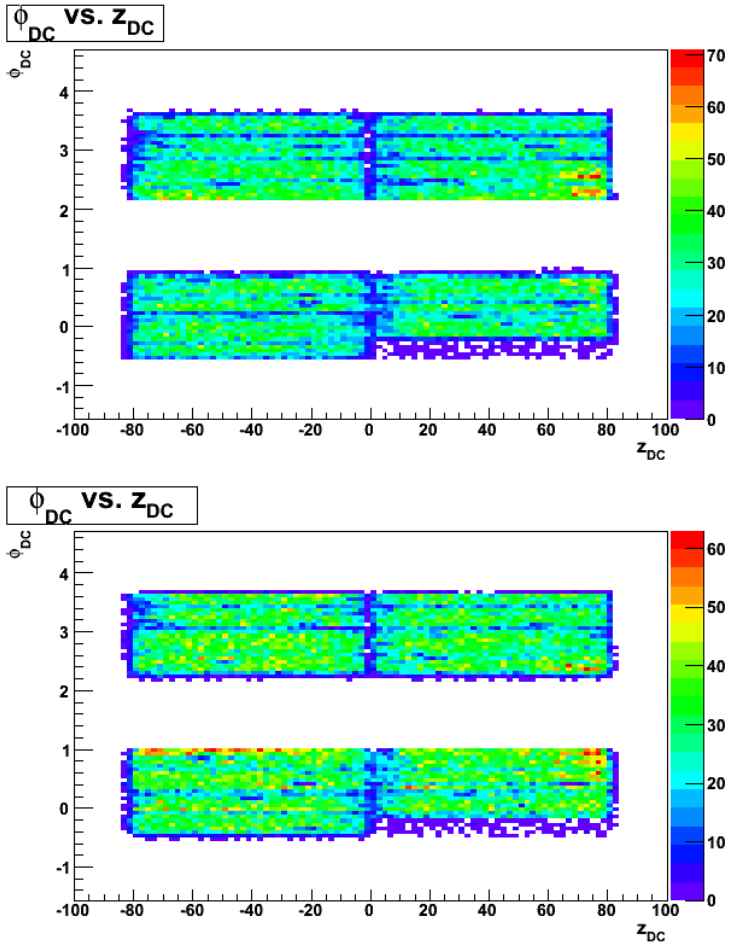

Figure 4.19: Distribution of electrons in Drift Chamber , e^+ on top and e^- on bottom for magnetic field in - - configuration. Plotted is ϕ of DC in radians vs. z of DC in cm.

Table 4.3: Electron Fiducial Cuts

regions of no acceptance	$DC\phi < -0.55$ OR $DC\phi > 3.65$
	$DC\phi > 0.1$ AND $DC\phi < 0.2$
	$DC\phi > 0.95$ AND $DC\phi < 2.2$
PC1 dead for runs > 249391	$zed > 0$ AND $DC\phi < -0.19$
HDB e^+ background ++ field	$DC\phi < 2.24$ AND $DC\phi > 1.5$
HBD e^- background for ++ field	$DC\phi > 0.9$ AND $DC\phi < 1.5$
HBD e^+ background for $--$ field	$DC\phi > 0.9$ AND $DC\phi < 1.5$
HBD e^- background for $--$ field	$DC\phi < 2.24$ AND $DC\phi > 1.5$

Table 4.4: Summary of fiducial cuts placed on electrons for Run 8.

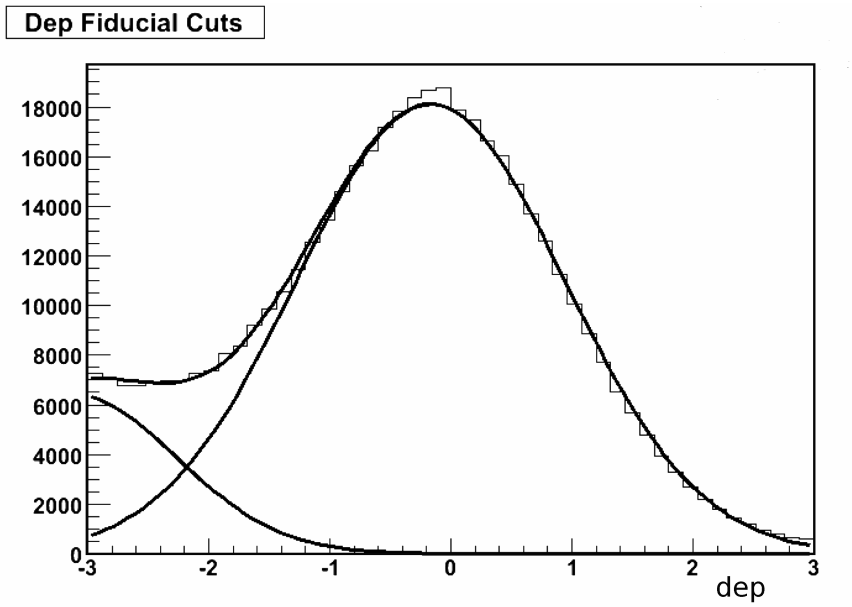

Figure 4.20: Electron *dep* for Run 8 after fiducial cuts. Fit to double gaussian to show region of signal vs. remaining background.

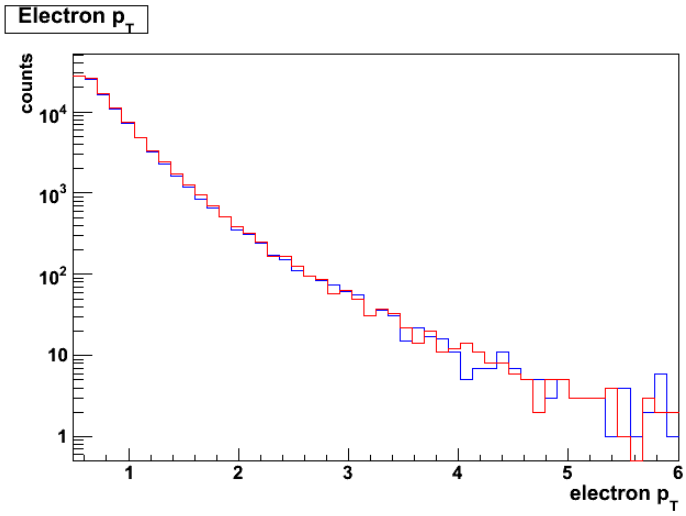

Figure 4.21: p_T distribution of single electrons in Run 6 for e^+ (red) and e^- (blue).

the Run 6 dataset and 7.53×10^6 electrons in the Run 8 dataset. The p_T distributions of the electrons are shown in Fig. 4.21.

Chapter 5

Electron-Muon Analysis in p+p and d+Au

5.1 Acceptance times Efficiency Correction

Only a small fraction of the total number of electrons and muons created in an event are reconstructed. This is mostly due to the limited acceptance region of the detectors, with smaller effects due to dead or hot electronics channels, misreconstructed tracks, and multiple scattering. A calculation of expected efficiency using simulations must be performed so that the observed yield can be correctly scaled to represent the true number of tracks. This is independent of the mixed event correction, which is also an acceptance correction but only fixes the shape of the correlation, not the yield. Simulations are performed using GEANT, a software package that simulates the passage of

particles through matter [99]. GEANT was run using a model of the PHENIX detector appropriate to the year the run took place.

If an unlimited number of simulations (and therefore disk space) were available, we would ideally do an efficiency correction for the correlated e$-\mu$ pairs as a function of several variables: p_T, η, ϕ, and z_{vtx}. Because this is not the case we must simplify the efficiency correction, and fortunately we can do this with minimal loss of accuracy. Electrons and muons are measured in different detectors that are physically separated from each other, so the measurement of one does not generally have an impact on the measurement of the other. Therefore we assume that the efficiency factorizes, so that we can simply multiply the electron and muon efficiencies to obtain the final correction factor.

The full efficiency can be written as $\epsilon(p_{Te}, p_{T\mu}, \eta_e, \eta_\mu, \phi_e, \phi_\mu, z_{vertex})$. Because the efficiency is not in general uniform over the full distribution of each variable, ideally it would be calculated in bins for each of the seven possible parameters. Even assuming electron/muon factorization, it would take an extraordinary amount of simulations to fill the bins required for a multidimensional correction. However, this type of full correction is not required for several reasons: 1) Both electron and muon efficiencies were found to be independent of the z_{vtx} (see Fig. 5.1) 2) Single particle distributions are isotropic in ϕ and are thrown that way in the simulations, so the amount lost in the areas of no acceptance is accounted for. Again the changes in shape due to dead areas are corrected for with mixed events. 3) The efficiency does depend on η, especially

for muons, but this works to shift the mean η measured. This is reflected in the η range reported (see Sec. 5.8.8).

The final efficiency corrections were done in bins in p_T, 10 bins for muons and 13 bins for electrons. The other variables are simply integrated over. Single particles were thrown with a realistic η spectrum and a flat p_T. Because of the exponential nature of the p_T distribution, if particles were thrown with a realistic distribution there would be almost none falling in the upper p_T bins: therefore a flat distribution was thrown, and weighted realistically after reconstruction. Electrons were thrown with a p_T range of 0.1-10.0 GeV, and muons within a range of 0.5-10.0 GeV. The efficiency was calculated using

$$\epsilon(p_T) = \frac{N_{\text{reconstructed}}}{N_{\text{thrown in } \eta \text{ and } \phi \text{ window}}} \tag{5.1}$$

The p_T range thrown is a wider range than measured, as contributions of particles that originate at lower p_T and are reconstructed with a higher p_T must be accounted for. This is known as the "bleed-over" effect (see Fig. 5.3) and is more important for muons, given the worse momentum resolution of the MuTR compared with the central arms. Some muons that have low p_T bleed in to the kinematic region measured, while others are reconstructed with lower p_T and hence bleed out and are not included in the e$-\mu$ pairs (the contribution from lower p_T bins for electrons is negligibly small). This effect also works within the p_T bins: an electron that is thrown between 0.75 and 1.0

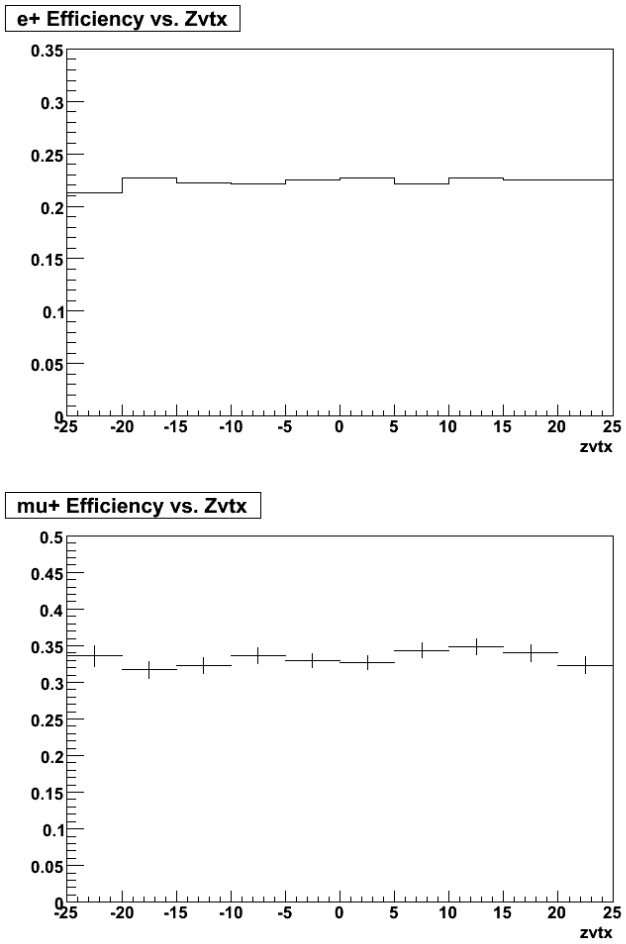

Figure 5.1: Efficiency of e^+ (top) and μ^+ (north arm) as a function of z vertex. Because little variation is seen with changing z_{vtx} bin, the efficiencies are approximated as independent of vertex position.

GeV may get reconstructed in a range of $0.5 - 1.25$ GeV or so, meaning that when we run simulations for one p_T bin we must look a wider p_T window after we have reconstructed the tracks. The efficiency is then found as a function of reconstructed p_T (since that is all we can measure in the data) summing contributions from all thrown bins.

The bleed over effect is also found in η, in that particles from different η regions can end up in the acceptance due to reconstruction effects. The contribution from muons outside the η acceptance was evaluated and found to be only a $1 - 2\%$ effect, therefore insignificant (Fig. 5.2). Because of this the simulated muons were thrown within the measured range of $1.4 < |\eta| < 2.1$. Electrons were thrown within a range of $-0.5 < \eta < 0.5$ to account for the effect of different ηs being accepted depending on where the z_{vtx} is. All simulated distributions were given vertices based on the real z_{vtx} distribution for the given run.

For the efficiencies to be valid, it is necessary that simulated electrons and muons are as identical as possible to the electrons and muons in data. To ensure this, the distributions of variables used for cuts were compared. In Figs. 5.4 and 5.5 we see the comparison of simulation to data for muons from Run 8 (data from Run 6 is similar). The comparison of electron distributions is shown in Figs. 5.6 and 5.7.

As an aside, while it is accurate to compute p+p efficiencies by throwing and

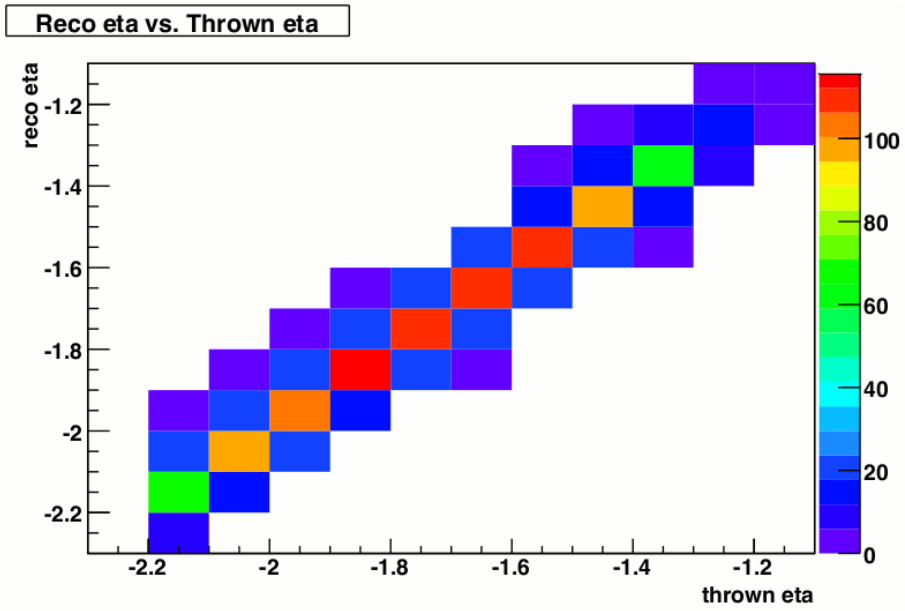

Figure 5.2: "Bleed over" effect for muons in south arm. Shown, in bins of width 0.1 in η, is the reconstructed η as a function of thrown η. Most muons are reconstructed in an η bin within 0.1 of the thrown value.

Table 5.1: Muon efficiencies for Run 6 and Run 8

Pt bin	Run 6 north	Run 6 south	Run 8 north
1.0-1.25	0.379	0.459	0.372
1.25-1.5	0.503	0.568	0.521
1.5-1.75	0.560	0.614	0.570
1.75-2.0	0.581	0.631	0.597
2.0-2.5	0.596	0.647	0.593
2.5-3.0	0.601	0.653	0.605
3.0-3.5	0.602	0.654	0.615
3.5-4.0	0.602	0.656	0.623
4.0-4.5	0.604	0.657	0.630
4.5-10.0	0.607	0.658	0.628

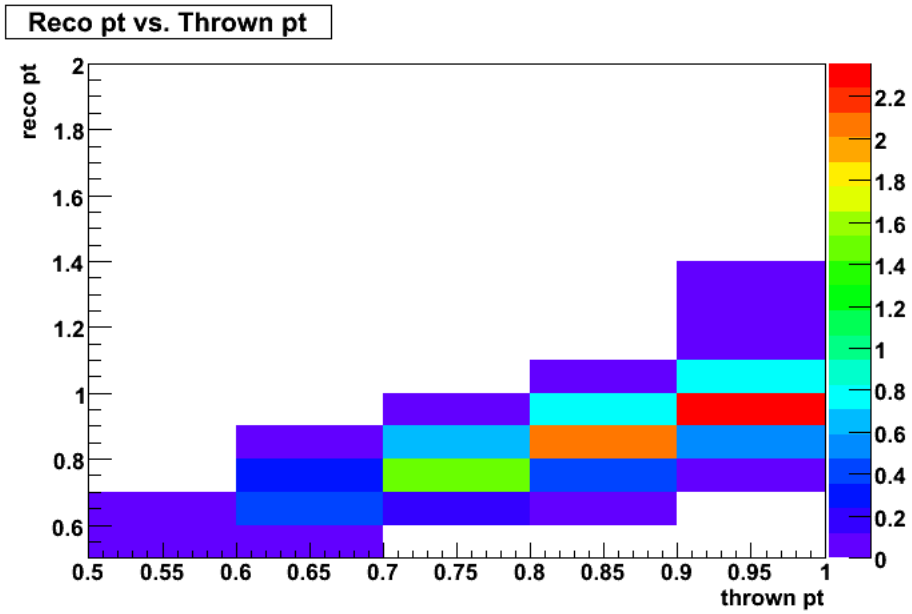

Figure 5.3: "Bleed over" effect in p_T for muons in the north arm. Reconstructed p_T as a function of thrown p_T for range $0.5 < p_T < 1.0$. Because muons are required to have $p_T > 1.0$, this shows that only a small fraction ($< 1\%$) of muons at low p_T originated in a p_T region outside of the measured kinematic range.

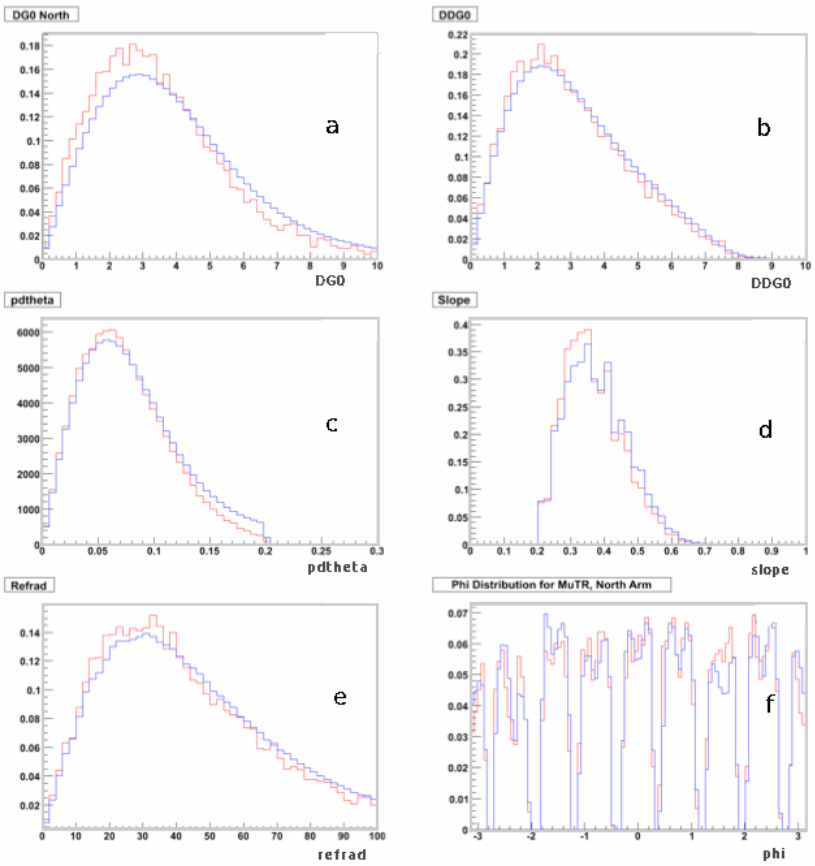

Figure 5.4: Comparison of simulated PISA muons to data for Run 8 north arm. Data is in blue, PISA is in red. Variables are as follows: a) DG0 b) DDG0 c) p$\delta\theta$ d) slope e) refrad f) ϕ in muon arms.

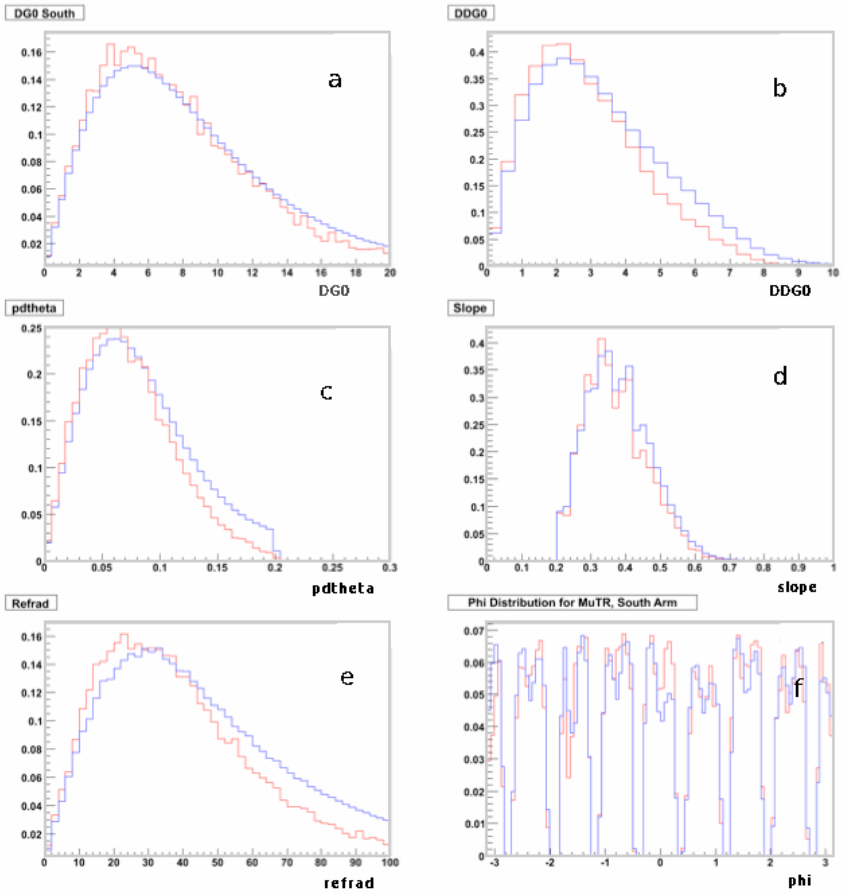

Figure 5.5: Comparison of simulated PISA muons to data for Run 8 south arm. Data is in blue, PISA is in red. Variables are as follows: a) DG0 b) DDG0 c) p$\delta\theta$ d) slope e) refrad f) ϕ in muon arms.

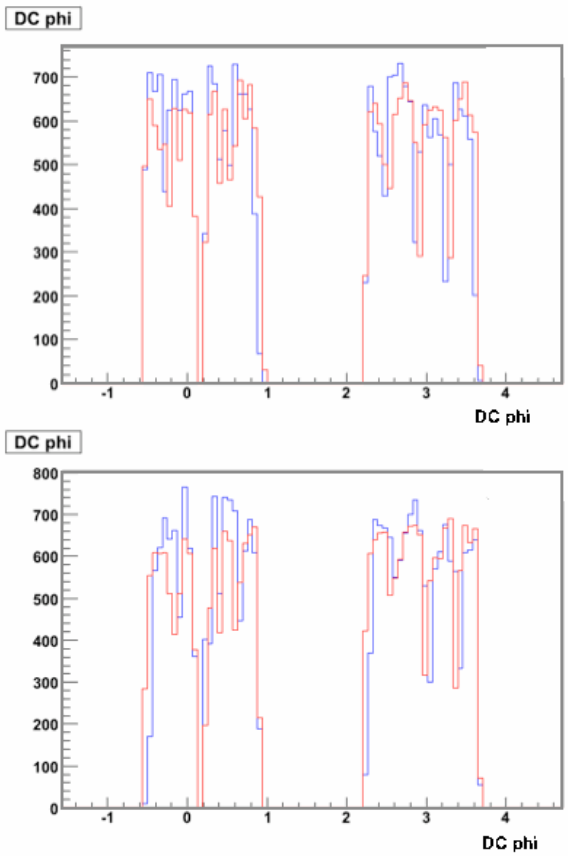

Figure 5.6: Drift Chamber ϕ distribution for e^+ (top) and e^- (bottom) for PISA (red) vs. data (blue). Data taken from Run 8 dataset.

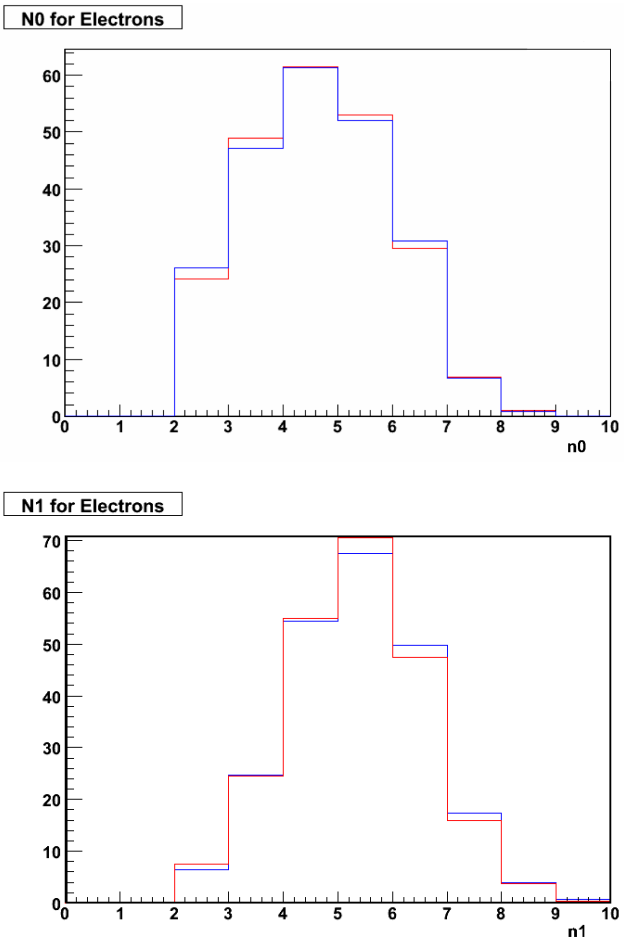

Figure 5.7: n0 (left) and n1 (right) for data (blue) vs. PISA (red). Data taken from Run 8 dataset.

Table 5.2: Electron efficiencies for Run 6 and Run 8

Pt bin	Run 6 e^+	Run 6 e^-	Run 8 e^+	Run 8 e^-
0.5-0.75	0.162	0.166	0.193	0.187
0.75-1.0	0.204	0.198	0.203	0.199
1.0-1.25	0.210	0.200	0.204	0.199
1.25-1.5	0.205	0.208	0.207	0.207
1.5-1.75	0.217	0.207	0.209	0.206
1.75-2.0	0.223	0.211	0.208	0.215
2.0-2.5	0.217	0.217	0.206	0.210
2.5-3.0	0.224	0.215	0.211	0.212
3.0-3.5	0.225	0.222	0.208	0.210
3.5-4.0	0.223	0.225	0.211	0.215
4.0-4.5	0.222	0.222	0.207	0.210
4.5-5.0	0.217	0.217	0.203	0.206
> 5.0	0.207	0.208	0.192	0.193

reconstructing single particles, generally it is not accurate to use this method for heavy ion collisions. This is because it is easier to misreconstruct tracks in a high occupancy environment, such as exists in Au+Au collisions. In cases such as these, single tracks are embedded into real events, then retrieved again after reconstruction. The efficiency after embedding tends to be significantly lower than that obtained from single particles alone. In the case of the d+Au analysis, embedding was attempted, but it was found that the effect on altering efficiencies was negligible. This was especially true in the case of the north arm, and because only the north arm signal is studied in this analysis it was decided not to use embedding (the choice of north arm only will be discussed later).

5.2 Trigger Requirement

PHENIX has triggers that fire for muons and electrons, but at least during Run 6 there was no joint electron-muon trigger. For this reason the MuID LL1 deep trigger (Sec. 3.2.4) was used to select on events that have a muon, and then events that also contained an (untriggered) electron were selected. For both Run 6 and Run 8, the MuID LL1 deep trigger was ANDed with the BBC minimum bias trigger (see Sec. 3.2.4), and this combination trigger was used in this analysis. The number of events skipped is controlled by the "scaledown" factor, which allows only a fraction of events firing the trigger to be kept. This is to ensure that the datasets are of a reasonable size. The signal e$-\mu$ pairs used come entirely from the MuIDLL1 deep triggered dataset, because this dataset contains MuID roads that reach gap 3 or gap 4: the data from gap 3 is crucial for background measurements, described later.

The goal of this analysis is to get a measurement of the number of e$-\mu$ pairs per minumum bias event. In order to get the number of minumum bias events from the triggered sample, we must use the relation,

$$N_{MB} = rej \times N_{trig} \tag{5.2}$$

where N_{MB} is the number of minbias events, rej is the trigger rejection and N_{trig} is the number of events in the triggered sample. The rejection is found

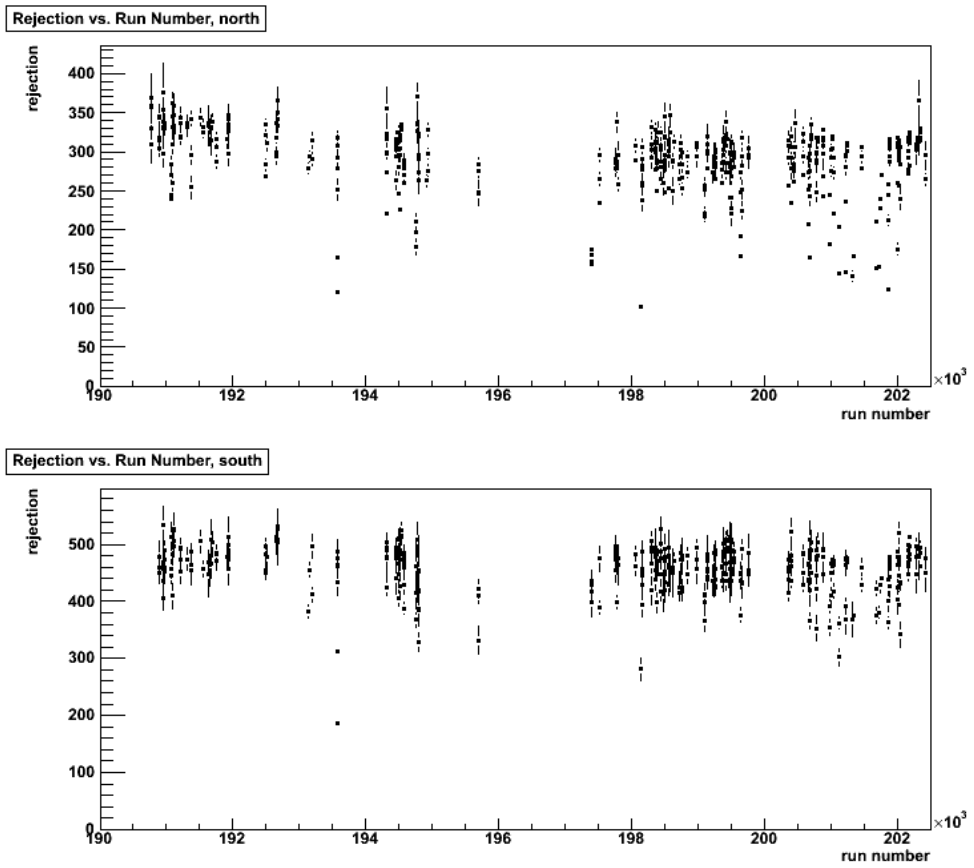

Figure 5.8: Run 6 rejection factors for MuIDLL1 north (top) and south (bottom) as a function of run number.

by dividing the number of triggered events by the total number of events in a minbias dataset. The run-by-run variation in rejection values is shown in Figs. 5.8, 5.9.

The trigger efficiency is given by the fraction of tracks that meet all trigger requirements that actually fire the trigger. The final pair yield must be corrected up by a factor $1/eff_{trig}$ to correct for muon tracks that are missed by

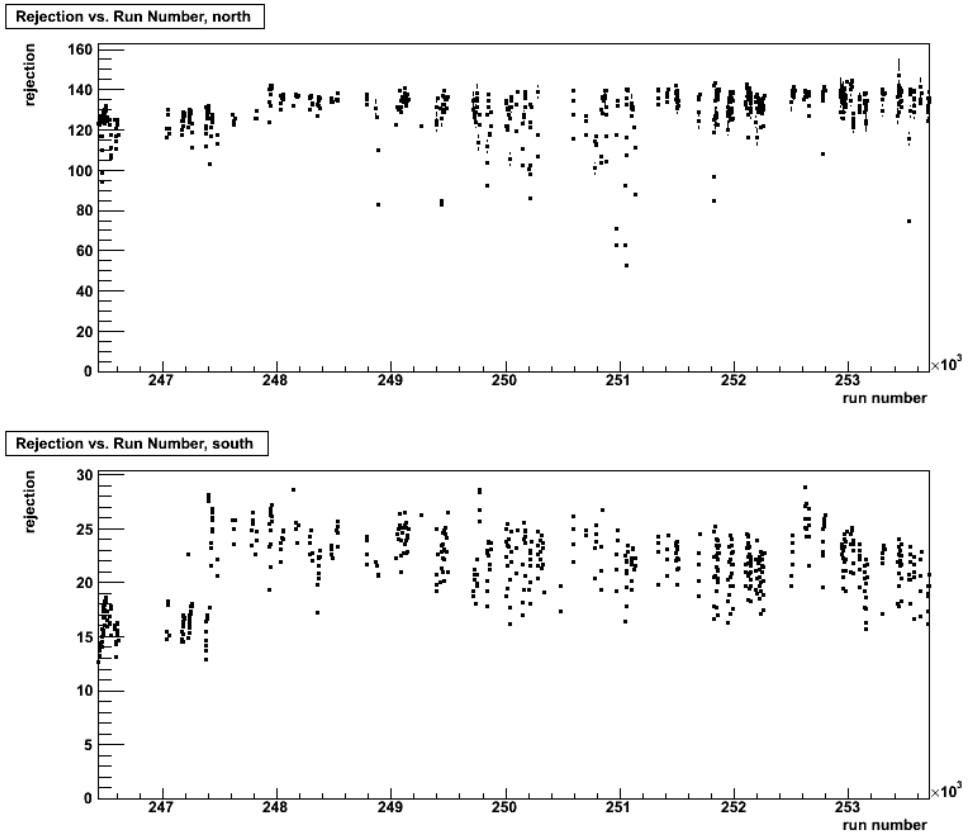

Figure 5.9: Run 8 rejection factors for MuIDLL1 north (top) and south (bottom) as a function of run number.

Table 5.3: Trigger Efficiency for the MuIDLL1 deep triggers.

	North 1 Deep	South 1 Deep
Run 6 pp gap 4	0.961	0.961
Run 6 pp gap 3	0.982	0.985
Run 8 dAu gap 4	0.954	0.961

Table 5.4: Trigger Efficiency for the MuIDLL1 deep triggers in Run 8 for Gap 3 tracks vs. p_T.

p_T range	North 1 Deep	South 1 Deep
1-2 GeV	0.824	0.846
2-3 GeV	0.826	0.868
3-4 GeV	0.858	0.882
4-5 GeV	0.884	0.901
$>$ 5 GeV	0.844	0.923

the trigger. In the case of the MuIDLL1 deep trigger, these are tracks that reach gap 3 or gap 4 of the MuID. A summary of the average deep trigger efficiency for the two runs is given in Table 5.3. For the trigger on gap 3 tracks in Run 8 a strong p_T dependence was found. These efficiency values are shown in Table 5.4.

5.3 Pair Corrections

After making track cuts, we are left with the number of pairs found in Table 5.5. Besides the cuts made to select good electron and muon tracks, other corrections must be made to the pair distribution. The pair distribution must be

Table 5.5: Number of raw pairs left after track cuts by run and arm.

Run and Arm	Opposite Sign Pairs	Same Sign Pairs
Run 6 north	3459	2894
Run 6 south	4154	2894
Run 8 north	24,457	21,256

corrected for the acceptance of PHENIX, since it does not have full azimuthal coverage in the central arms. The efficiency for triggering on e$-\mu$ pairs must be accounted for so that the final yield is independent of detector effects. Also the combinatoric background must be removed, which is accomplished using a like-sign subtraction.

5.3.1 Like-sign Subtraction

What we are looking for in this analysis is a signal of opposite sign e$-\mu$ pairs. Apart from the heavy quark signal, opposite and like sign e$-\mu$ pairs arise in the same way, from either random combinatorics or from light quark decays. These sources produce opposite and like sign pairs in equal numbers, so the only difference between the distributions is the opposite sign heavy flavor signal. Because of this, the like sign distribution is a good measure of the combinatoric and light quark background. To remove this background we can subtract the like sign distribution.

In order to subtract the like sign, we must apply the proper normalization

[100]. For identical particles there is a relative normalization between like sign and opposite sign pairs, as shown in a previous PHENIX single electron analysis [101]. It was there shown that the relative normalization may be calculated as

$$\langle n_{+-} \rangle = 2\sqrt{\langle n_{++} \rangle \langle n_{--} \rangle} \tag{5.3}$$

where n_{+-} is the per-event rate of opposite sign pairs and n_{++} and n_{--} are the rate for like sign pairs.

For non-identical particles we can follow the same procedure as in [101]. Let $n_{\mu+}$, $n_{\mu-}$, n_{e+}, and n_{e-} be the number of detected particles of a given species and charge sign in a particular event. They are related to the actual number generated, $N_{\mu+}$, $N_{\mu-}$, N_{e+}, N_{e-} by the detection efficiencies, $n = \epsilon N$. The probablity to detect n particles out of N with an effiency of ϵ is binomial

$$B\left(n, \epsilon\right) = \frac{N}{n!\left(N-n\right)!} \epsilon^n \left(1-\epsilon\right)^{N-n} \tag{5.4}$$

with a well definied mean, ϵN.

Starting with the numbers of particles in the given event, we can determine

the pair rates. We will consider μ^+ and e^+ as a specific case.

$$\begin{aligned} n_{\mu+e+} &= \sum\sum n_{\mu+} n_{e+} B\left(n_{\mu+}, \epsilon_{\mu+}\right) B\left(n_{e+}, \epsilon_{e+}\right) \\ &= \sum n_{\mu+} B\left(n_{\mu+}, \epsilon_{\mu+}\right) \sum n_{e+} B\left(n_{e+}, \epsilon_{e+}\right) \\ &= \epsilon_{\mu+}\epsilon_{e+} N_{\mu+} N_{e+} \end{aligned} \tag{5.5}$$

This is true for any charge and species combination. Therefore, we can write the like-sign pairs as

$$\begin{aligned} n_{\text{like}} &= n_{\mu+e+} + n_{\mu-e-} \\ &= \epsilon_{\mu+}\epsilon_{e+} N_{\mu+} N_{e+} + \epsilon_{\mu-}\epsilon_{e-} N_{\mu-} N_{e-} \end{aligned} \tag{5.6}$$

This will further reduce when we note that the efficiency and the rate for electrons and positrons are the same. Therefore, the like-sign can be reduced to

$$n_{\text{like}} = \epsilon_e N_e \left(\epsilon_{\mu+} N_{\mu+} + \epsilon_{\mu-} N_{\mu-}\right) \tag{5.7}$$

The μ^+ and μ^- rates are indeed different (due to interactions in the absorber) and therefore, this cannot be further reduced. We can also write down the rate for unlike-sign pairs as

$$\begin{aligned} n_{\text{unlike}} &= n_{\mu+e-} + n_{\mu-e+} \\ &= \epsilon_{\mu+}\epsilon_{e-} N_{\mu+} N_{e-} + \epsilon_{\mu-}\epsilon_{e+} N_{\mu-} N_{e+} \\ &= \epsilon_e N_e \left(\epsilon_{\mu+} N_{\mu+} + \epsilon_{\mu-} N_{\mu-}\right) \end{aligned} \tag{5.8}$$

In the last line we used the fact again that the electron and positron rates and efficiencies are the same. Comparing Eqn. 5.7 and Eqn. 5.8 yields the same rate of like- and unlike-sign pairs. This result is easy to interpret. Because the electron and positron rates are not different, they do not contribute any differences to the pair rate. Because there are fewer negative muons than positive, the reduction in the like-sign pairs is the same as the reduction to the unlike-sign pairs. Therefore, there is no relative normalization between the like- and unlike-sign pairs.

5.3.2 Event Mixing

Event mixing is used to correct the shape of the correlation distribution for the acceptance. In PHENIX, event mixing is crucial because the central detectors only cover half of the azimuthal acceptance. This causes a distribution that is originally flat in azimuth to pick up a strong dependence on ϕ, and mixed events are used to correct back to the flat distribution. The effect is lessened for e$-\mu$ because the muon detectors cover almost a full azimuthal acceptance. The the mixed correction is given by:

$$M(\Delta\phi) = \frac{\int \Delta\phi \ \mathrm{Mix}_{q,Q,a}\left(\Delta\phi\right)}{2\pi \mathrm{Mix}_{q,Q,a}\left(\Delta\phi\right)} \tag{5.9}$$

This factor multiplies the signal distribution. In the limit of full azimuthal acceptance, the mixed distribution would be flat and would not change the

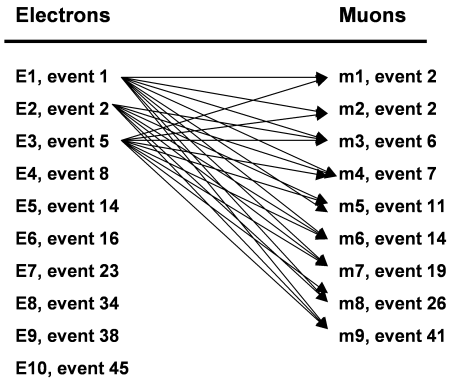

Figure 5.10: Example of how mixing works, showing the mixing of three electrons with the muon pool.

signal. The efficiencies are independent of the mixed acceptance correction in that they correct the yield rather than the shape: these are discussed in Sec. 5.1.

In order to do the mixing, electron and muon tracks from different events are stored in separate pools, where each pool corresponds to a different z_{vtx} range. There are 20 pools, each containing events within a 2.5 cm range in z_{vtx}. For the d+Au dataset, events are also broken up into 4 separate centrality pools, giving 80 pools in total. The pools are filled until there are at least 10 muons in the muon pool, and then each electron is mixed with each muon in the respective pools, unless the two came from the same event (see Fig. 5.10). When each particle has been mixed both pools are cleared, and the process starts again. In this analysis, muons from deep triggered muon events were mixed with electrons from minimum bias events to reduce the trigger bias.

The correlation distribution is corrected by the mixed events by first normalizing the mixed distribution to 2π. Then the real is divided by the mixed, and divided by the bin width to give $dN/d\Delta\phi$. Below are examples of the mixed event opposite sign as well as like sign distributions after mixing muons from Muon triggered events with electrons from minimum bias events (Fig. 5.11). They are mostly flat with a slight sinusoidal modulation as one would expect due to the acceptance of the central arms. Separate mixed distributions are created for different sign combinations, since the magnetic field gives a slightly different acceptance to particles of different signs. Also different mixed distributions were created for run groups that differed from each other by an added fiducial cut. Three run groups were used for the Run 8 dataset, corresponding to the initial "++" magnetic field, the "++" magnetic field with the PC1 dead area, and the "- -" field with the PC1 dead area. Run 6 was divided into two groups for the purpose of creating mixed events, corresponding to two run groups with slightly different average electron rates.

5.4 Inclusive Distributions

Figs. 5.12 and 5.13 show inclusive distributions for e$-\mu$ pairs in p+p and d+Au north arm respectively. They have been corrected using mixed events, but not for efficiency. We see there is a much larger pedestal for opposite and like sign pairs in the Run 8 data, indicating more background. This is likely due to

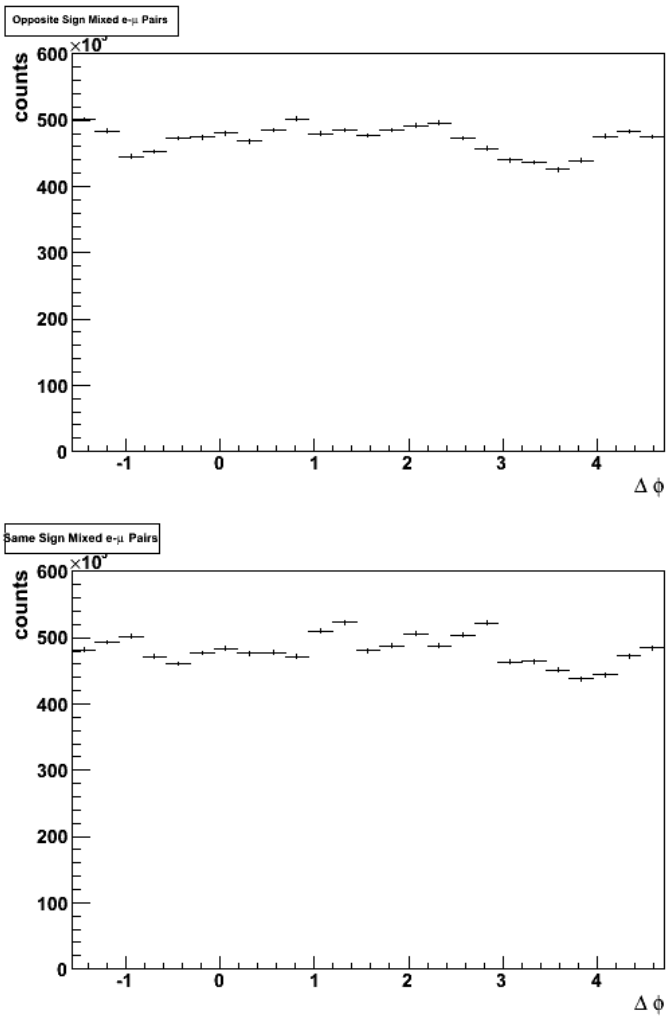

Figure 5.11: Example mixed distribution as a function of azimuthal angle for $e^-\mu^+$ (top) and $e^+\mu^+$ pairs (bottom) from Run 6.

N_{coll} scaling, where N_{coll} is about 7.6 for minimum bias d+Au collisions (see discussion in Sec. 6.1. While this background is still removed with a like sign subtraction, the error bars on the final distribution are larger now than for the p+p.

We can see a big difference in comparing the north arm in Run 8 (Fig. 5.13) to the south arm (Fig. 5.14). The pedestal level in the inclusive is about twice as big for the south arm in this uncorrected distribution. Because of the huge amount of background underneath the heavy flavor peak, it is impossible to see a heavy flavor signal in the like sign subtracted distribution. This is most likely due to the dominance of soft processes in the gold-going (south arm) direction. For this reason it was decided to only study the north arm pairs, which is the deuteron-going direction, using the Run 8 data.

5.5 Verification of Corrections using Pythia

To test the self-consistency of the acceptance and efficiency corrections, the analysis was run on Pythia simulation files that were run through PISA (the PHENIX GEANT simulator), then fully reconstucted. Pythia was run on the charm setting (MSEL=4), and 100 million events were produced. All semi-leptonic decays of D mesons were turned on, and a minimum parton p_T was set to 1.0 GeV/c. A trigger on e$-\mu$ pairs was used to cut down on file size.

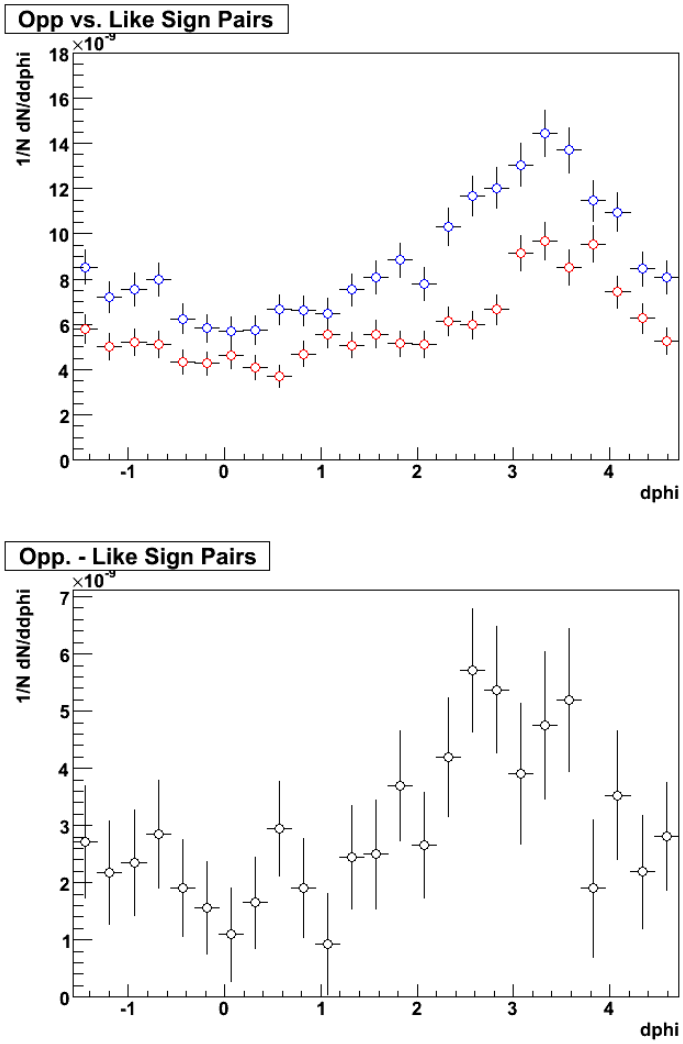

Figure 5.12: Inclusive distributions for Run 6 p+p, north arm. Top is opposite sign (blue) vs. like sign (red), bottom is opposite - like sign.

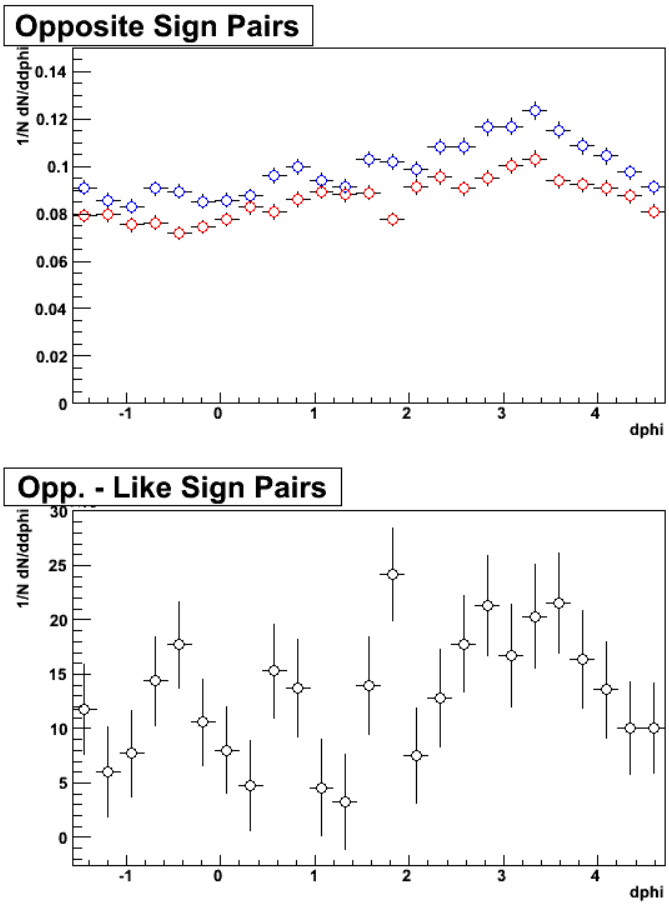

Figure 5.13: Inclusive distributions for Run 8 d+Au, north arm. Top is opposite sign (blue) vs. like sign (red), bottom is opposite - like sign.

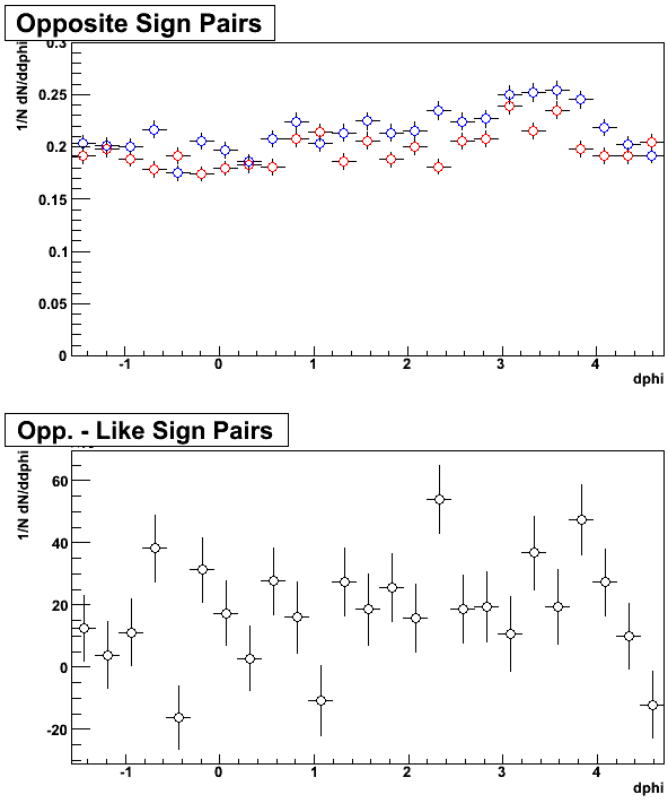

Figure 5.14: Inclusive distributions for Run 8 d+Au, south arm. Top is opposite sign (blue) vs. like sign (red), bottom is opposite - like sign.

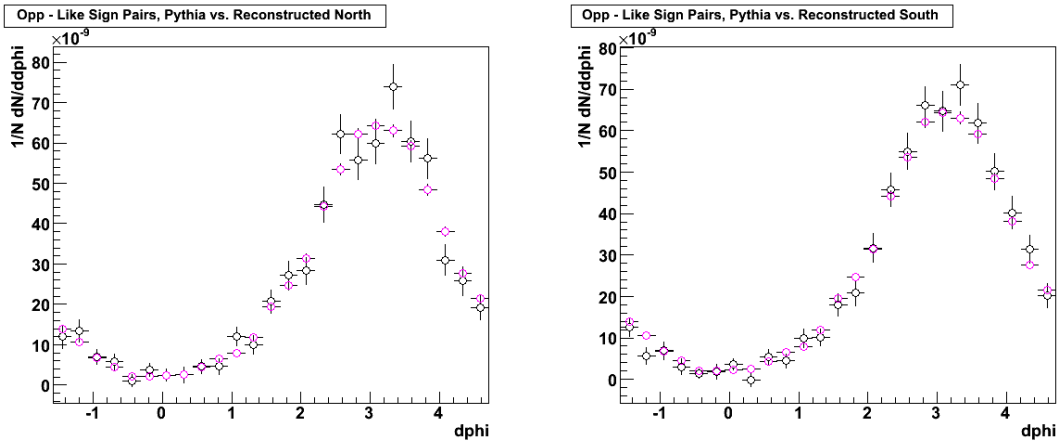

Figure 5.15: $\Delta\phi$ distribution for generated Pythia e$-\mu$ events (magenta) vs. the same events after full reconstruction and analysis cuts and corrections (black). North events are on the left and south events are on the right.

The Pythia events were then used as input to PISA, and run through a full reconstruction using the Run 6 settings. PISA is used to simulate the signals produced in the detector from the Pythia events, taking into account absorption, multiple scattering, and longer range decays. A full analysis was run on the output, including efficiency correction, dividing by mixed events, and all cuts. The results are shown in Fig. 5.15. Only statistical errors are plotted. The overall difference in integrated number of pairs between the Pythia and the reconstruction is less than 1%, indicating the differences in the angular distributions are due to random fluctuations and slight discrepancies in azimuthal angle not accounted for with mixed events. Because of the good agreement between the generated distribution and the reconstructed distribution we have confidence in the corrections performed on the data.

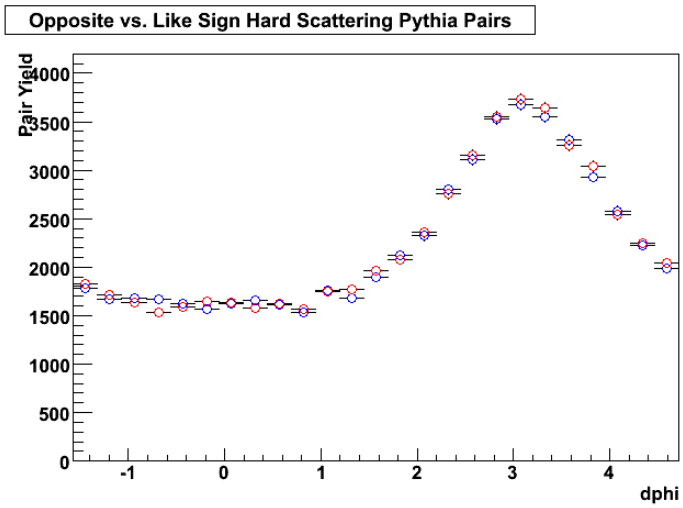

Figure 5.16: $\Delta\phi$ distribution for Pythia e$-\mu$ pairs arising from hard scattering. Opposite sign is in blue, same sign is in red. This demonstrates the validity of the like-sign subtraction for removing non-charm e$-\mu$ pairs.

5.6 Backgrounds

There are many sources of electrons and muons in PHENIX besides heavy flavor. Some of these will appear to be correlated due to random combinatorics, and could contribute to the opposite and like sign e$-\mu$ distributions. Even if non-heavy flavor pairs are created, though, they will not be charge correlated: the pairs will be random combinations so there will be as many opposite sign pairs created as same sign pairs. This means that the like sign subtraction should remove these sources of background. For confirmation of this, see Fig. 5.16: it shows e$-\mu$ pairs from Pythia hard scattering with charm removed. At $\Delta\phi \approx \pi$, which is our acceptance region, opposite and same sign pairs are measured in equal amounts.

Although all backgrounds are expected to be eliminated with the like sign subtraction, it is still important to confirm this with the analysis. Furthermore there is a case where background would not subtract out, which is background related to charm decay. For example, charged kaons from D decay or muons resulting from the decay of those Ks could show a charge correlation with electrons in the event. For this reason we take special care to evaluate the background from punchthrough hadrons as well as muons from light meson (pion and kaon) decay. Because of the low statistics, we take any background not consistent with 0 within 2 standard deviations to be significant. We also measured the correlations involving photonic electrons, mostly as a check of the method in that photonic electrons should not contribute to a charge correlated signal.

5.6.1 Decay Muon Background

A major source of background in the muon arms results from muons that are created by light hadron decay. On a track-by-track basis these are indistinguishable from from heavy flavor muons, since PHENIX is not equipped with detectors that can resolve the position of the secondary decay vertex. In the future, the silicon vertex detectors at PHENIX will be able to resolve the decay length of the muon's parent, thereby determining if it came from a D (short decay distance) or a light meson (much longer decay distance). For now, though, the only property of the decay muons we can use to distinguish

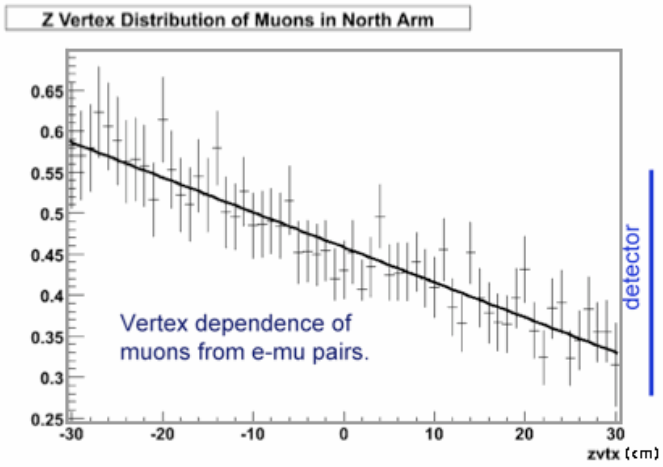

Figure 5.17: z_{vtx} dependence of muons in e$-\mu$ pairs measured in the north muon arm, corrected for detector acceptance as a function of z_{vtx}.

them is their dependence on z_{vtx}. The farther the collision is from one of the muon detectors, the more likely it is that pions and kaons will decay to muons before the tracks are measured (see Fig. 5.17). Prompt muons from heavy flavor show no such vertex dependence.

Because the majority of decay muons come from z_{vtx} positions far from the detctor, naively one could simply make a cut on the vertex being close to the detector to reduce their contribution. This would remove a lot of the signal, though, and is not advisable for an analysis such as this that is already statistics limited. To study the decay contribution to the $\Delta\phi$ spectrum, the signal was divided into two regions: farther from the detector ($z_{vtx} < 0$ for north arm muons, $z_{vtx} > 0$ for south arm muons) and nearer to the detector ($z_{vtx} > 0$ for north, < 0 for south). Then the near distribution was subtracted

from the far distribution. Muons with no vertex dependence should have equal contributions in both regions, but decay muons should be preferably found far from the detector. If a non-zero contribution was found in the far - near distribution after the like sign subtraction, decay muons would be found to contribute to the signal. As we can see in Table 5.6, all decay distributions fit flat lines that are consistent with 0. Therefore no significant decay muon background contribution was found.

One important caveat is that the method used to measure decays only measures a fraction of the total sample. The decay distribution shows a linear increase as a function of z_{vtx} for both the near side and far side distribution. The near side subtraction removes the component that does not depend on z_{vtx} (the heavy flavor muons), but also some of the decays. The fraction that is left was estimated by assuming the decay contribution goes to zero an interaction length past the absorber. If this is true we would only be seeing 22% of the decay muons in these decay distributions. While this fraction is not important for background subtraction (since this background does not need to be subtracted), it will become important in the evaluation of systematic errors. For the derivation of this quantity, please see Appendix A.

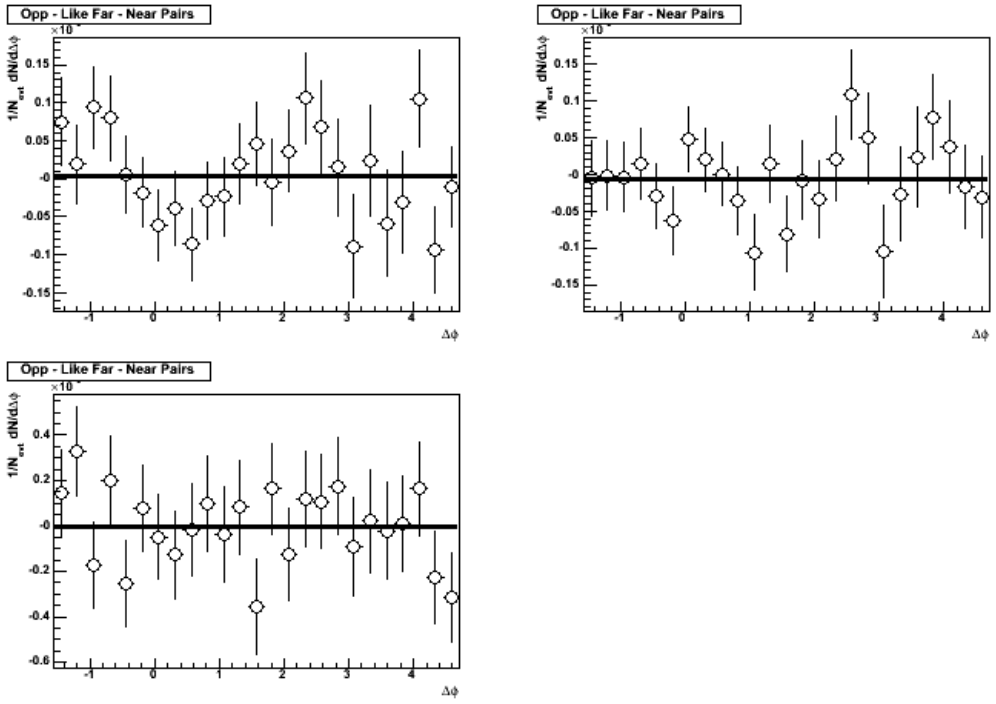

Figure 5.18: Like sign subtracted decay distributions as a function of $\Delta\phi$ for Run 6 north (top left), Run 6 south (top right), and Run 8 north (bottom left).

Table 5.6: Decay Background Linear Fit Values

Run and Arm	Value	Error
Run 6 North	2.85 $\times 10^{-9}$	1.13 $\times 10^{-8}$
Run 6 South	-7.07 $\times 10^{-9}$	1.05 $\times 10^{-8}$
Run 8 North	-5.10 $\times 10^{-9}$	4.14 $\times 10^{-8}$

5.6.2 Punchthrough Hadrons

Even though the muon absorber does a good job of eliminating background, it is still possible for some hadrons to "punch through" the absorbers so that their tracks are detected in the last gap of the MuID. For tracks that make it that far, hadrons are indistinguishable from muons, which poses a problem for muon backgrounds. However, if one looks at the p_z (longitudinal momentum) distribution of tracks that stop in gap 3, there is a clear difference: muons show a gaussian stopping peak distribution, whereas hadrons occur in a nearly constant tail out to high momentum (see Fig. 5.19). By making a cut of $p_z > 3.0$ GeV/c we may eliminate muons from the gap 3 data and obtain a pure sample of hadrons.

To find how the punchthrough background affects the e$-\mu$ analysis, hadrons in gap 3 were isolated and then correlated with electrons. The hadrons were taken from the MuID LL1 M1D dataset, same as the signal e$-\mu$ pairs. Even though a MuID hadron trigger was introduced for Run 8, it did not provide a larger hadron sample than the deep dataset. Furthermore, the deep sample was simpler to use in that it is consistent with the signal data: efficiency corrections for both datasets are the same. Mixed event distributions were created similarly to those used for the signal (Sec. 5.3.2), except only muons with a last hit in Gap 3 of the MuID were used. Fully corrected distributions for opposite sign, like sign, and like sign subtracted punchthroughs were generated (Fig. 5.20).

In estimating the punchthrough distribution in gap 4 from the distribution in gap 3, a couple corrections had to be made:

- The yield due to punchthroughs is expected to be significantly higher in gap 4 than in gap 3. While this might seem counterintuitive (these hadrons must have passed through one more absorber layer), this is because gap 4 is the last gap, and the last measurement made of the tracks. Tracks with last gap=3 have definitely stopped in gap 3, whereas tracks with last gap=4 may have stopped in gap 4 or may not have stopped at all. Simulations using the software "FLUKA" and "GHEISHA" run for the single muon analysis indicate that for every hadron that has a last gap value of 3, 2.81 ± 0.3 hadrons have last gap=4 [102]. This factor is used to scale up the punchthrough distributions.

- By placing the $p_z > 3.0$ cut on tracks we have rejected all hadrons with a momentum of less than this. By fitting the hadron distribution in gap 3 and extrapolating it to $2.0 < p_z < 3.0$ GeV/c we find that we must scale the distribution up by a factor of 1.3 to reflect the total amount of hadrons in our inclusive sample. Only muons with $p_z > 2.0$ GeV/c are measured in the muon detectors.

The punchthrough distributions for Runs 6 and 8 are shown in figures 5.20, 5.21, 5.22, and 5.23. The linear fit values are shown in Table 5.7. No punchthrough background is subtracted for the Run 6 south distribution, the distribution being

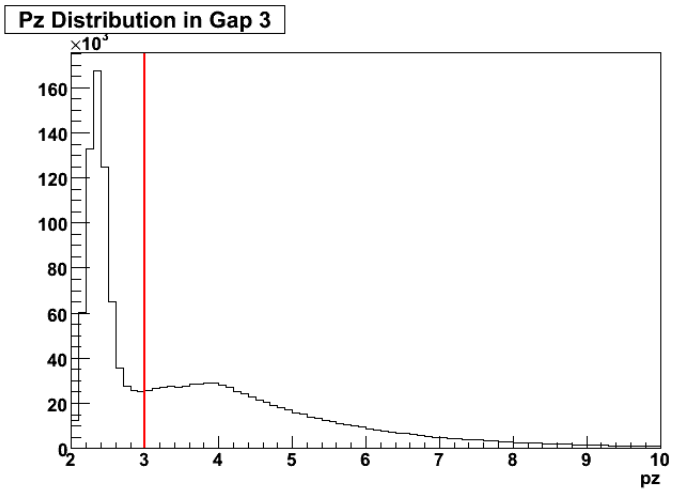

Figure 5.19: p_z distribution of tracks stopping in gap 3 of the MuID, showing the muon stopping peak. Cut on p_z required for punchthroughs is shown as red line.

limited to a small flat level in $\Delta\phi$ (consistent with zero within 2σ). However, the Run 6 north distribution shows a non-zero punchthrough contribution, and therefore the flat line fit to the background is subtracted from the inclusive. Also the punchthrough background in the Run 8 north arm data is non-negligible, fitting a wrapped gaussian of height $7.59 \times 10^{-8} \pm 4.47 \times 10^{-8}$ and width 0.38 ± 0.24, plus a flat line, $1.04 \times 10^{-10} \pm 1.18 \times 10^{-8}$. This fit yields a p value of 0.24 and χ^2/NDF= 26.27/22, compared with a flat line fit yielding a p value of 0.16 and χ^2/NDF= 30.93/24. The gaussian fit was then subtracted from the inclusive signal distribution, and the errors were found using the covariance matrix of the fit (as outlined in Sec. 5.8.1).

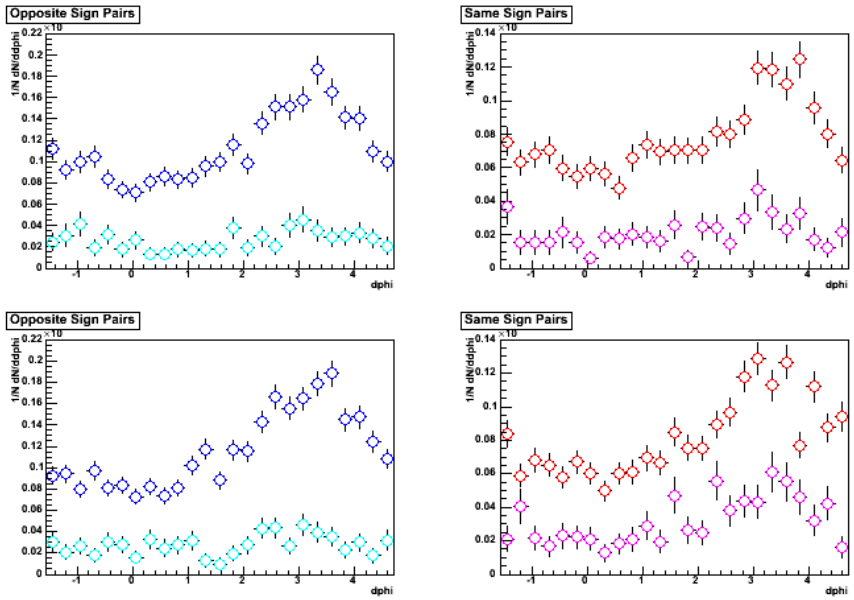

Figure 5.20: Run 6 punchthrough distributions vs. inclusive for opposite sign north (top left), same sign north (top right), opposite sign south (bottom left), and same sign south (bottom right). The punchthrough distributions are shown in cyan (opposite) and magenta (same).

Table 5.7: Punchthrough Background Linear Fit Values

Run and Arm	Value	Error
Run 6 North	4.60 $\times 10^{-9}$	2.17 $\times 10^{-9}$
Run 6 South	-2.53 $\times 10^{-9}$	2.24 $\times 10^{-9}$

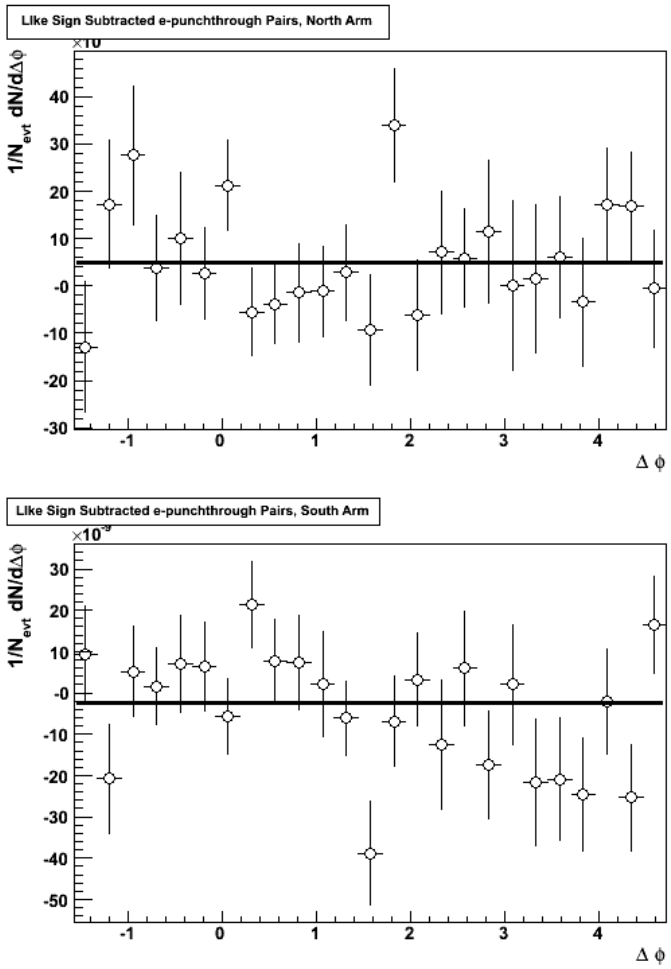

Figure 5.21: Punchthrough like sign subtracted distributions for north (top) and south (bottom) arm in Run 6. The north arm distribution is fit to a flat line of $4.5 \times 10^{-9} \pm 2.17 \times 10^{-9}$, and the south arm distribution fits a line of $-2.53 \times 10^{-9} \pm 2.24 \times 10^{-9}$.

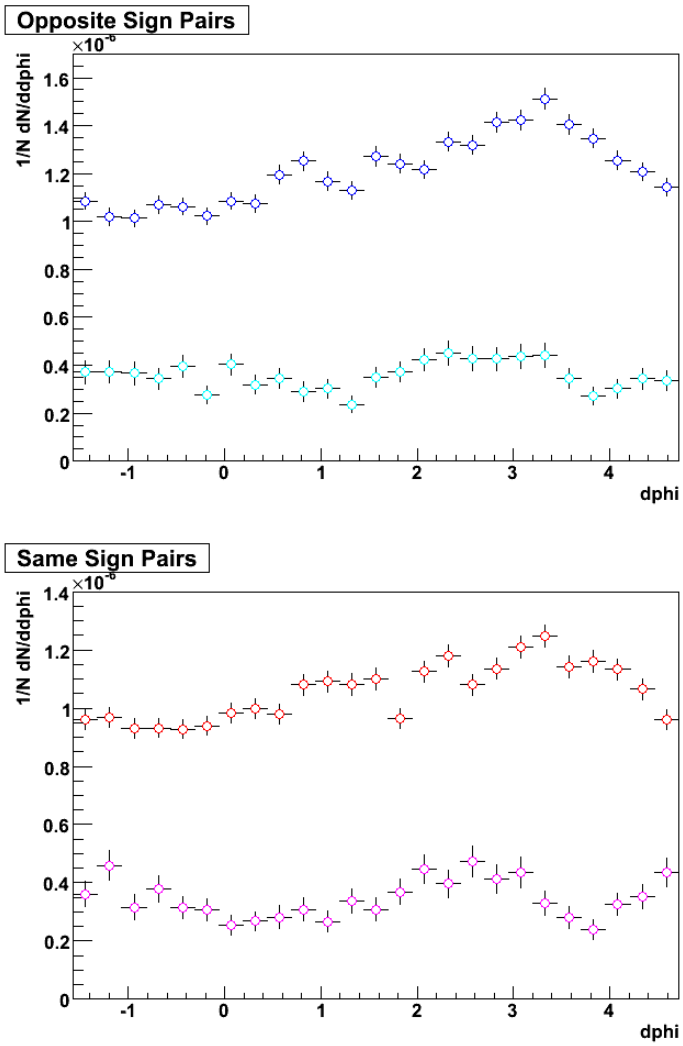

Figure 5.22: Punchthrough distributions for opposite sign (top) and same sign (bottom) for Run 8, north arm. Inclusive distributions included for comparison. Punchthrough distributions shown in cyan (opposite) and magenta (same)

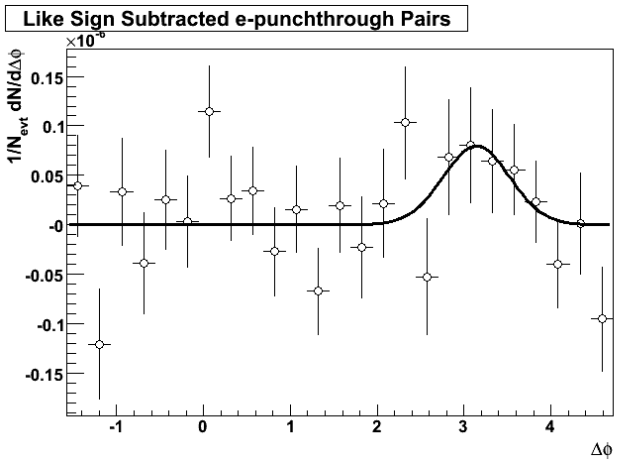

Figure 5.23: Punchthrough like sign subtracted distribution for Run 8 north arm. The distribution is fit to a wrapped gaussian of $\sigma = 0.381$ and height $= 7.59 \times 10^{-8}$ plus a flat of value 1.045×10^{-10}.

5.6.3 Photonic Electron Background

The measurement of electrons by PHENIX is in general much cleaner than the measurement of muons. There is almost no possibility of hadron contamination of the electron sample thanks to detectors such as the RICH and the EMCal. Also there is no equivalent to the decay muon background for electrons, since the primary charged D decay products ($\pi^{\pm}$, $K^{\pm}$) decay to muons at a much higher rate than they decay to electrons.

A major background affecting single electron measurements is due to photonic electrons. These electrons come predominantly from π^0 decay, through either $\pi^0 \to \gamma\gamma$ where one γ converts to an electron, or though $\pi^0 \to e^+e^-\gamma$ where one of the electrons is detected. Because photonic electrons result from the

decay of a neutral particle, there is no reason to believe they would be charge-correlated with a muon, even if they shared a charm pair ancestor. As a check of the method, though, we went on to evaluate this background to confirm there is no contribution.

Photonic electrons may often be associated with photons of $p_T > 0.4$, and the invariant mass of these pairs will show a peak at the π^0 mass. This is evident in Fig 5.24. The $e-\gamma$ π^0 peak was fit to a gaussian distribution. All electrons in the e$-\mu$ sample that were associated with a photon and fell within a $\pm 2\sigma$ range of the mean of the gaussian fit were considered to be photonic electrons. These photonic electrons were then correlated with muons to yield a background $\Delta\phi$ distribution. However, a large number of these electrons were most likely not from π^0 decay, but only fell within the mass peak due to combinatorics. Some of these combinatoric electrons may even be heavy flavor electrons. To remove the heavy flavor signal, we first fit the mass distribution to a gaussian plus a polynomial, to model both the photonic signal and the combinatoric background. This allowed us to find the ratio of the signal to background under the π^0 peak. Then an estimate of the combinatoric $\Delta\phi$ distribution was found by looking at e$-\mu$ pairs where the electron coincides with a photon, but their mass is above the range of the π^0 peak: we used a range of 0.2$-$0.4 GeV/c. The $\Delta\phi$ distribution for these pairs was subtracted from the photonic signal electron $\Delta\phi$ distribution after scaling by the ratio of background to signal. The resultant distributions for Run 6 are shown in

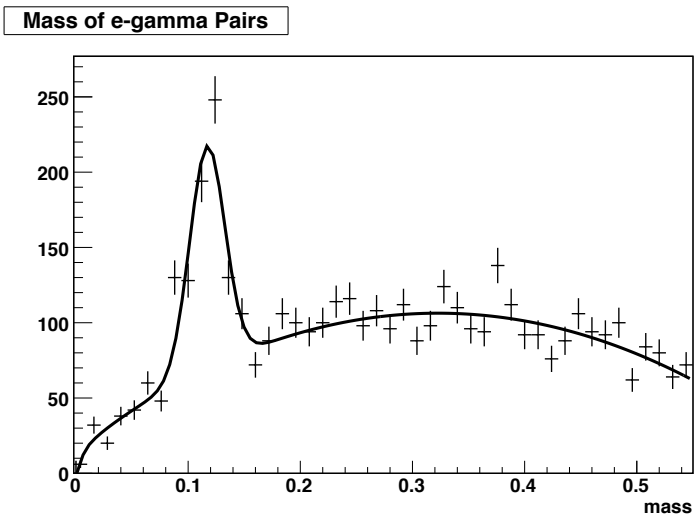

Figure 5.24: Invariant mass in GeV/c^2 of $e-\gamma$ pairs, showing gaussian fit to π^0 peak plus polynomial fit to background.

Fig. 5.25. The flat line fits are consistent with zero within 2σ, thus showing this to be an insignificant background as we expected.

5.6.4 Background Subtraction Summary

Only the backgrounds that contributed to the $\Delta\phi$ distribution at a non-zero level were subtracted. The backgrounds that were found consistent with zero did, however, have a systematic uncertainty assigned to them. The sole background that fit a flat line (Run 6 north punchthrough) was removed by subtracting the linear fit function from the signal distribution. The Run 8 punchthrough background, which fit a gaussian, was removed by subtracting

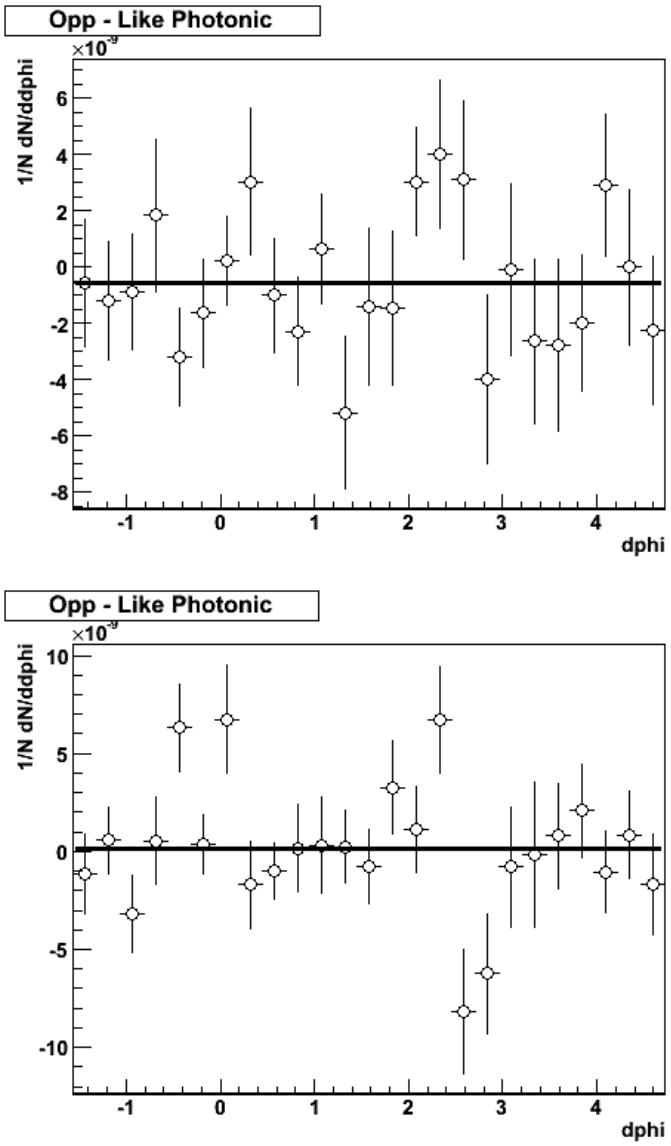

Figure 5.25: Photonic $\Delta\phi$ distributions for photonic electrons with north arm muons (top) and south arm muons (bottom). The north distribution fits a line of $-5.43 \times 10^{-10} \pm 4.61 \times 10^{-10}$ and the south distribution fits a line of $1.70 \times 10^{-10} \pm 4.37 \times 10^{-10}$, both of which are consistent with 0 given the very low statistics.

that fit gaussian from the signal, and errors were propagated accordingly.

We must note one subtraction which we did not do, which is a ZYAM (zero yield at minimum) subtraction [103]. It is common practice in RHIC dihadron analyses to define the lowest point in the azimuthal correlation to be the point of zero jet yield. The pedestal on which the distribution sits is then subtracted off, shifting the entire distribution downward. This procedure is used to remove background from the underlying event. In the e$-\mu$ analysis, though, we have already subtracted off the background with the like sign subtraction, as well as the additional sources described above. Therefore, even though the final distribution shows a large pedestal in addition to the peak at π, this is part of the signal of e$-\mu$ from charm. This pedestal is predicted from NLO charm production (see Sec. 6.3.1).

5.7 Consistency Checks

5.7.1 Run 8 p+p Comparison

Ideally, processes in p+p and d+Au collisions would be compared against each other under exactly the same detector configuration. This is generally possible if the different collision systems are run in the same year, as upgrades are made and new detectors are installed during the summer breaks between runs. With this in mind it was decided that a p+p run would take place immediately after

the Run 8 d+Au run, and the number of events recorded was comparable to that recorded during Run 6. Unfortunately, though, many fewer e$-\mu$ events were recorded due to a change in the muon triggers. Rather than separate north and south 1-deep triggers that had been used previously, these two triggers were AND-ed and given new, larger scaledown factors. This means that effectively the e$-\mu$ sample from Run 8 p+p is only about a third the size of that of the Run 6 p+p dataset.

Though it is not a direct contribution to the p+p analysis, the Run 8 dataset it still useful as a cross check on the e$-\mu$ consistency between runs. It is necessary to see that we have properly corrected for the structural changes between runs, for example the addition of the HBD support structure that has caused high backgrounds for electrons. The results of this comparison can be seen in Fig. 5.26. The like sign subtracted distributions agree within errors, though there is a small difference between the like sign and opposite sign distributions on their own. This is not a cause for alarm, because the inclusive distributions include many backgrounds that are removed with the like sign subtractions, and these backgrounds may differ with different detector conditions. Furthermore the difference is reduced when systematic errors are taken into account.

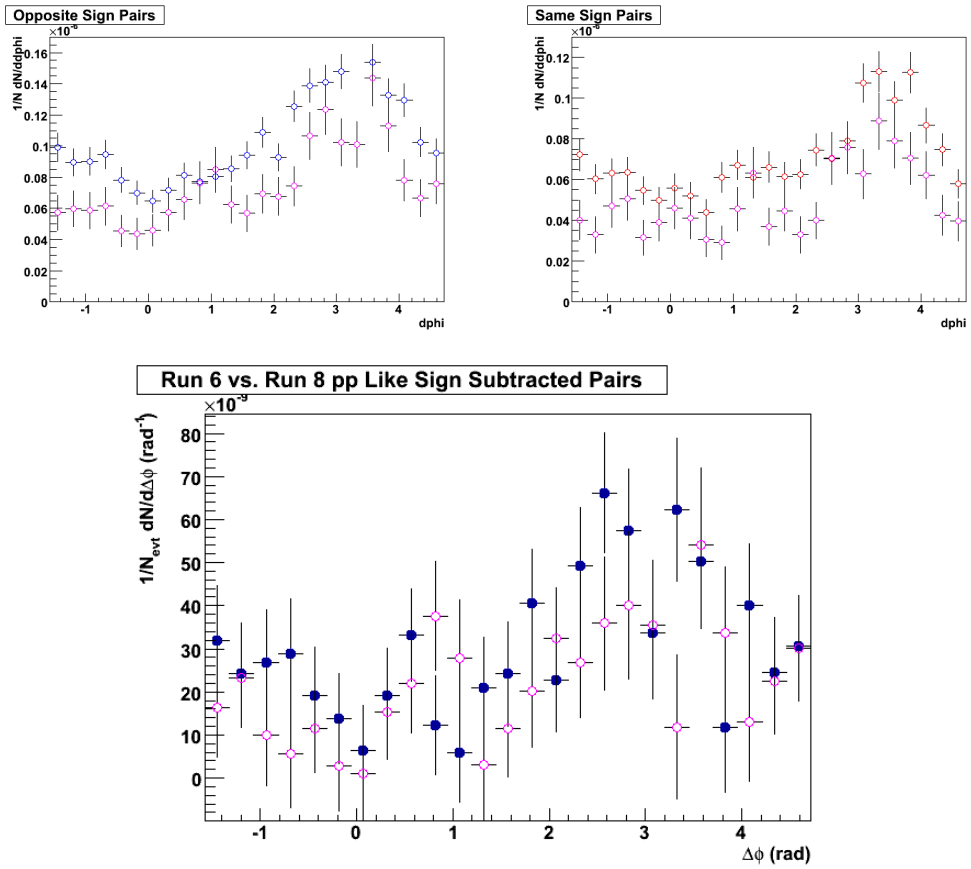

Figure 5.26: Run 6 p+p vs. Run 8 p+p north arm distributions for opposite sign (left) and same sign (right) pairs. The Run 8 data are in magenta on each plot. Below, comparison of like sign subtracted and background subtracted Run 6 p+p distribution (black) vs. Run 8 p+p distribution (magenta).

5.7.2 Pythia Comparison

The final e$-\mu$ distributions were also compared with those created using Pythia simulations, with the settings described in Appendix B. An exact match is not expected, since Pythia does not simulate higher order charm production processes to high accuracy. Nevertheless, the distributions match well in the peak region (Fig. 5.27). The mismatch on the near side (the plateau in the data) is most likely due to the contribution from higher order corrections. Simulations using POWHEG more closely match the data (see Sec. 6.3.1).

5.8 Systematic Errors

Systematic errors on PHENIX data come in three varieties: Type A, uncorrelated point-to-point errors; Type B, correlated point-to-point errors; and Type C, errors on the absolute normalization [104]. As long as these types are each uncorrelated, a total systematic uncertainty may be found from their magnitude:

$$\sigma^{syst} = \sqrt{(\sigma^{systA})^2 + (\sigma^{systB})^2 + (\sigma^{systC})^2} \tag{5.10}$$

and then the total uncertainty is:

$$\sigma = \sqrt{(\sigma^{stat})^2 + (\sigma^{syst})^2} \tag{5.11}$$

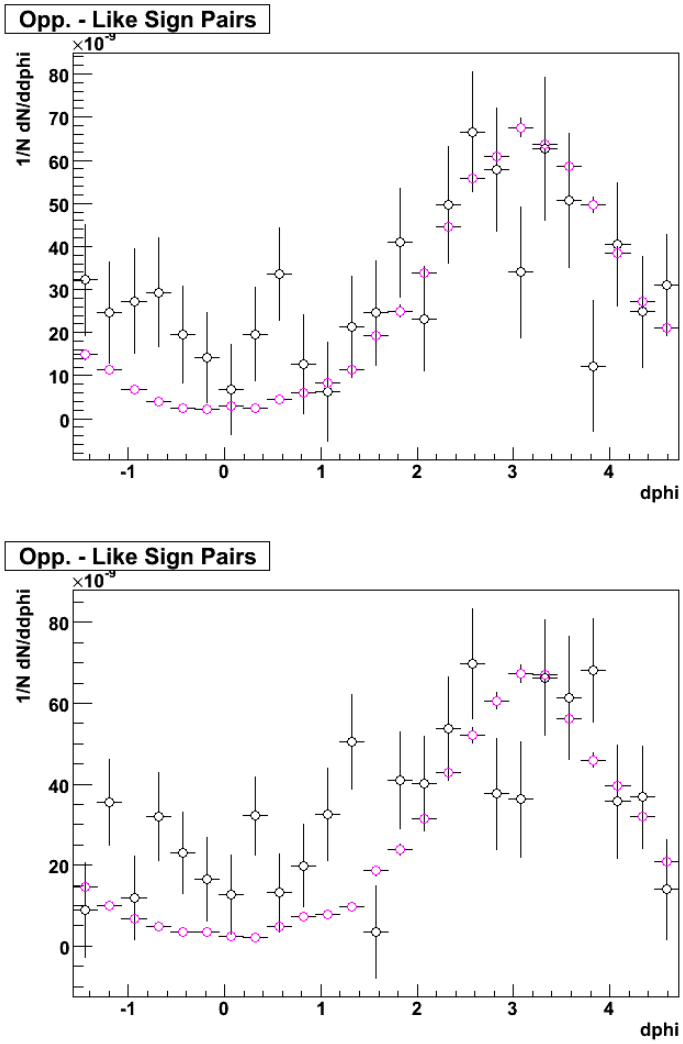

Figure 5.27: Run 6 p+p data (black) vs. Pythia simulated (magenta) e$-\mu$ pairs as a function of $\Delta\phi$ for north arm (top) and south arm (bottom).

The following is a summary of all of the different sources of systematic errors in the e$-\mu$ measurement.

5.8.1 Background Subtraction Uncertainty

Two types of backgrounds factor into the subtraction uncertainty: punchthrough hadrons and decay muons. The uncertainty must be found for the decay muons even though they are effectively not subtracted (they fit a flat line consistent with zero) because there is a plausible reason why they might contribute to the signal. It is possible to have charge correlated e$-\mu$ pairs from decays if the muon is still part of the charm decay chain. For example, a D might decay to a K, which then decays to a pion plus a muon. We only know that this is a zero contribution because we have measured it. This is in contrast to our measurement of the photonic electron background, which we never expected to contribute to the signal. Photonic electrons are produced in pairs (from π^0 decay or from $\gamma \rightarrow e^+e^-$), which means they lose the charge correlation with the muon even if they are in the charm decay chain. They could only contribute to the signal if we had made an error in the analysis or had not properly corrected for detector effects (which was not the case). Therefore to include the error on the photonic background would be an overestimate of the total error.

For the backgrounds that fit flat lines, we take the systematic uncertainty to

Table 5.8: Total Linear Fit Errors

Run and Arm	Error Value	$\Delta\phi$ integrated error
Run 6 North	1.15×10^{-8}	7.23×10^{-8}
Run 6 South	1.07×10^{-8}	6.72×10^{-8}
Run 8 North	4.30×10^{-8}	2.70×10^{-7}

be the error of the fit to those lines. If the fit is a flat line consistent with zero, then each point can be thought of as an independent measure of zero. Then the standard deviation of this measurement is equal to the error on the flat line fit. The overall combined linear background errors (decay and punchthrough have been summed in quadrature) are shown in Table 5.8. These are classified as Type C uncertainties, since they affect the overall normalization of the results.

The error on the gaussian punchthrough subtraction for Run 8 must be handled separately. The covariance matrix for the fit was found, it was used in error propagation via the equation:

$$\sigma^2 = \begin{bmatrix} \frac{\partial f}{\partial a} & \frac{\partial f}{\partial b} \end{bmatrix} \begin{bmatrix} \sigma_a^2 & \sigma_{ab} \\ \sigma_{ba} & \sigma_b^2 \end{bmatrix} \begin{bmatrix} \frac{\partial f}{\partial a} \\ \frac{\partial f}{\partial b} \end{bmatrix} \tag{5.12}$$

where f is the fit function and a and b are the parameters used in the fit. The derivatives of the fit with respect to the parameters were evaluated at each $\Delta\phi$ bin, giving a σ for each bin. The fit function used is

$$f = \frac{a}{b\sqrt{2\pi}} e^{\frac{-(\Delta\phi-\pi)^2}{2b^2}} \tag{5.13}$$

Because these bin-by-bin errors are uncorrelated, they are classified as Type A.

5.8.2 Particle ID and Fiducial Cuts Uncertainty

There is uncertainty regarding the efficiency of the particle ID cuts, in that we do not know exactly how many real electrons and muons each cut removes and how much background they let in. This is a Type B error, because while it will not affect each point on the $\Delta\phi$ histogram individually, it also will not shift the entire distribution up or down by a normalization factor. This uncertainty was quantified by measuring the effect of tightening each cut. The acc×eff was recalculated for each tightened cut, and the new pair yield was measured and compared with the old. If the yield stays the same, this implies that the tightened cut only cuts out more real electrons or muons, which the acc×eff corrects for. However if this yield varies, the old cut still let some background in. The change in yield is a measure of how effective the cut is. This technique is used for both the particle ID cuts as well as the fiducial cuts. Included is a table giving the percentage change in yield upon tightening various cuts.

If each of the particle ID errors was uncorrelated, we could simply add them in quadrature for the total systematic. As seen in Table 4.2, however, the muon variables are not entirely independent of each other. For this reason the systematic error associated with the muon road and track cuts was evaluated

Table 5.9: Muon Variable Systematic Error

Cut	Percentage Change in Yield
Correlated DG0, DDG0, refrad, p$\delta\theta$, slope north	4.44%
Correlated DG0, DDG0, refrad, p$\delta\theta$, slope south	5.13 %
MuTR matching Run 6 north	6.38%
MuTR matching Run 6 south	2.86 %
MuTR matching Run 8 north	7.0%

Table 5.10: Electron Variable Systematic Error

Cut	Percentage Change in Yield
Correlated n0, n1	5.11%
emc matching	2.70%
dep Run 6	3.11 %
dep Run 8	5.28%
DC ϕ fiducial	4.97%
DC ϕ fiducial Run 8 cuts	0.51%
prob	0.95%

using a full error matrix, using the covariances of each pair. The resulting systematic error is lower than that obtained assuming independence. The same is true for two of the electron variables, n_0 and n_1. These have a $\mathcal{C}$ value of 0.765, since they are essentially measuring the same thing. The error for this pair combined was found taking the correlation into account. In general, the cut variables are independent of each other if they involve different detectors or different measurement aspects of the same detector; otherwise the correlation needs to be accounted for.

The systematic errors found from tightening cuts were generally found to agree

between Run 6 and Run 8 when the same cuts were used for both runs. In the few cases in which the cuts changed, the errors needed to be reevaluated. For example, an additional error was assigned to the fiducial cuts placed to remove HBD conversion electrons and the PC1 dead area in Run 8. Also, the cut on *dep* changed between runs, and had to be reevaluated. This poses some difficulty in comparing the datasets, for example in the ratio used to find R_{dA}. The errors that are the same for each run are of course 100% correlated, and the errors that correspond to a new cut are completely uncorrelated (such as the HBD fiducial cuts). In the case of the dep cut, which is similar for the run groups but slightly altered, we approximate the error to be 50% correlated and 50% uncorrelated. In taking the R_{dA} ratio, as described in the next chapter, systematic errors that are identical between the Run 6 and the Run 8 datasets cancel.

5.8.3 MuTR Efficiency Systematic Uncertainty

In order to evaluate the systematic effect of dead and hot areas in the MuTR, we compared the ϕ distributions of the data versus PISA. For this comparison the Monte Carlo was weighted according to the p_T spectrum used to weight the PISA for the acc×eff correction. An overlay of data with PISA for the MuTR ϕ distribution in the north arm is shown in Fig. 5.28 for Run 6 and Figs. 5.4 and 5.5 for Run 8. The data was normalized to the integral of the Monte Carlo, and the difference between the integral of the data and the Monte Carlo

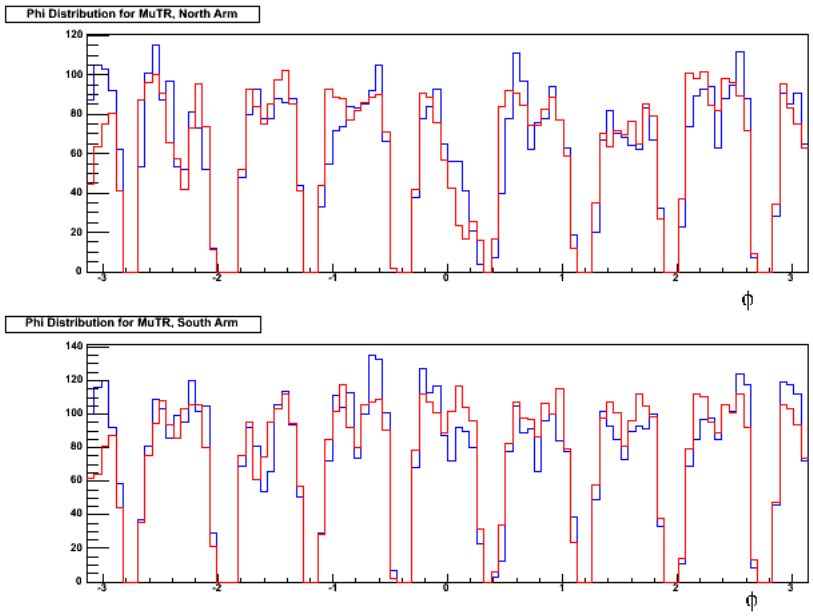

Figure 5.28: MuTR ϕ distribution in radians for data vs. MC for Run 6 north arm (top) and south arm (bottom). Data is in blue and MC is in red.

was measured for each octant. The overall percentage differences are given in Tab. 5.9, and these are used for the Type B systematic error on the matching of data to Monte Carlo in the MuTR.

5.8.4 Systematic Uncertainty on Trigger Efficiencies

The datasets used in this analysis was selected using the MuID LL1 North and South Deep triggers. The efficiencies for these triggers to fire on a muon stopping in either gap 3 or gap 4 of the MuID was used to correct the e$-\mu$ spectrum. The uncertainty on these efficiencies was measured by finding their variation with respect to different run groups. Efficiencies were calculated

Table 5.11: Trigger Efficiency Systematic Error

Dataset	Trigger Efficiency Uncertainty
Run 6 pp	3.0%
Run 8 dAu gap 4	1.67%
Run 8 dAu gap 3	2.38 %

separately for 20 different run groups for Run 6, but for only 5 different groups for Run 8 (due to very little variation being found). The total uncertainties are shown in Table 5.11.

5.8.5 Systematic Uncertainty on PISA eff×acc Calculation

The single particle acc×eff values were calculated using a PISA simulation of single electrons and muons. The particles were thrown with a flat distribution in p_T, and were then weighted before analysis with a realistic p_T spectrum (taken from the measured PHENIX heavy lepton spectra). In order to study the uncertainty due to the eff×acc corrections, the difference was found between the values from the p_T weighted leptons and those without the weighting applied. This difference was found to be 2.0% for muons and 1.6% for electrons. However, this is too large as a measure of systematic uncertainty, because this assumes the weighting function used is wrong by a maximal amount. For a more realistic measure of the uncertainty, we use half of these values: 1.0% for muons and 0.8% for electrons.

Table 5.12: Total Summed Type B Errors

Dataset	Total Type B Uncertainty
Run 6 pp north	11.99%
Run 6 pp south	10.62%
Run 8 dAu north	12.81 %

5.8.6 Systematic Uncertainty on Run to Run Uncertainty

Another source of systematic uncertainty comes from the run to run variation in muon yields and electron yields. Because the acc×eff corrections are usually only calculated for one run, the corrections for subsequent runs may be slightly wrong due to variations in acceptance. To measure this, the octant by octant yield in the MuTR was examined as a function of run group. A variation in yield of not more than 2% was found. Because this coincides with previous measures of run to run variations using J/Ψ yields, we used this as the systematic uncertainty.

5.8.7 Total Type B Uncertainty

All uncertainties unrelated to background subtraction are Type B uncertainties, and were added in quadrature for each dataset analyzed. The resulting error is found in Table 5.12.

5.8.8 Effect of Mean η Shift on Yield

Differences in dead regions in the MuTR and MuID do more than simply reduce the number of pairs observed: they can slightly shift the physics. Because the muon detectors cover the forward region, asymmetrical dead areas can effectively shift the mean η at which muons are found, and therefore the mean η of e-μ pairs. The pairs will then correspond to charm production in a slightly different kinematic region, and because both production and suppression depend on the rapidity this could lead to observational effects.

Ideally, the mean η for both datasets and also for the Pythia simulations would be the same. In reality there are slight differences though, as shown in Tab. 5.13. Based on Pythia simulations, the yield differences for different mean η values were also calculated. A realistic η spectrum was modeled, and the differences in yield at the mean η of each of the datasets were found. This differences happened to be less than 1%. Because of this we do not expect the different mean η values to change the value of R_{dA}. The actual mean η of the measurement is reported with the result. As a sidenote, the mean η of the electrons is almost exactly 0 due to the more symmetric acceptance of the central arms, so in that case this analysis is unnecessary.

Table 5.13: Mean $|\eta|$ Values for Datasets

Dataset	Mean $\|\eta\|$	Percentage Change in Yield
Pythia north	1.732	
Run 6 north	1.746	-0.622%
Run 8 north	1.749	-0.758%
Pythia south	1.732	
Run 6 south	1.727	0.216%

Chapter 6

Results and Discussion

6.1 Final Heavy Flavor e$-\mu$ Correlations

After all corrections are made to both the signal and the background $\Delta\phi$ distributions, each non-zero background distribution is subtracted:

$$\frac{1}{N_{evt}}\frac{dN^{e^q\mu_a^Q}}{d\Delta\phi} = \frac{\int \Delta\phi\ \mathrm{Mix}_{q,Q,a}\left(\Delta\phi\right)}{2\pi\epsilon_e\epsilon_\mu^{Q,a}N_{evt}}\frac{\mathrm{Real}_{q,Q,a}\left(\Delta\phi\right)}{\mathrm{Mix}_{q,Q,a}\left(\Delta\phi\right)} - \frac{\int \Delta\phi\ \mathrm{Mix}^p_{q,Q,a}\left(\Delta\phi\right)}{2\pi\epsilon_e\epsilon_\mu^{Q,a,p}N_{evt}}\frac{\mathrm{Real}^p_{q,Q,a}\left(\Delta\phi\right)}{\mathrm{Mix}^p_{q,Q,a}\left(\Delta\phi\right)} \tag{6.1}$$

where ϵ_e is the electron acceptance$\times$efficiency and $\epsilon_\mu^{Q,a}$ is the charge- and arm-

dependent muon acceptance×efficiency. The quantities with "p" superscripts are those distributions and efficiencies for punchthrough hadrons. The subtracted e$-\mu$ distributions, including systematic errors, are shown in Figs. 6.1, 6.2, 6.3, and 6.4. The distributions are fit with wrapped gaussian functions with a linear offset, of the form

$$f_{gaus}(x) = C + \frac{A}{\sigma\sqrt{2\pi}} e^{\frac{(x-\pi)^2}{2\sigma^2}} \tag{6.2}$$

A list of the fit parameters and their uncertainties is given in Tab. 6.1. North and south Run 6 distributions are consistent with each other. The Run 8 distribution is not obviously a gaussian, and in fact fits a flat line equally well (p values of 0.23 for the gaussian and 0.26 for a line). For the gaussian fit, the error on σ was found first assuming a symmetrical error, then relaxing that assumption. The symmetrical error is shown in Table 6.1. The asymmetrical error was found to be $+0.921$ -0.640.

A comparison of Run 6 p+p vs. Run 8 d+Au is shown in Fig. 6.5. In order to compare the two datasets, the Run 8 distribution is scaled by N_{coll}, the number of binary collisions in minimum bias d+Au collisions. This is the factor by which hard processes are expected to scale in heavy ion collisions, in the absence of medium-induced and other effects. The value of N_{coll} for the d+Au dataset was found to be 7.59 [105].

Table 6.1: Fit parameter values, with their errors, for each dataset. Both a gaussian fit and a flat line fit to the Run 8 north dataset are shown.

Dataset	C	C err	σ	σ err	A	A err
Run 6 p+p north	1.77×10^{-8}	5.10×10^{-9}	0.921	0.318	7.84×10^{-8}	3.01×10^{-8}
Run 6 p+p south	2.29×10^{-8}	3.88×10^{-9}	0.883	0.195	8.58×10^{-8}	2.26×10^{-8}
Run 8 d+Au north	1.05×10^{-7}	1.77×10^{-8}	0.968	0.840	8.53×10^{-8}	9.92×10^{-8}
Run 8 d+Au flat	1.17×10^{-7}	9.33×10^{-9}				

One may wonder if a more detailed study of e$-\mu$ pairs may have been done by breaking up the distributions into bins in p_T and centrality (a measure of how head-on the collision is). While this may have helped to better illustrate the influence of cold nuclear matter effects on the d+Au distributions, the statistics proved to be too low to extract much information from binned data. For this reason an inclusive distribution was decided on as the final result.

6.2 Calculating the Cross Section and R_{dA}

6.2.1 Derivation of Measured Quantities

A useful measure of a rare process in particle collisions is given by the cross section. It has dimensions of area and is often given in units known as "barns", which are defined as 1 barn = 10^{-28} m^2. The cross section is related to the likelihood that a scattering process will occur. The total inelastic cross section of a proton-proton collision at $\sqrt{s} = 200$ GeV is approximately 42 mb.

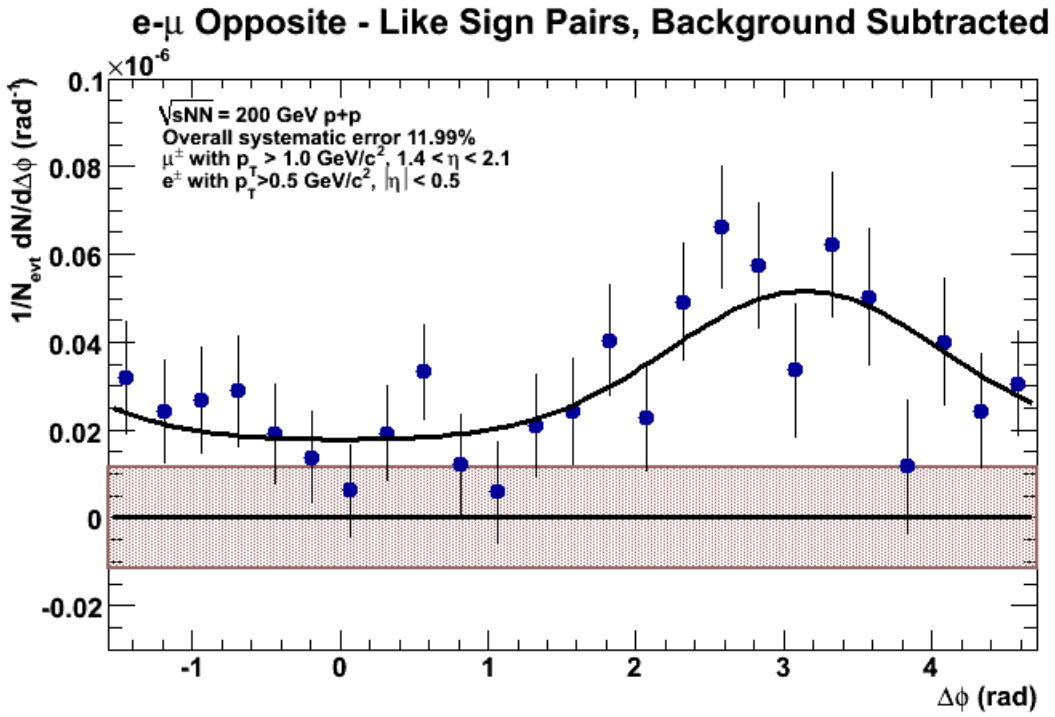

Figure 6.1: Background subtracted Run 6 north arm e$-\mu$ pairs. Data is from p+p collisions at 200 GeV. The kinematic range used is electron $p_T > 0.5$, muon $p_T > 1.0$, electron rapidity between $-0.5 < \eta < 0.5$ and muon rapidity between $1.4 < \eta < 2.1$. Error bars show only statistical error. The combination of punchthrough and decay muon systematic error shown with filled box. The other systematic errors combined give an overall error of 11.99%. Gaussian fit gives $\sigma = 0.921 \pm 0.318$.

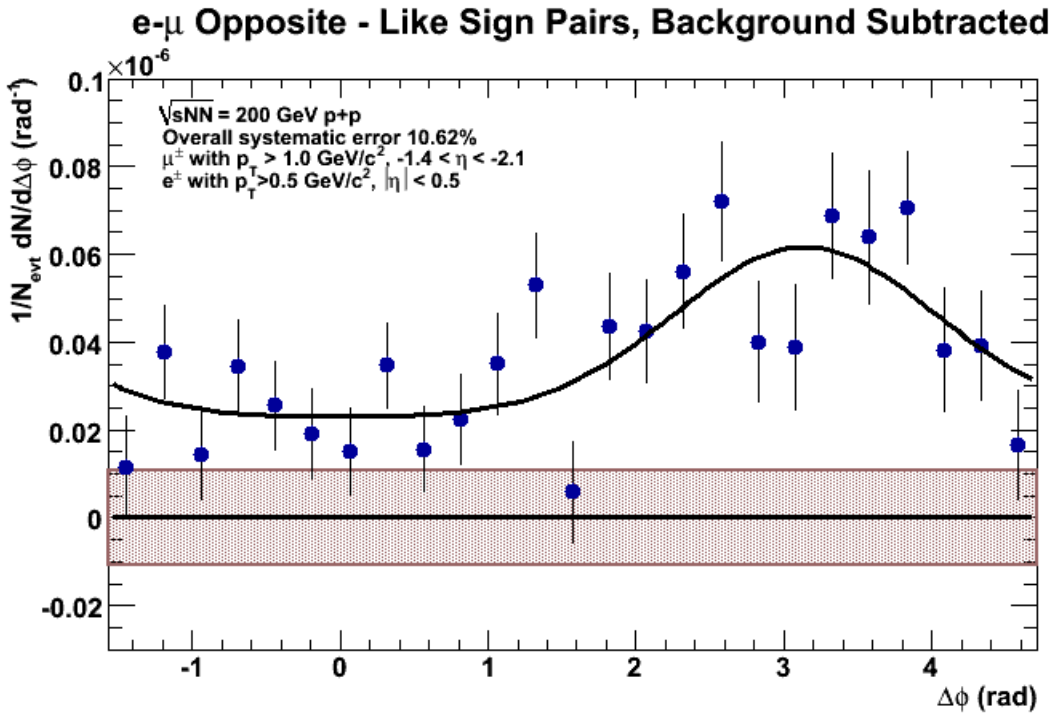

Figure 6.2: Background subtracted Run 6 south arm e$-\mu$ pairs. Data is from p+p collisions at 200 GeV. The kinematic range used is electron $p_T > 0.5$, muon $p_T > 1.0$, electron rapidity between $-0.5 < \eta < 0.5$ and muon rapidity between $-2.1 < \eta < -1.4$. Error bars show only statistical error. The combination of punchthrough and decay muon systematic error shown with filled box. The other systematic errors combined give an overall error of 10.62%. Gaussian fit gives $\sigma = 0.883 \pm 0.195$.

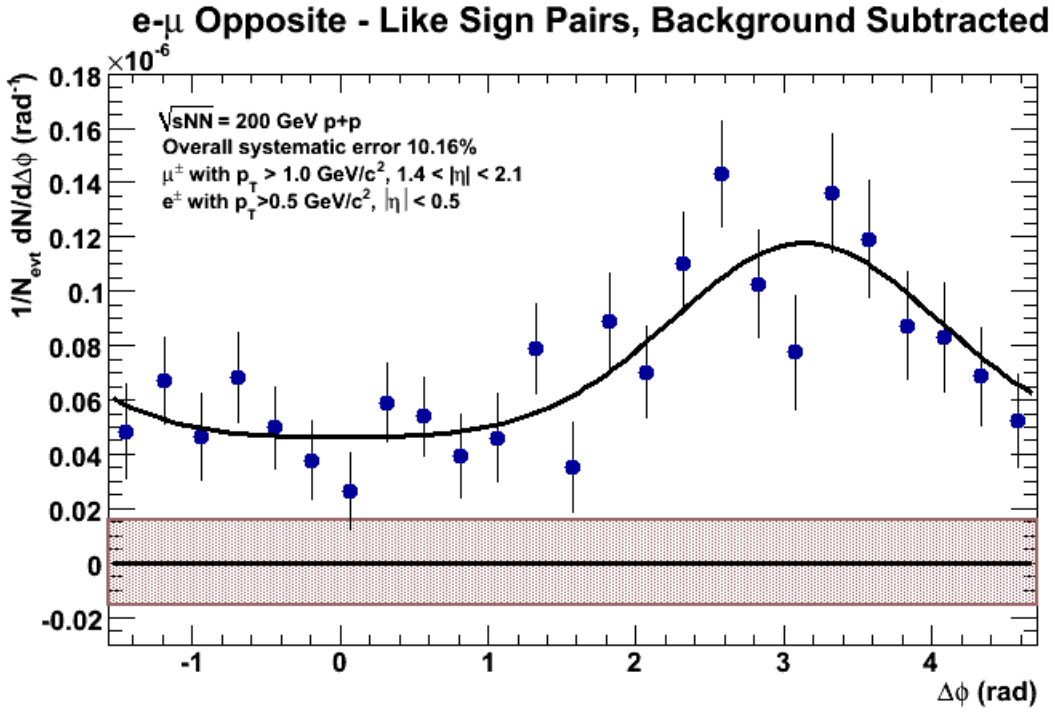

Figure 6.3: Background subtracted Run 6 north+south arm e$-\mu$ pairs. Data is from p+p collisions at 200 GeV. The kinematic range used is electron $p_T > 0.5$, muon $p_T > 1.0$, electron rapidity between $-0.5 < \eta < 0.5$ and muon rapidity between $-2.1 < |\eta| < -1.4$. Error bars show only statistical error. The combination of punchthrough and decay muon systematic error shown with filled box. The other systematic errors combined give an overall error of 10.16%. Gaussian fit gives $\sigma = 0.897 \pm 0.177$.

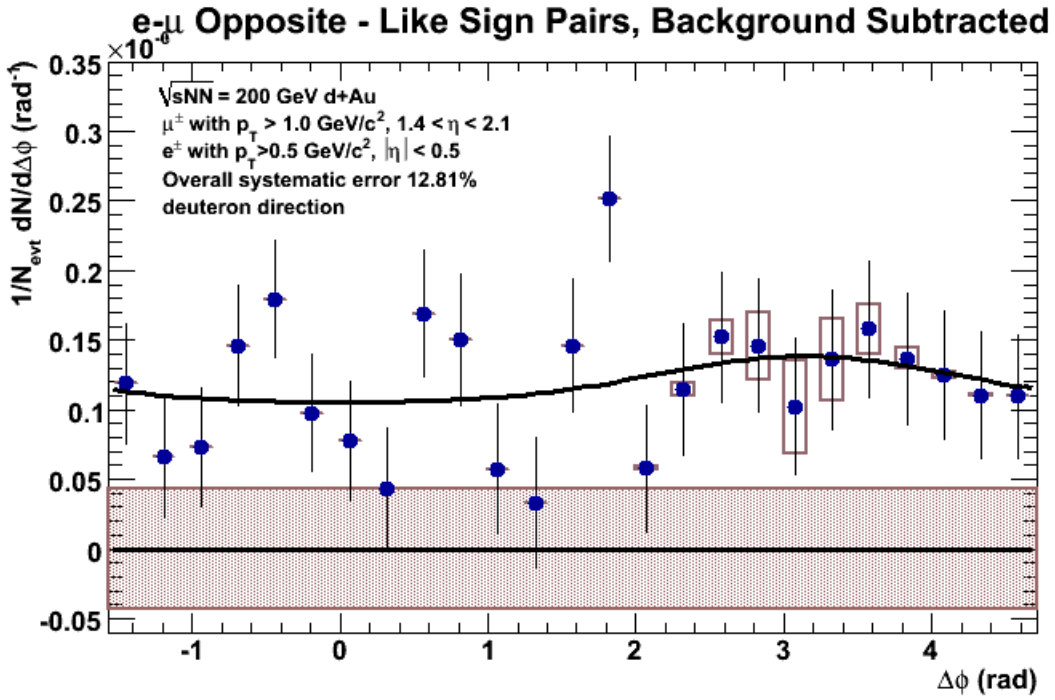

Figure 6.4: Background subtracted Run 8 north arm e$-\mu$ pairs. Data is from d+Au collisions at 200 GeV. The kinematic range used is electron $p_T > 0.5$, muon $p_T > 1.0$, electron rapidity between $-0.5 < \eta < 0.5$ and muon rapidity between $1.4 < \eta < 2.1$. Error bars show only statistical error. Linear background systematic error shown with filled box, gaussian punchthrough subtraction error shown with empty boxes. Other systematic errors combine to give an overall error of 12.81%.

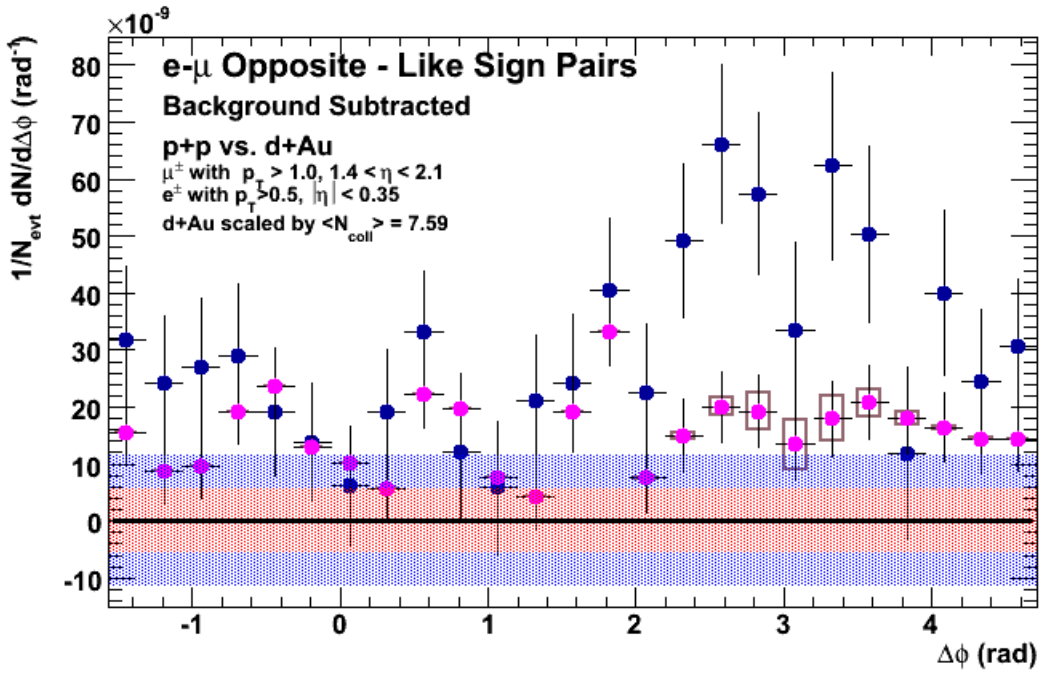

Figure 6.5: Run 6 north (blue) vs. Run 8 north (magenta) scaled by $N_{coll} = 7.59$. Systematic subtraction error for Run 6 is shown by blue band, error for Run 8 by red band. Empty boxes show punchthrough subtraction error on the d+Au, error bars are statistical errors.

In order to find the cross section for interaction processes, we must know a quantity called the luminosity, which is the number of interacting particles per unit area per unit time. It is related to the cross section by

$$\frac{dN^X}{dt} = \mathcal{L}\sigma^X \tag{6.3}$$

Where $\frac{dN^X}{dt}$ is the scattering event rate for process X, $\mathcal{L}$ is the luminosity, and σ is the cross section for process X. This can also be written as

$$\sigma^X = \frac{N^X}{\hat{\mathcal{L}}} \tag{6.4}$$

Where $\hat{\mathcal{L}}$ is the time-integrated luminosity, in units of [cm^{-2}]. The integrated luminosity is calculated by RHIC for the given run period. However, PHENIX does not see all of this luminosity due to inefficiencies in the detector response. The effective luminosity that PHENIX sees is

$$\hat{\mathcal{L}_{\text{eff}}} = \frac{N^{tot}_{BBC}}{\sigma_{BBC}} \tag{6.5}$$

Where N^{tot}_{BBC} is the total number of events recorded to the BBC, and σ_{BBC} is the BBC cross section. For Run 6, the BBC cross section was 23 ± 2.3 mb. Thus, to find the cross section of e$-\mu$ pairs as a function of rapidity, we can write,

$$\frac{d\sigma^{e-\mu}_{unbiased}}{dy} = \frac{\sigma_{BBC}}{N^{tot}_{BBC}} \frac{dN^{e-\mu}_{unbiased}}{dy} \tag{6.6}$$

Note, however, that this relation applies only to an unbiased measure of the number of e$-\mu$ pairs as a function of rapidity. In reality we have an unavoidable trigger bias that we must correct for. Up until this point, the number of e$-\mu$ pairs has been corrected for acceptance and efficiency, as well as for the muon trigger efficiency. The muon trigger, though, is ANDed with the BBC LL1 trigger, which ensures that an actual collision took place when the track was detected. Because not all e$-\mu$ tracks fire this trigger, we must account for the fraction that are missed when finding the overall cross section. The BBC efficiency for hard processes is found by calculating the number of hard scattering events that occur with the BBC trigger firing, and dividing by the total number of hard scattering events. Ideally this calculation would be done with heavy flavor muons, however no muon-triggered data was recorded without requiring the BBC. Events with other high p_T particles should cause the BBC to fire a similar fraction of the time. In a study involving high p_T π^0s in Run 6, the BBC LL1 trigger fired for 78% $\pm$ 3% of events, and this is what we'll use for the BBC efficiency ϵ^{BBC}_{hard} [106]. Finally we arrive at the final equation for the cross section,

$$\frac{d\sigma^{e-\mu}}{dy} = \frac{\sigma_{BBC}}{N^{tot}_{BBC}} C^{BBCbias} \frac{dN^{e-\mu}_{biased}}{\Delta y} \tag{6.7}$$

Where $C^{BBCbias} = 1/\epsilon^{BBC}_{hard} = 1.28$ and $\sigma_{BBC} = 23.0 \pm 2.2$mb as determined during Run 3, the latest data available [107], [108].

When analyzing d+Au data it is not usual to determine the cross section. Rather, we measure the deviation from the scaled p+p yields using R_{dA}, which is defined as follows:

$$R_{dAu} = \frac{dN_{dA}}{< T_{dA} > \times d\sigma_{pp}} \tag{6.8}$$

where T_{dA} is the nuclear thickness function for deuteron-gold collisions, N_{dA} is the yield in d+Au, and σ_{pp} is the cross section of the process in p+p collisions [13]. T_{dA} is the factor by which the cross section in p+p is multiplied to give the yield in d+Au, $N^{dA}_{\rm hard} = T_{dA}\sigma^{pp}_{\rm hard}$. The average value of T_{AB} for an arbitrary heavy ion collisions of A with A nucleons and B with B nucleons is

$$< T_{AB} >= \frac{\int T_{AB}(b) d^2b}{\int d^2b \frac{d^2\sigma^{AB}}{d^2b}} = \frac{AB}{\sigma^{AB}} \tag{6.9}$$

where b is the impact parameter, which is the distance between the centers of the two nuclei when the two centers lie in a vertical plane at the moment of collision (for more details see [109]). σ^{AB} is the total inelastic cross section. For d+Au,

$$< T_{dA} >= \frac{2 \times 197}{\sigma^{dA}} = 179.9 b^{-1} \pm 12.4 b^{-1} \tag{6.10}$$

where σ_{dA} is calculated to be 2.26 ± 0.16 b based on a measurement from RHIC Run 3 in 2003 [110]. The other input required to find R_{dA} is $\frac{dN}{dy}$, which is given by

$$\frac{dN^{e-\mu}}{dy} = \frac{c_{bias} N^{e-\mu}}{N_{MB} \epsilon \Delta y} \tag{6.11}$$

where ϵ is the overall acceptance$\times$efficiency correction, Δy is the width of the rapidity window used, and c_{bias} is the overall bias factor. This is defined as $c_{bias} = \frac{1/\text{hard scattering events triggered by BBC}}{1/\text{fraction of events counted}}$. The top ratio corrects for the inefficiency of the BBC to fire on the type of hard scattering events we are studying. Because no data was available on how often the BBC fires for muon events, we used the ratio for hard scattered pions, which is 0.78 as stated above. The bottom factor is the fraction of the total cross section recorded by the BBC minimum bias triggers. The bias factor corrects to the true number of events that occured, and also the true number of e$-\mu$ events that took place. This factor is found to be equal to 0.889 ± 0.001 for Run 8 [105] and equal to 0.696 ± 0.069 for Run 6 [95].

R_{dA} is a measure of particle yield suppression relative to the p+p baseline, see Sec. 1.5. This quantity is useful for determining the magnitude of cold nuclear

matter effects on charm in d+Au collisions.

6.2.2 Results for e$-\mu$ cross section in p+p

The e$-\mu$ production cross sections may be found from the total integrated number of pairs per minimum bias event. For Run 6 north and south arms, these values are:

$$\frac{N_{\text{pairs north}}}{N_{MB}} = 1.90 \times 10^{-7} \pm 7.98 \times 10^{-8}(\text{stat.}) \pm 8.15 \times 10^{-8}(\text{syst.}) \quad (6.12)$$

$$\frac{N_{\text{pairs south}}}{N_{MB}} = 2.14 \times 10^{-7} \pm 7.47 \times 10^{-8}(\text{stat.}) \pm 7.43 \times 10^{-8}(\text{syst.}) \quad (6.13)$$

and for Run 8 north arm this is:

$$\frac{N_{\text{pairs north}}}{N_{MB}} = 7.44 \times 10^{-7} \pm 2.87 \times 10^{-7}(\text{stat.}) \pm 2.80 \times 10^{-7}(\text{syst.}) \quad (6.14)$$

The Run 6 yields give cross sections (using Eq. 6.7):

$$\frac{d\sigma^{\eta=0.87}}{dy} = 7.99 \pm 3.36(\text{stat.}) \pm 3.43(\text{syst.})\text{nb} \quad (6.15)$$

$$\frac{d\sigma^{\eta=-0.87}}{dy} = 9.00 \pm 3.14(\text{stat.}) \pm 3.12(\text{syst.})\text{nb} \quad (6.16)$$

The cross sections given are specific for the kinematic range used in the analysis: $p_T > 0.5$ for electrons, $p_T > 1.0$ for muons, and they are reported for a mean of $\eta = 0.873$ for pairs in the north arm and $\eta = -0.875$ for pairs in the south arm. The rapidity window over which the cross section is evaluated must be chosen, and for this we used the width of the window for the muons, $\Delta\eta = 0.7$. Because electrons and muons are light particles, rapidity is almost identical to the pseudorapidity, so here we approximate $\eta \approx y$.

6.2.3 R_{dA} Measurement

R_{dA} was measured using the yield values in Sec. 6.2.2 and the correction factors in Sec. 6.2.1. The yields for the north arm Run 8 d+Au distribution were compared with those of the north arm Run 6 p+p distribution. A comparison of results from the same Muon Arm were used, rather than a comparison with the combined north and south Run 6 distribution, to limit systematic uncertainties: many of the uncertainties for the north arm are common to

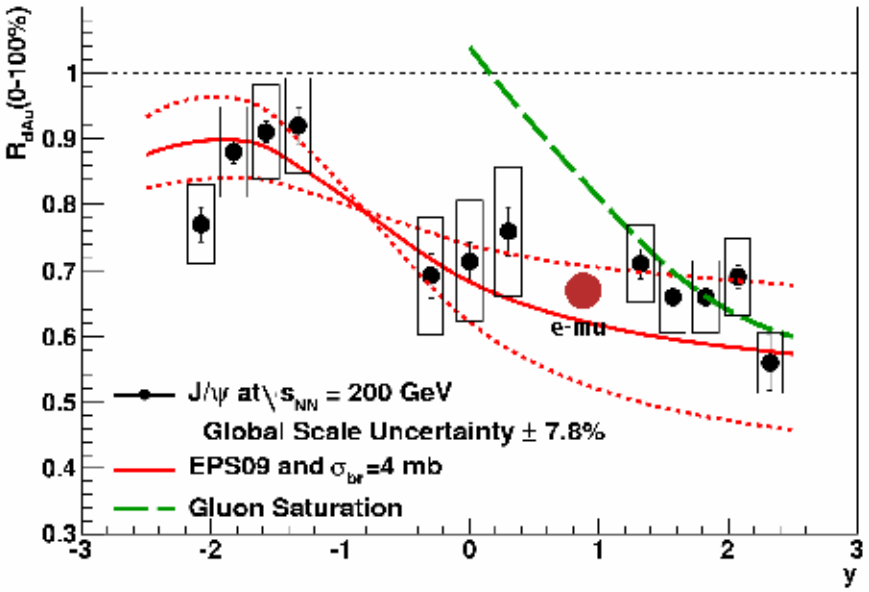

Figure 6.6: Comparison of R_{dA} for electron-muon pairs with that of J/Ψ pairs as a function of rapidity. The e$-\mu$ point is labeled and shown in a red circle. From [111].

both datasets, and cancel when taking the ratio. Using Eq. 6.8, we get that for forward rapidity charm pairs,

$$R_{dA}^{e-\mu} = 0.678 \pm 0.387(\text{stat.}) \pm 0.395(\text{syst.}) \tag{6.17}$$

A comparison of the e$-\mu$ R_{dA} point with the existing Run 8 J/Ψ measurement R_{dA} results is shown in Fig. 6.6.

6.3 Comparing e$-\mu$ Results to Simulations

6.3.1 Charm Production Process Contribution

Information on the charm production processes responsible for e$-\mu$ pairs can be found by comparing the results to an NLO simulator. For this we use POWHEG, interfaced with Pythia to simulate showering (see Sec. 2.6.2). It attempts to simulate all charm processes, specifically gluon fusion, flavor excitation, and gluon splitting, in realistic ratios. This is in contrast to Pythia, which includes these processes as corrections, making it impossible to determine the level at which they contribute.

Plots of like sign subtracted e$-\mu$ pairs from POWHEG, are shown in Fig. 6.7. Gluon fusion events were determined to be those that involved a simple $2 \rightarrow 2$ scattering of two gluons to two heavy quarks. Flavor excitation and gluon splitting events included one or two initial state gluons and two heavy quarks in the final state, as well as a final gluon. It was impossible to tell the difference between these two processes, though, because the Les Houches format output file does not include information on whether both quarks were produced in the final state or if one split in the initial state. Furthermore, it is possible that some gluon fusion events with final state gluon radiation were included in this sample. It is clear from this that gluon fusion without initial gluon radiation is only a minor contribution. The other processes contribute to the

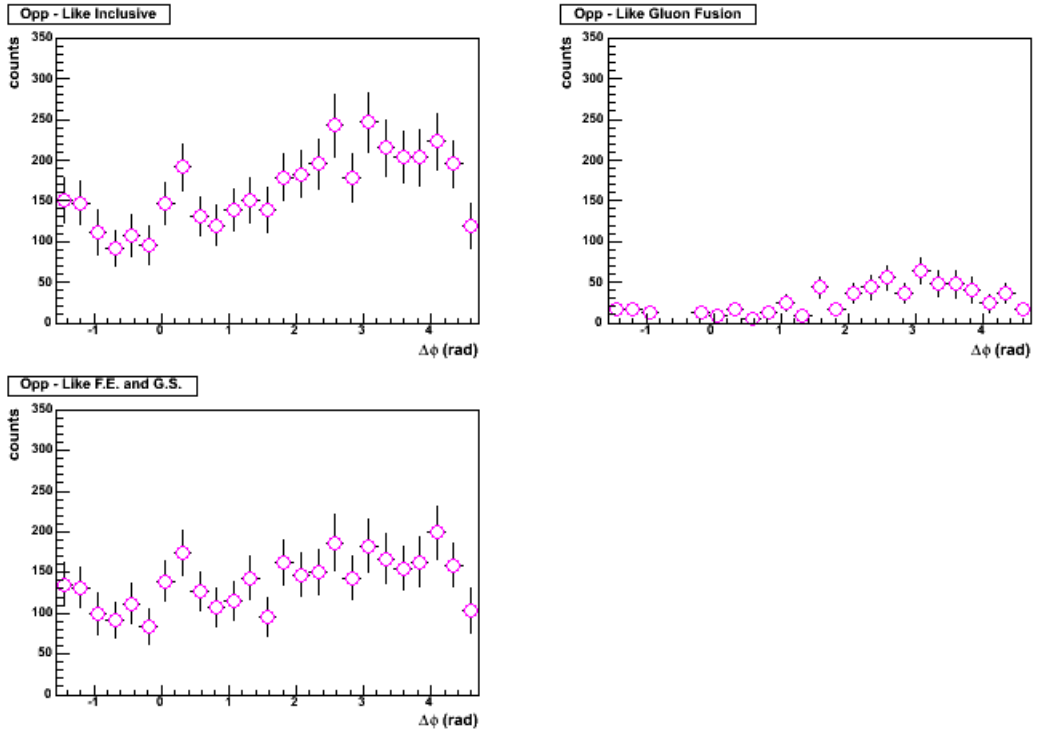

Figure 6.7: $\Delta\phi$ distributions for contributions to POWHEG charm e$-\mu$ pairs (clockwise from top left): inclusive, gluon fusion, and combination of flavor excitation and gluon splitting.

flat plateau far from $\Delta\phi = \pi$, a feature that can also be seen in the data. Gluon fusion account for approximately 16% of the total e$-\mu$ production, while the combination of flavor excitation and gluon splitting comprises the rest.

When the POWHEG e$-\mu$ distribution is compared to those from the p+p data, the relative levels of the far side peak and the near side plateau nearly match (Fig. 6.9). This means it is likely that POWHEG is properly simulating the charm production mechanisms which result in forward rapidity e$-\mu$ pairs. In this plot the POWHEG is normalized to the integral of the data: unlike

Pythia, it is difficult to absolutely normalize POWHEG because it does not provide a process cross section. For a comparison to Pythia (which is absolutely normalized, using a K factor of 3.5), we show the comparison to data we previously found in the last chapter (Fig. 6.8). The POWHEG distribution matches the plateau seen away from $\Delta\phi = \pi$, while the Pythia does not. A Kolmogorov statistical comparison test was performed on the distributions, comparing the likelihood that the data distributions match either the Pythia or the POWHEG distributions. Using this it was found that the POWHEG is a more likely match.

6.3.2 Charm $\sqrt{< k_T^2 >}$ Determination from Pythia

The intrinsic transverse momentum of a parton relative to its hadron is known as k_T. The presence of a random transverse momentum causes an inbalance in the hard scattering process, which can be seen as a broadening of the angular width of the jet spectrum. PHENIX has previously used an analysis of dihadron correlations to estimate the spread in k_T values for various trigger and associated p_Ts [112].

To estimate the $< k_T >$ for charm quark pairs, we have run Pythia simulations with various values of $< k_T >$ preset. These simulations were run with the setting MSEL = 4, so effectively only gluon fusion processes are analyzed. While this is not an exact model of the data, gluon fusion processes contribute

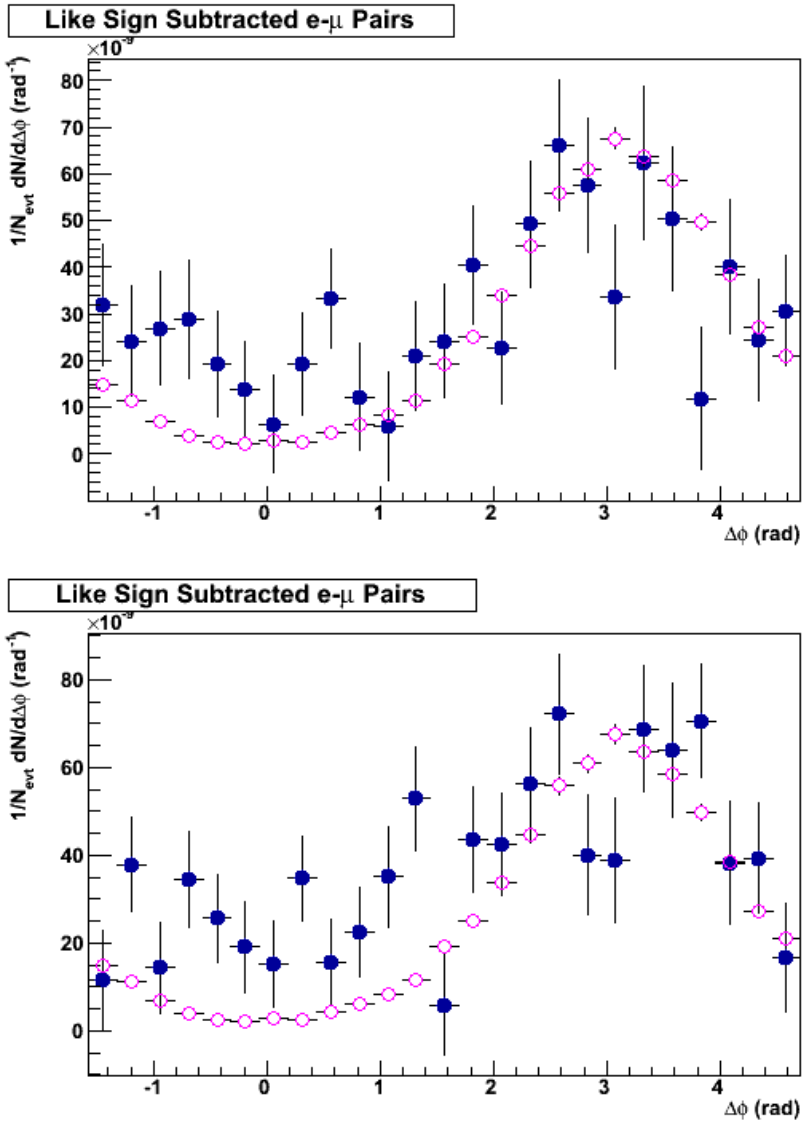

Figure 6.8: Run 6 p+p data (filled blue) vs. Pythia simulated (open magenta) e$-\mu$ pairs for north arm (top) and south arm (bottom). The Kolmogorov comparison test gives a probability of ≈ 0.

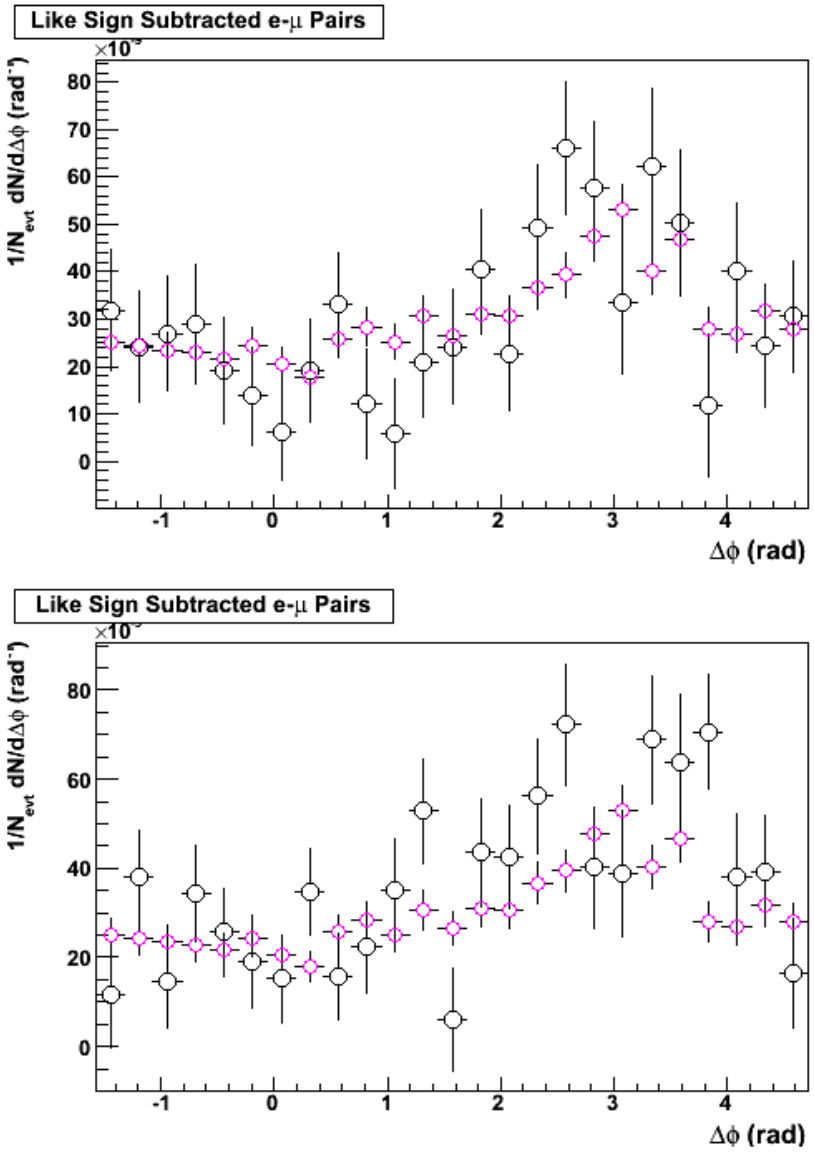

Figure 6.9: Run 6 p+p data (black) vs. POWHEG simulated (magenta) e$-\mu$ pairs for north arm (top) and south arm (bottom). Kolmogorov probability for north = 0.66, for south = 0.40.

Table 6.2: $< k_T >$ estimate for gaussian widths from data

Dataset	width	estimated $< k_T >$	90% confidence interval
Run 6 North	0.921	1.457	$0.15 < k_T < 3.35$
Run 6 South	0.883	1.133	$0 < k_T < 2.095$
Run 6 Combined	0.897	1.250	$0 < k_T < 2.228$

solely to the peak, while the other processes contribute mostly to the broad plateau. This means the broadening of the peak will be in a large part due to $< k_T >$ smearing in fusion processes. Futhermore, we had to use Pythia because it is not possible to set the value of k_T in POWHEG. Four values of $< k_T >$ were set and simulations run for each value. Then the away side width was found using a gaussian fit, and the widths were found to depend linearly on $< k_T >$ (see Figs. 6.10, 6.11). The measured widths of the gaussian distributions of the Run 6 data were then used to calculate the corresponding $< k_T >$, along with the 90% confidence interval using an uncertainty analysis as in [113]. The k_T value matching the measured σ was found from a linear regression of the form $\sigma = ak_T + b$, and the reported ranges take into account the correlation of the a and b fit parameters. These results are shown in Table 6.2.

6.3.3 Bottom Contribution

Bottom quark production is also expected to produce e$-\mu$ pairs, though not with the same azimuthal distribution as those produced from charm. This

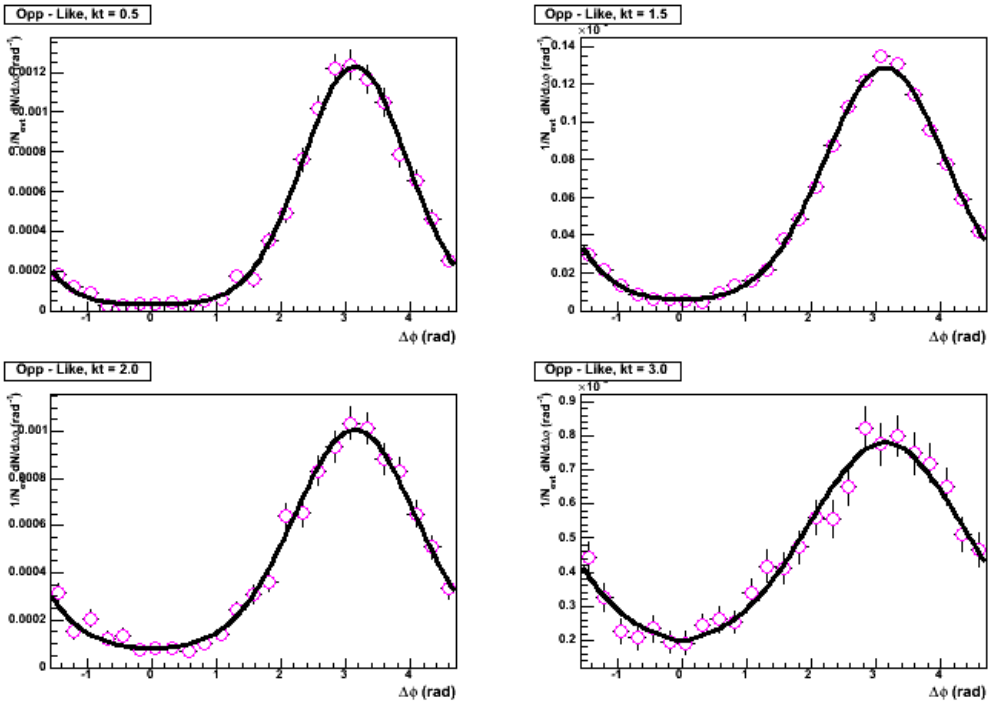

Figure 6.10: Like sign subtracted $\Delta\phi$ distributions for various values of k_T, fit to wrapped gaussians. RMS values: top left, $k_T = 0.5$ and $\sigma = 0.806$, top right, $k_T = 1.5$ (standard Pythia value) and $\sigma = 0.930$, bottom left, $k_T = 2.0$ and $\sigma = 0.940$, and bottom right, $k_T = 3.0$ and $\sigma = 1.163$.

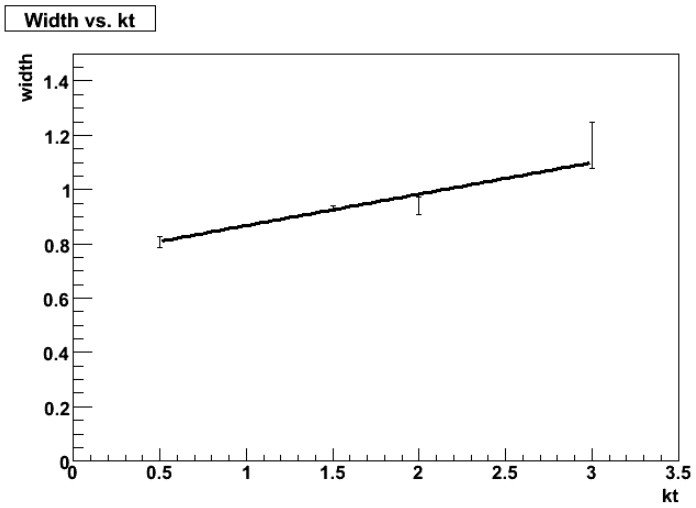

Figure 6.11: Away side width (Gaussian σ) vs. intrinsic k_T. Fits a functional form of $\sigma = 0.752 + 0.116 k_T$.

is because often two semileptonic decays are involved, those of the original B mesons and also those of their D meson daughters. We have previously been assuming that all opposite sign pairs are signal, and like sign pairs are background. This is not necessarily the case for e$-\mu$ pairs from B decay, given that up to four e$-\mu$ combinations are created for every bottom pair: some of these will be like sign. The multiple semi-leptonic decays also tend to smear out the angular distributions, which look much different than the distributions for pairs from charm. The opposite sign and like sign distributions for e$-\mu$ pairs from bottom are shown in Fig. 6.12.

Because the analysis procedure does not isolate bottom, only charm, it is not correct if bottom is a major contributor to the pairs. Recent measurements using heavy flavor electrons [81], [114] show that the fraction of heavy flavor

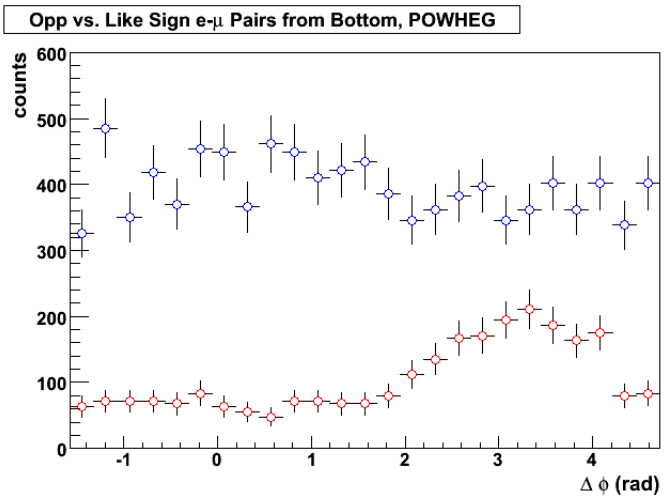

Figure 6.12: Opposite (blue) vs. same sign (red) $\Delta\phi$ for e$-\mu$ pairs from bottom events, POWHEG (unscaled).

electrons from bottom levels off at around 50% for high p_T. However for the measured e$-\mu$ pairs not more than 3% have $p_T > 3.0$, and for this momentum range the fraction of bottom is much lower. Studies using both Pythia and POWHEG have shown that bottom e$-\mu$ distributions are of the order 10^2 lower in yield than those from charm (see Fig. 6.13). Because the uncertainty from the bottom yield is small enough to be within systematic uncertainty, we can neglect this contribution.

6.4 Interpretation of Results

We have found that e$-\mu$ pairs are suppressed in d+Au collisions relative to p+p, and the away side peak has essentially disappeared. Although this is the

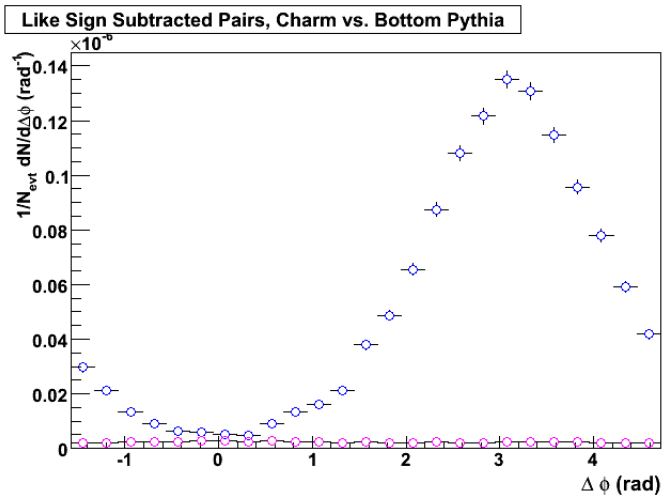

Figure 6.13: Like sign subtracted e$-\mu$ $\Delta\phi$ correlations from Pythia, charm gluon fusion (blue) vs. bottom gluon fusion (magenta).

first study at RHIC of forward charm correlations, related results have been found using hadron correlations. STAR finds hints of away side disappearance and broadening in forward-central hadron correlations [115], while PHENIX finds a minimal effect [52]. A larger effect has been seen in forward-forward hadron pairs, where the effective pair rapidity is much larger [116]. All RHIC experiments have confirmed suppression of single particles at forward rapidities (see Sec. 1.5).

The most popular current theory to explain forward suppression is the CGC model, discussed in Sec. 1.4.2. Effects are predicted to be large only at very low x, generally $x < 0.01$. To determine the x range seen in this analysis, a study was done using Pythia charm production to plot the inital parton x values for events producing e$-\mu$ pairs. The results are shown in Fig. 6.14. The mean x

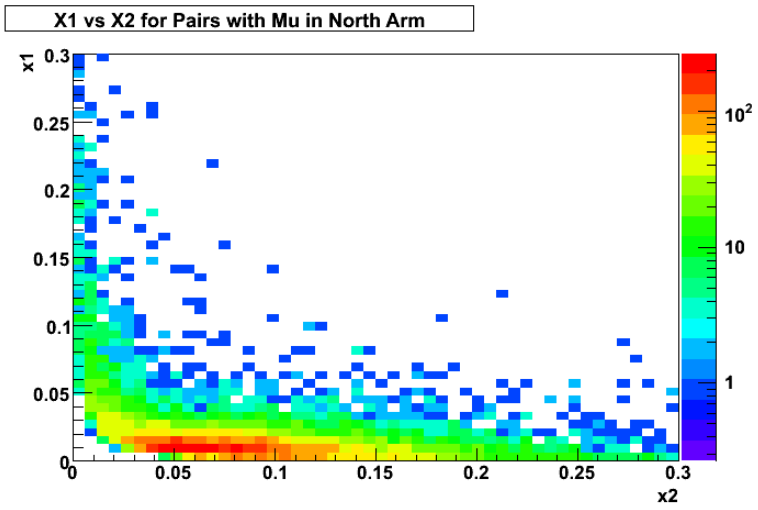

Figure 6.14: x ranges for partons resulting in forward e$-\mu$ pairs. Vertical axis corresponds to particle in backward-going parton, horizontal to forward-going parton.

of the struck backward-going parton, corresponding to the parton in the gold nucleus in a d+Au collision, is 0.0199 ± 0.0003. This puts it slightly outside the kinematic range of CGC effects. However, Kharzeev postulates that there is a transition region between CGC dominated and hard scattering dominated regimes, where intermediate effects are seen [117]. In this "region of extended scaling," the away-side jet may not be totally replaced by gluon emission (as in the CGC framework), but might just become somewhat decorrelated due to gluon radiation. This effect would be especially enhanced with rapidity-separated pairs, because gluon radiation is proportional to Δy. Forward charm suppression may also be explained by final state multiple scattering, which predicts charm suppression to be of the same order of magnitude as that of light quarks [69].

It is not clear we have enough information to determine why the away-side peak disappears for e$-\mu$ pairs in d+Au. While CGC effects may be responsible, it is also possible that charm production processes are different in d+Au as compared with p+p. The POWHEG results show that if production is dominated by flavor excitation and gluon splitting processes, a flat spectrum in $\Delta\phi$ would result. The reason why these processes would be enhanced relative to gluon splitting in cold nuclear matter is unknown, though. Clearly more theoretical studies will have to be done on this issue.

Chapter 7

Conclusions

The purpose of this thesis has been to describe the first electron-muon analysis made at RHIC. Because it is a clean measurement with low background, e$-\mu$ pairs have long been predicted to be a clear indicator of charm production, and we have shown this to be the case. When the first measurements demonstrating charm energy loss and flow were made at RHIC, interest in charm as a probe of the QGP increased greatly. While it is possible to accurately measure charm using single electrons at PHENIX, such a clean measurement of charm correlations has not previously been made. Correlations yield additional information that cannot be obtained from single particle measurements alone in all three systems that are studied at RHIC. In p+p collisions, the shape of the angular correlation is dependent on the QCD processes by which charm is produced, as well as by the initial transverse momentum (k_T) of the charm quarks. Modifications to the correlation shape can be seen in d+Au

collisions, where initial state shadowing may cause suppression of the away side jet. Finally, the comparison of heavy ion collisions with d+Au will show the additional final state effects of the hot medium on the jet shape. Taken together, these measurements will show the full range of effects acting on charm in both cold and hot nuclear matter.

The results for e$-\mu$ in p+p collisions agree with the predictions from POWHEG, which models higher order charm production processes. Instead of only observing an away side peak, as expected from simple gluon fusion processes, we see a broad plateau-like structure, indicating that processes involving initial and final state gluon radiation are important. This structure is not seen in Pythia simulations of e$-\mu$ pairs, which indicates that higher order processes must be accurately taken into account to describe the production of charm pairs.

Interpreting the d+Au results is a bit more difficult. The measured R_{dA} is consistent with that measured for forward J/Ψ and single muons [95] [111]. This indicates that the level of supression at the intermediate rapidity range studied is more consistent with that of higher rapidities, rather than the Cronin enhancement seen in the open charm spectrum at central rapidity [118]. There is also a significant disappearance of the away side peak in the d+Au correlation, the degree of which is somewhat unexpected. It could indicate pair suppression, as well as disassociation of pairs in the cold nuclear matter. It could also be due to a shift in charm production mechanisms relative to p+p

collisions. A detailed theoretical study would help disentangle these effects.

A natural extension to this study will be the analysis of e$-\mu$ pairs in Au+Au collisions. The interaction of charm jets with the QGP may yield information on charm energy loss effects through a modification of the jet shape, similar to what is seen with hadron correlations. Observations of an extended ridge in $\Delta\eta$ and double-hump Mach cone-type structures in charm jets could yield new insight into the causes of these effects, already seen in other jet studies. It will be interesting to see if any jet structure is visible, given the large away side jet suppression already evident from the d+Au data.

Studies have already been done in Au+Au using electron-hadron correlations [97] [119], but due to the large background in these measurements it is hard to interpret the results. While e$-\mu$ is a cleaner measurement, it is currently limited due to the vertex resolution of the PHENIX muon detectors. Fortunately, however, the accurate measurement of heavy flavor electrons and muons will soon be vastly improved due to the addition of the Silicon Vertex Tracker (VTX) and the Forward Vertex Tracker (FVTX). These two detectors are designed to measure displaced vertices due to heavy flavor decay. They do this by making very precise measurements of tracks close to the interaction region. If a D meson decays to a lepton, the lepton originates at a point removed from the event vertex because the D traveled before it decayed. The silicon detectors will be able to increase the precision of track reconstruction to a point where these offsets will be measureable. Then heavy flavor electrons

and muons may be tagged, greatly reducing combinatoric background. With this heavy flavor tagging, a study of e$-\mu$ in Au+Au will be possible.

Bibliography

[1] *The PHOBOS Perspective on Discoveries at RHIC*, B. B. Back et al., Nucl. Phys. A **757**, 28 (2005). 3

[2] M. Peskin and D. Schroeder, *An Introduction to Quantum Field Theory* (Addison-Wesley, 1995). 4

[3] G. Dissertori, I. Knowles, and M. Schmelling, *Quantum Chromodynamics, High Energy Experiments and Theory* (Oxford Science Publications, 2003). 5, 18, 20

[4] *Asympotic Sum Rules at Infinite Momentum*, J. D. Bjorken, Phys. Rev **179**, 1547 (1969). 6, 19

[5] *Deep Inelastic Electron Scattering*, J. I. Friedman and H. W. Kendall, Annual Review of Nuclear Science **22**, 203 (1972). ix, 6, 21, 22

[6] *Factorization for hard exclusive electroproduction of mesons in QCD*, J. Collins, L. Frankfurt, and M. Strikman, Phys. Rev. D **56**, 2982 (1997). 6

[7] *Jet quenching and radiative energy loss in dense nuclear matter*, M. Gyulassy et al., Quark Gluon Plasma 3 pp. 123–191 (2003), nucl-th/0302077. 6, 12

[8] *Asymptotically Free Gauge Theories I*, D. J. Gross and F. Wilczek, Phys. Rev. D **8**, 3633 (1973). 7

[9] *Static and dynamic critical phenomena at a second order QCD phase transition*, K. Rajagopal and F. Wilczek, Nucl. Phys. B (1993). 7

[10] *Transition temperature in QCD*, M. Cheng et al., Phys. Rev. D **74**, 054507 (2006). 7

[11] *Equation of state and QCD transition at finite temperature*, A. Bazavov et al., Phys. Rev. D **80**, 014504 (2009). viii, 9

[12] *Centrality Dependence of Charged Particle Multiplicity in Au-Au Collisions at* $\sqrt{s_{NN}} = 130$ *GeV*, K. Adcox et al., Phys. Rev. Lett. **86**, 3500 (2001). 9

[13] *Formation of dense partonic matter in relativistic nucleus-nucleus collisions at RHIC: Experimental evaluation by the PHENIX collaboration*, K. A. PHENIX Collaboration et al., Nucl. Phys. A **757**, 184 (2005). 9, 11, 199

[14] *Nuclear Modification of Electron Spectra and Implications for Heavy Quark Energy Loss in Au+Au Collisions at* $\sqrt{s_{NN}} = 200$ *GeV*, S. S. Adler et al., Phys. Rev. Lett. **96**, 032301 (2006a). 9, 13

[15] *Hadronization in heavy ion collisions: Recombination and fragmentation of partons*, R. J. Fries et al., Phys. Rev. Lett. **90**, 202303 (2003). 10, 12

[16] *Hadronic dissipative effects on elliptic flow in ultrarelativistic heavy-ion collisions*, T. Hirano et al., Phys. Lett. B **636**, 299 (2006). 10

[17] *Hydrodymanic description of ultrarelativistic heavy-ion collisions*, P. Kolb and U. Heinz, Quark Gluon Plasma 3 (2003), arXiv:nucl-th/0305084. 11

[18] *Elliptic Flow at SPS and RHIC: from kinetic transport to hydrodynamics*, P. F. Kolb et al., Phys. Lett. B **500**, 232 (2001). 11

[19] *Heavy Quark Production in p+p and Energy Loss and Flow of Heavy Quarks in Au+Au Collisions at* $\sqrt{s_{NN}} = 200$ *GeV*, A. Adare et al., arXiv:1005.1627. 11

[20] *Elliptic and hexadecapole flow of charged hadrons in Au+Au collisions at* $\sqrt{s_{NN}} = 200$ *GeV*, A. Adare et al., Phys. Rev. Lett **105**, 062301 (2010). 11

[21] *Viscosity in Strongly Interacting Quantum Field Theories from Black Hole Physics*, P. Kovtun, D. T. Son, and A. O. Starinets, Phys. Rev. Lett. **94**, 111601 (2005). 11

[22] *Strong Color Field Baryonic Remnants in Nucleus-Nucleus Collisions at 200 GeV*, V. T. Pop et al., Phys. Rev. C **72**, 054901 (2005). 12

[23] *Suppression of Non-photonic Electrons from Enhancement of Charm Baryons in Heavy Ion Collisions*, P.Sorensen and X.Dong, Phys. Rev. C **74**, 024902 (2006). 12, 51

[24] *Centrality dependence of high p_T hadron suppression in Au+Au collisions at $\sqrt{s_{NN}} = 130$ GeV*, C. Adler et al., Phys. Rev. Lett. **89**, 202301 (2002). 12

[25] *Heavy-quark probes of the quark-gluon plasma and interpretation of recent data taken at the BNL Relativistic Heavy Ion Collider*, H. van Hees, V. Greco, and R. Rapp, Phys. Rev. C **73**, 034913 (2006). 13

[26] *Experimental and theoretical challenges in the search for the quark gluon plasma: The STAR Collaboration's critical assessment of the evidence from RHIC collisions*, J. Adams et al., Nucl. Phys. A **757**, 102 (2005a). viii, 13

[27] *On a Diffuse Reflection of the α-Particles*, H. Geiger and E. Marsden, Proceedings of the Royal Society A **82**, 495 (1909). 15

[28] *The interpretation of the new particles as displaced charge multiplets*, M. Gell-Mann, Il Nuovo Cimento (1956-66). 15

[29] *Theory of Deep-Inelastic Lepton-Nucleon Scattering and Lepton-Pair Annihilation Processes*, D. Drell, D. Levy, and T. Yan, Phys. Rev. **187**, 2159 (1969). 16

[30] *Review of Particle Physics*, C. Amsler et al., Phys. Lett. B **667**, 1 (2008). 17, 84, 86

[31] *High-energy Electroproduction and the Constitution of the Electric Current*, J. C. G. Callan and D. Gross, Phys. Rev. Lett. **22**, 156 (1969). 20

[32] *Measurement of the neutral current cross section and F_2 structure function for deep inelastic e+p scattering at HERA*, M. Derrick and others (ZEUS collaboration), Eur. Phys. J **C21**, 443 (2001). ix, 22, 23, 25

[33] *Calculation of the Structure Functions for Deep Inelastic Scattering and e+ e- Annihilation by Perturbation Theory in Quantum Chromodynamics*, Y. L. Dokshitzer, Sov. Phys. JETP **46**, 641 (1977). 24

[34] *Asymptotic Freedom in Parton Language*, G. Altarelli and G. Parisi, Nucl. Phys. **B126**, 298 (1977). 24

[35] *Deep inelastic e p scattering in perturbation theory*, V. N. Gribov and L. N. Lipatov, Sov. J. Nucl. Phys. **15**, 438 (1972). 24

[36] *The Pomeranchuk Singularity in Nonabelian Gauge Theories*, E. A. Kuraev, L. N. Lipatov, and V. S. Fadin, Sov. Phys. JETP **45**, 199 (1977). 26

[37] *The Pomeranchuk Singularity in Quantum Chromodynamics*, Y. Balitsky and L. Lipatov, Sov. J. Nucl. Phys. **28**, 22 (1978). 26

[38] *Proton Structure, Partons, QCD, DGLAP and Beyond*, A. Martin, ACTA Physica Polonica B **39**, 2025 (2008). 26

[39] *The Ratio of the Nucleon Structure Functions $f_2(n)$ for Iron and Deuterium*, J. Aubert et al., Phys. Lett. B **123**, 275 (1983). 27

[40] *Nuclear effects in structure functions*, M. Arneodo, Physics Reports **240**, 301 (1994). ix, 27, 29, 30, 32

[41] *Nuclear Shadowing*, N. Armesto, J. Phys. G **32**, R367 (2006). 29, 30

[42] *Vector Meson Dominance*, D. Schildknecht, ActaPhys. Polon. B **37**, 595 (2006). 29

[43] *Asymptotic Behavior and Subtractions in the Mandelstam Representation*, M. Froissart, Phys. Rev. **123**, 1053 (1961). 33

[44] *The Color Glass Condensate and Small x Physics: 4 Lectures*, L. McLerran, Lect. Notes Phys. **583**, 291 (2002). 33

[45] *Evolution at small x_{bj}: The Color Glass Condensate*, H. Weigert, Prog. Part. Nucl. Phys. **55**, 461 (2005). x, 35

[46] *Nuclear modification factor in d+Au collisions: Onset of suppression in the color glass condensate*, D. Kharzeev, Y. V. Kovchegov, and K. Tuchin, Phys. Lett. **B599**, 23 (2004), hep-ph/0405045. 36

[47] *Evolution of the nuclear modifiation factors with rapidity and centrality in d+Au collisions at $\sqrt{s_{NN}} = 200$ GeV*, I. Arsene et al., Phys. Rev. Lett. **93**, 242303 (2004). x, 36, 37

[48] *Nuclear Modification Factors for Hadrons at forward and backward rapidities in deuteron-gold collisions at $\sqrt{s_{NN}} = 200$ GeV*, S. Adler et al., Phys. Rev. Lett. **94**, 082302 (2005). x, 36, 38

[49] *Forward neutral pion production in p+p and d+Au collisions at $\sqrt{s_{NN}} =$ 200 GeV*, J. Adams et al., Phys. Rev. Lett. **97**, 152302 (2006). x, 36, 37, 39

[50] *Cronin effect and high-p_T suppression in pA collisions*, D. Kharzeev, Y. Kovchegov, and K. Tuchin, Phys. Rev. D **68**, 094013 (2003). 36

[51] *Forward Production in d+Au collisions by parton recombination*, R. C. Hwa, C. B. Yang, and R. J. Fries, Phys. Rev. C **71**, 024902 (2005). 37

[52] *Azimuthal Angle Correlations for Rapidity Separated Hadron Pairs in d+Au Collisions at $\sqrt{s_{NN}} = 200$ GeV*, S. S. Adler et al., Phys. Rev. Lett. **96**, 222301 (2006b). 37, 213

[53] *Nonleptonic Weak Decays and the Eightfold Way*, M. Gell-Mann, Phys. Rev. Lett. **12**, 155 (1964). 40

[54] *Elementary Particles and SU(4)*, B. Bjorken and S. Glashow, Phys. Lett **11**, 255 (1964). 40

[55] *Weak Interactions with Lepton-Hadron Symmetry*, S. L. Glashow, J. Iliopoulos, and L. Maiani, Phys. Rev. D **2**, 1285 (1970a). 40

[56] *Charmed and bottom flavoured particle production in hadronic interactions*, S. Tavernier, Rep. Prog. Phys. **50**, 1439 (1987). 40, 42

[57] *Weak Interactions with Lepton-Hadron Symmetry*, S. L. Glashow, J. Iliopoulos, and L. Maiani, Phys. Rev. D **2**, 1285 (1970b). 41

[58] *Experimental Observation of a Heavy Particle J*, J. J. Aubert et al., Phys. Rev. Lett. **33**, 1404 (1974). 41

[59] *Discovery of a Narrow Resonance in e^+e^- Annihilation*, J. E. Augustin et al., Phys. Rev. Lett. **33**, 1406 (1974). 41

[60] *Discovery of a Second Narrow Resonance in e^+e^- Annihilation*, G. S. Abrams et al., Phys. Rev. Lett. **33**, 1453 (1974). 41

[61] G. Zweig (1964), CERN report TH.412. 42

[62] *Heavy Quarks and e^+e^- Annihilation*, T. Appelquist and H. D. Politzer, Phys. Rev. Lett. **34**, 43 (1975). 42

[63] *Observation of a dimuon resonance at 9.5-GeV in 400-GeV proton - nucleus collisions*, S. W. Herb et al., Phys. Rev. Lett. **39**, 252 (1977). 43

[64] A. Pickering, *Constructing quarks: a sociological history of particle physics* (University of Chicago, 1984). 43

[65] *Heavy Particle Production in High-Energy Hadron Collisions*, G. S. J. Collins, D. Soper, Nucl. Phys. B **263**, 37 (1986). 43, 44

[66] *Charm Parton Content of the Nucleon*, J. Pumplin, H. L. Lai, and W. K. Tung, Phys. Rev. D **75**, 054029 (2007). 44

[67] *Systematics of Charm Production in Hadronic Collisions*, R. Vogt, S. J. Brodsky, and P. Hoyer, Nucl. Phys. B **383**, 643 (1992). 44, 47

[68] *Production and hadronization of heavy quarks*, E. Norrbin and T. Sjostrand, Euro. Phys. Journal C **17**, 131 (2000). x, xi, 44, 46, 47, 48

[69] *Open charm tomography of cold nuclear matter*, I.Vitev et al., Phys. Rev. D **74**, 054010 (2006). x, 48, 50, 51, 214

[70] *The total charm cross section*, R. Vogt, Eur. Phys. J. ST **155**, 213 (2008). 49

[71] *Heavy-quark colorimetry of QCD matter*, Y. Dokshitzer and D. Kharzeev, Phys. Lett. B **519**, 199 (2001). 49

[72] *Nuclear Effects on Hadron Production in d+Au and p+p Collisions at* $\sqrt{s_{NN}} = 200\ GeV$, S. S. Adler et al., Phys. Rev. C **74**, 024904 (2006c). 51

[73] *Looking for intrinsic charm in the forward region at BNL RHIC and CERN LHC*, V. P. Goncalves, F. S. Navarra, and T. Ullrich, Nucl. Phys. A **842**, 59 (2010). 51

[74] *Open charm yields in d+Au collisions at* $\sqrt{s_{NN}} = 200\ GeV$, J. Adams et al., Phys. Rev. Lett. **94**, 062301 (2005b). 52

[75] *Measurement of single muons at forward rapidity in* $p + p$ *collisions at* $\sqrt{s} = 200 GeV$ *and implications for charm production*, S.S.Adler et al., Phys. Rev. D **76**, 092002 (2002). xi, xv, 54, 90, 112, 115

[76] *Measurement of high-*p_T *single electrons from heavy flavor decays in p+p collisions at* $\sqrt{s} = 200 GeV$, A. Adare et al., Phys. Rev. Lett. **97**, 252002 (2006). 52

[77] W. Xie, in *DIS conference* (2010). 53

[78] *Dilepton mass spectra in p+p collisions at* $\sqrt{s_{NN}} = 200 GeV$ *and the contribution from open charm*, A. Adare et al., Phys. Lett. B **670**, 313 (2009a). 53, 59

[79] *Heavy quark production in p+p and energy loss and flow of heavy quarks in Au+Au collisions at* $\sqrt{s_{NN}} = 200 GeV$, A. Adare et al., arXiv:1005.1627v2. 53

[80] *Transverse momentum and centrality dependence of high-*p_T *non-photonic electron suppression in Au+Au collisions at* $\sqrt{s_{NN}} = 200 GeV$, B. I. Abelev et al., Phys. Rev. Lett. **98**, 192301 (2007). xi, 53, 56

[81] *Measurement of Bottom versus charm as a function of transverse momentum with electron-hadron correlations in p+p collisions at* $\sqrt{s_{NN}} = 200 GeV$, A. Adare et al., Phys. Rev. Lett. **103**, 082002 (2009b). xi, 57, 211, 234

[82] *Heavy-flavor correlation measurements via electron azimuthal correlations with open charm mesons*, A. Mischke, J. Phys. G **35**, 044022 (2008). 57

[83] *Hard Probes in Heavy Ion Collisions at the LHC: Heavy Flavour Physics*, M. Bedjidian et al., hep-ph/03011048. 59

[84] *Matching NLO QCD computations with parton shower simulations: the POWHEG method*, S. Frixione, P. Nason, and C. Oleari, Journal of High Energy Physics **2007** (2007), arXiv:0709.2092. 60

[85] *A standard format for Les Houches Event Files*, P. Skands et al., Computer Physics Communications **176**, 300 (2007). 60

[86] *The RHIC Injector Accelerator Configurations, and Performance for the RHIC 2003 Au-d Physics Run*, L. Ahrens et al., Proceedings of the 20003 Particle Accelerator Conference. 66

[87] *PHENIX inner detectors*, M. Allen et al., NIM **A499**, 549 (2003). 73

[88] *The RHIC Zero Degree Calorimeter*, C. Adler et al., NIM **A470**, 488 (2001). 74

[89] *PHENIX central arm tracking detectors*, K. Adcox et al., NIM **A499**, 489 (2003a). 76, 78

[90] *Construction and performance of the PHENIX pad chambers*, K. Adcox et al., NIM A **497**, 263 (2003b). 78

[91] *Event Reconstruction in the PHENIX Central Arm Spectrometers*, J. T. Mitchell et al., Nuclear Instruments and Methods **482**, 491 (2002), nucl-ex/0201013. 81

[92] *PHENIX central arm particle I.D. detectors*, M. Aizawa et al., NIM **A499**, 508 (2003). 84

[93] *The PHENIX Calorimeter*, L. Aphecetche et al., NIM **A499**, 521 (2003). 87

[94] *PHENIX muon arms*, H. Akikawa et al., NIM **A499**, 537 (2003). 89

[95] *A measurement of open charm using single muons at forward angles for p+p collisions at center of mass 200 GeV*, D. Hornback, Ph.D thesis (2008). xv, 95, 99, 112, 200, 217

[96] *PHENIX on-line systems*, S. S. Adler et al., NIM **A499**, 560 (2003). 96, 100

[97] *Azimuthal Correlations of Electrons from Heavy Flavor Decay with Hadrons in Au+Au and p+p Collisions at* $\sqrt{s} = 200$ *GeV*, A. Adare et al., arXiv:1011.1477. 103, 218

[98] *Run6pp 200GeV Muon Arm QA*, H. Liu et al., PHENIX Analysis Note 636. 106

[99] *GEANT 4-a simulation toolkit*, S. Agostinelli, Nuclear Instruments and Methods in Physics Research Section A:Accelerators, Spectrometers, Detectors and Associated Equipment **506**, 250 (2003). 132

[100] *Personal communication with Nathan Grau.* 148

[101] *PHENIX Analysis Note 116*, T. Hemmick et al. 148

[102] *Personal communication with Donald Hornback.* 165

[103] *Decomposition of harmonic and jet contributions to particle-pair correlations at ultrarelativistic energies*, N. Ajitanand et al., Phys. Rev. C **72**, 011902 (2005). 174

[104] *Combining PHENIX measureents: Weighted averages, correlations and separation of combined errors*, D. d'Enterria. 177

[105] *PHENIX Run-08 d-Au at 200 GeV Centrality Categorization*, J. Nagle, PHENIX Analysis Note 900. 190, 200

[106] *BBC Efficiency for Neutral Pions and Etas in the Central Arm in Run-06 p+p at* $\sqrt{s} = 200\,GeV$, J. Seele, C. Aidala, and F. Ellinghaus. 198

[107] *Single electrons from heavy flavor decays in* $p + p$ *collisions at* $\sqrt{s} = 200\,GeV$, Y. Akiba et al. 199

[108] *Personal communication with Anne Sickes.* 199

[109] *Glauber Modeling in High Energy Nuclear Collisions*, M. Miller et al., Ann. Rev. Nucl. Part. Sci. **57**, 205 (2007). 199

[110] *Diffraction Dissociation - 50 Years Later*, S. White, AIPConf. Proc. **792** (2005), arXiv:nucl-ex/0507023. 200

[111] A. Adare et al., submitted to Physical Review Letters, arXiv:1010.1246. xxv, 203, 217

[112] *Jet Properties and Dihadron Correlations in p+p Collisions at* $\sqrt{s} = 200$ *GeV*, S. Adler et al., Phys. Rev. D **74**, 072002 (2006d). 206

[113] J. Mandel, *The Statistical Analysis of Experimental Data* (Dover, 1964). 209

[114] *Measurement of the Bottom Contribution to non-photonic electron production in p+p at* $\sqrt{s} = 200\,GeV$, M. M. Aggarwal et al., Phys. Rev. Lett. **105**, 202301 (2010). 211

[115] E. Braidot, arXiv:1008.3989v1 [nucl-ex]. 213

[116] *Searching for Gluon Saturation in d+Au Collisions at PHENIX*, B. Meredith (2010). 213

[117] *Jet Azimuthal Correlations and Parton Saturation in the Color Glass Condensate*, D. Kharzeev, E. Levin, and L. McLerran, Nucl. Phys. A **748**, 627 (2005). 214

[118] *Cold Nuclear Matter Effects on Open Heavy Flavor at RHIC*, M. Durham, Talk at Winter Workshop on Nuclear Dynamics, Winter Park, CO February 2011. 217

[119] *Non-photonic electron-hadron azimuthal correlation for AuAu, CuCu and pp collisions at* $\sqrt{s_{NN}} = 200\,GeV$, B. Biritz, Nucl. Phys. A **830**, 849c (2009). 218

[120] C. Wong, *Introduction to high-energy heavy-ion collisions* (World Scientific, 1994). 236

Appendix A

Derivation of Decay Muon Quantities

To estimate the systematic uncertainty due to the decay muon subtraction, we need to calculate the fraction of muons we see using the method outlined in Sec. 5.6.1. The decay portion of the e$-\mu$ spectrum forms a triangle when plotted with respect to the event vertex because of the long lifetime of the parent hadrons (see Fig. A.1). After subtracting near pairs from far pairs, we are left with a sample of pure decay pairs, though it is only a fraction of the total. This fraction is dependent on the zero point of the decay triangle, where decay muons cease to be produced.

To find the zero point, we start with the assumption that hadrons that produce

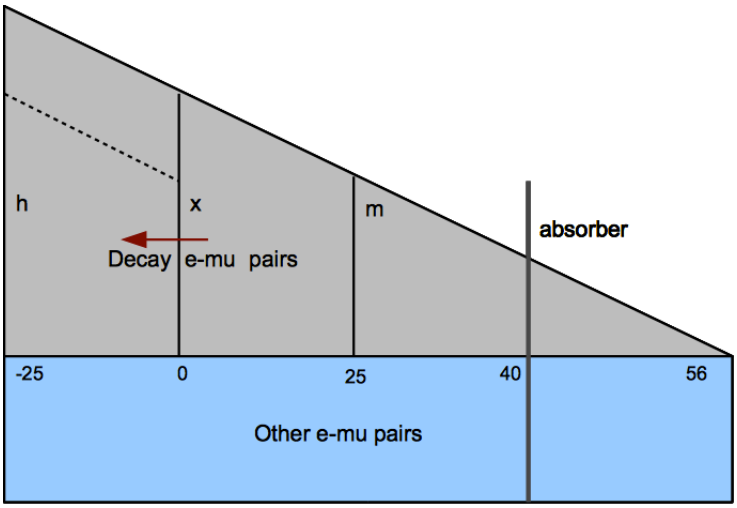

Figure A.1: Diagram of e$-\mu$ pairs vs. event vertex, showing postions of vertex cuts and muon absorber. The distribution between 0 cm $< z_{vtx} <$ 25 cm is shown shifted over the distribution between -25 cm$< z_{vtx} <$ 0 cm to illustrate the subtraction.

decay muons are pions. This is because pions are most numerous, and they have a larger $c\tau$ than kaons, leading to a lower limit on the fraction seen (and an upper limit on the error). If collisions can occur within a range, $-Z_{max} < z < Z_{max}$, then the probability for a pion to be produced in this range is $P_\pi = \frac{1}{2Z_{max}}$. When this is multiplied by the probability for that pion to decay to a muon we have the total probability as a function of vertex for a decay muon to be produced:

$$P_\mu(z) = \frac{1}{2Z_{max}} \int dz \frac{1}{\lambda_d} e^{-\frac{z-z_{max}}{\lambda_d}} \tag{A.1}$$

where λ_d is the decay length of a muon. To find the point where the rate of

muon decay goes to 0, we can solve for where the probability to decay is equal to 0:

$$\frac{1}{2Z_{max}} \int_{Z_{max}}^{Z_0} dz \frac{1}{\lambda_d} e^{-\frac{z-z_{max}}{\lambda_d}} = 0 \tag{A.2}$$

$$\frac{1}{2Z_{max}} \left(-e^{-\frac{Z_0 - Z_{max}}{\lambda_d}} + e^{-\frac{Z_{max} - Z_{max}}{\lambda_d}} \right) = 0 \tag{A.3}$$

$$\frac{Z_0 - Z_{max}}{2Z_{max}\lambda_d} = 0 \tag{A.4}$$

$$Z_0 = Z_{max} \tag{A.5}$$

Here we assume that $\lambda_d >> Z_{max}$, which is reasonable since $c\tau \approx 7.8$ m. Pions can be created in any range between the first two forward absorbers, which are at $Z_{max} = \pm 40$ cm. This is not the whole story though, since pions are not immediately absorbed in the steel - rather, they get absorbed with an interaction length $\lambda_i \approx 16$ cm. Since pions can decay within the absorber, we take the vertex position where muons stop being emitted to be 16 cm within the absorber, or at ± 56 cm along the PHENIX z axis.

By assuming that no pions remain after they have passed a decay length into the absorber, this calculation neglects the decay muons that come from punchthrough hadrons. This is thought to be a small contribution, though: relatively few hadrons punch through the absorber, and only a small fraction of those will go on to decay. Therefore we have neglected these decay muons.

To find the fraction of muons we see after the near side subtraction, we can

again refer to diagram A.1. The subtraction removes all of the non-vertex dependent pairs, as well as many of the decay muons. To find the fraction of decays we measure, we first find the area of the rhombus left when subtracting the area of the near side trapezoid from that of the far (indicated by the dotted line on the diagram):

$$A_1 = 0.25\left(\frac{h+x}{2}\right) - 0.25\left(\frac{x+m}{2}\right) \tag{A.6}$$

$$A_1 = \frac{1}{8}(h-m) \tag{A.7}$$

$$A_1 = 0.0775h \tag{A.8}$$

Here we have switched to measurements in meters, rather than centimeters. Then we need to find the total amount of decay pairs, bounded by the range -25 cm $< z <$ 25 cm, which is required by the vertex cuts. We use that $m = 0.38h$ from similar triangles:

$$A_2 = 0.5\left(\frac{h+m}{2}\right) \tag{A.9}$$

$$= \frac{1}{4}(h+0.38h) \tag{A.10}$$

$$= 0.345h \tag{A.11}$$

When we take the ratio $\frac{A_1}{A_2}$ we get 0.225, meaning that this procedure isolates 22.5% of the decay muons in our data sample. The final result is then scaled up by this factor.

Appendix B

Pythia Settings

The comparisons to Pythia made in this analysis were mainly done with Pythia run in charm production mode. This allowed more efficient production of e$-\mu$ events than regular minimum bias hard scattering mode. However it does tend to overemphasize gluon fusion events. For this reason, distribution shape comparisons were made using POWHEG, which more accurately simulates NLO effects.

Pythia settings were chosen based on those used in previous PHENIX heavy flavor simulations, especially [81]. The settings were tuned to match with previous heavy flavor results. The K factor was determined to best scale the Pythia normalization to the single electron results to the gluon fusion-generated Pythia charm electrons.

Table B.1: Pythia Settings

Parameter	Setting	Description
MSEL	4	Type of hard process: charm production (gluon fusion and $q\bar{q} \rightarrow Q\bar{Q}$)
MSTP(51)	7	Use CTEQ5L PDF set
MSTP(91)	1	Use gaussian distributed intrinsic k_T
PARP(91)	1.5	Value of $< k_T >$
MSTP(33)	1	Use K factor
PARP(31)	3.5	Value of K factor
MSTP(32)	4	Use $Q^2 = s$ as hard scattering scale
PARP(93)	5.0	Maximum value of k_T in GeV/c
CKIN(3)	1.0	Minimum value of parton p_T
PMAS(4)	1.25	Charm quark mass in GeV/c^2
MSTP(82)	4	Multiple interactions consistent with gaussian matter distributions
PARP(84)	0.4	Core nuclear radius
PARP(85)	0.9	Probability for additional interactions to give two color connected gluons
PARP(86)	0.95	Probability for additional interactions to give PARP(85) condition or closed gluon loop
PARP(90	0.25	Power of energy rescaling term
PARP(67)	4	Maximum parton virtuality scale factor

Appendix C

Kinematic Variables

One of the kinematic quantities most commonly used to describe heavy ion collisions is the rapidity, y. It is given by,

$$y = \frac{1}{2}\ln\left(\frac{E + p_z}{E - p_z}\right) \tag{C.1}$$

where E is the energy and p_z is the longitudinal momentum of the particle [120]. The rapidity can be either positive or negative, depending on the direction of motion of the particle and the coordinate system. The benefit in describing a trajectory in terms of rapidity rather than longitudinal angle is that the values of rapidity measured in different reference frames are simply related by an additive quantity.

When a track is measured in a detector, the energy and/or momentum may

be unknown if the particle has not been identified. If we know nothing about the particle other than its angle relative to the beam, we may describe it using the pseudorapidity variable, η. It is defined as,

$$\eta = -\ln[\tan(\theta/2)] \tag{C.2}$$

where θ is the longitudinal angle relative to the beam. This may be written in terms of momentum as

$$\eta = \frac{1}{2}\ln\left(\frac{|p| + p_z}{|p| - p_z}\right) \tag{C.3}$$

where $|p|$ is the magnitude of the momentum. Because it may be measured experimentally, η is used more often in RHIC experiments than y. However, in the limit of large momentum $|p| \approx E$, rapidity and pseudorapidity converge to the same value.